The Complex Organic Molecular Inventory of the HD 100546 Protoplanetary Disk

Bibi Fatimah Noor-E-Madinah Dillmahomed

University of Leeds

School of Physics and Astronomy

Submitted in accordance with the requirements for the degree of

Masters by Research

November 2022

Intellectual Property Statement

The candidate confirms that the work submitted is her own and that appropriate credit has been given where reference has been made to the work of others.

This copy has been supplied on the understanding that it is copyright material and that no quotation from the thesis may be published without proper acknowledgement.

The right of Bibi Fatimah Noor-E-Madinah Dillmahomedto be identified as Author of this work has been asserted by her in accordance with the Copyright, Designs and Patents Act 1988.

Acknowledgements

Abstract

Protoplanetary disks are important astrophysical objects which contain all the material, gas and dust, from which planets form. Quantifying the complex organic molecular content of these planet-forming disks is crucial in determining the potential habitability of exoplanetary systems. The surprising detection of the simplest oxygen-bearing complex organic molecule (COM), methanol, in the nearby disk around HD 100546 provides an interesting laboratory to study the chemistry of COMs in warm Herbig disks. Using the detection of methanol as a starting point, we investigate the complex organic molecular reservoir of the HD 100546 disk by quantifying the abundances of other complex molecules, 15 in total and comprising of the simplest members of the organic functional groups detected in astrophysical sources, focusing on those observable with ALMA and SKA. We perform ray-tracing calculations to calculate their molecular line emission strength and simulate line spectra over the ALMA and SKA bandwidths. The chemical model predicts abundances comparable to the observed methanol of most COMs in the gas phase, especially at the location of the dust cavity at 13 au. The disk line survey run predicts strong lines of mainly the nitrogen-bearing COMs, methyl cyanide and isocyanic acid with both ALMA and SKA. Fitting observed radial profiles with those extracted after performing ray-tracing calculations with *LIME* shows that the reservoirs of formaldehyde and methanol are constrained within an inner component and outer component, possibly contributing to the verification of the double ring structure in the disk. If detected, the COMs investigated in this work will expand the complex organic molecular inventory of warm Herbig disks, revealing the presence of the precursors to biologically important molecules in the material from which planets form.

CONTENTS

LIST OF FIGURES

List of Tables

Abbreviations

COM	complex organic molecule	SKA	Square Kilometre Array
LAMDA	Leiden Atomic and Molecular DAtabase	SNR	signal-to-noise ratio
ODE	Ordinary Differential Equation	SED	spectral energy distribution
ALMA	Atacama Large Millimetre/Submillimetre Array	UV	ultraviolet
LIME	LIne Modeling Engine	ISM	interstellar medium
LTE	local thermodynamic equilibrium		

CHAPTER 1

Introduction

1.1 Protoplanetary Disks

During the formation of low-mass stars through gravitational collapse, the conservation of angular momentum inevitably gives rise to circumstellar disks which extend from tens to hundreds of astronomical units. After the initial tunneling of material onto the star and when the surrounding molecular core is used up or disperses, the accretion rate decreases and a small amount of material remains as this disk. The occurrence of the latter was revealed when the sky was first observed through the infrared (IR) lens by the Infrared Astronomical Satellite (IRAS) [Strom et al., 1989]. Made of cool gas and dust, these disks can be considered protoplanetary. The first sensitive detectors at millimetre (mm) wavelengths showed the large dust-grain content of disks [Weintraub et al., 1989] which is sufficient material to form planetary systems with size scales similar to ours. Protoplanetary disks have a flattened morphology - the unequivocal evidence for which was provided by the Hubble Space Telescope (HST) through optical images of disk shadows against a bright nebular background [O'dell and Wen, 1994]. Interferometry at sub-millimetre (sub-mm) wavelengths provides the ability to not only resolve the keplerian rotation of protoplanetary disks but also map fainter structures in greater detail. Such potential to elucidate protoplanetary disk-related questions motivated the development of facilities such as the Atacama Large Millimetre/submillimetre Array (ALMA). The composition of the material in a protoplanetary disk determines the habitability of exoplanetary systems formed from it. It remains a challenge to assess the latter. Measuring the inventory of organic material present at the time of planet formation is one way of evaluating the potential of forming extra-terrestrial planetary systems to produce and support habitable environments.

1.1.1 Formation of Protoplanetary Disks

After the collapse of the molecular cloud core, marking the beginning of star and planet formation, all the mass which was initially concentrated in the core is processed by an inward accretion onto the protostar and an outward outflow. The progression of this early-stage of evolution can be mapped by measuring the distribution of warm circumstellar material in IR, giving rise to either a Spectral Energy Distribution (SED) classification or an accretion-based classification of Young Stellar Objects (YSOs).

Class	SED slope	Physical properties	Observational characteristics
0	-	$M_{env} > M_{star} > M_{disk}$	No optical or near-IR emission
1	$\alpha_{IR} > 0.3$	$M_{star} > M_{env} \sim M_{disk}$	Generally optically obscured
FS	$-0.3 < \alpha_{IR} < 0.3$		Intermediate between Classes 1 and 2
2	$-1.6 < \alpha_{IR} < -0.3$	$M_{disk}/M_{star} \sim 1\%, M_{env} \sim 0$	Accreting disk; strong Hα and UV
3	$\alpha_{IR} < -1.6$	$M_{disk}/M_{star} \ll 1\%, M_{env} \sim 0$	Passive disk; no or very weak accretion

Table 1.1: SED classification of YSOs [Williams and Cieza, 2011], based on the SED slope, α_{IR}, where $\alpha_{IR} = \frac{d \log \nu F_\nu}{d \log \nu}$, into Classes 0, 1, FS (flat-spectrum sources), 2 and 3

The disk forms very early on and then grows rapidly during the Class 0 collapse phase within $\sim 10^4$ years as more distant material with higher angular momentum falls inwards. The disk extends out to the centrifugal radius, which increases significantly with the angular rotation rate of the core and the infall time in the case of magnetised core collapse ($R(t) \propto \Omega^2 t^3$, where t is the time and Ω is the angular rotation rate of the core).

Due to gravitational infall, disks have high temperatures in early stages. When the core material is used up or disperses, disks cool down and their mass decreases as they accrete onto the star. The relatively high mass fraction in the disk versus that accreted onto the protostar results in the gravitational instability. Disk instability is responsible for the rapid transport of the flow of material from the envelope through the disk, as shown by many observations of inward motions on core-size scales. This leads to a decrease in the mass of the envelope by about an order of magnitude between the Class 0 and Class 1 phases. These instabilities also lead to sporadic bursts of high accretion (called FU Orionis) which then cause the disk mass to grow slower than that of the star. This punctuated evolution at early stages is also revealed by measurements of mass infall rates through different components (the envelope infall rate being greater than the disk accretion rate by more than one order of magnitude in Class 1 YSOs causes the build-up of mass in the disk until a burst event occurs, as suggested by Eisner et al. [2005]) and protostar luminosity distribution. During $\sim 7\%$ of the ~ 0.5 Myr combined Classes 0 and 1 embedded phases, a star actually gains half of its final mass.

By the end of the Class 1 phase when the envelope has completely dispersed and the star formation process is effectively over, the disk can now be considered protoplanetery,

rather than protostellar as it now contains only a small fraction of the stellar mass. The deeply embedded Classes 0 and 1 phases of star formation last for only a small fraction of the disk lifetime of several million years, during which time, material either accretes onto the star by internal friction or viscosity; is lost through outflows in order to preserve angular momentum - thereby causing the disk to spread over time - and photoevaporation by the central star and external stars; or condenses into cm-sized or larger bodies or planetesimals which can gravitationally perturb the disks. Inner holes and gaps, revealed by a relative decrease in flux over a narrow range of wavelengths or by direct imaging at sufficiently high resolution, are the possible results of their different evolutionary pathways.

1.1.2 Observation of Protoplanetary Disks

Protoplanetary disks radiate over a range of wavelengths from microns to mm, making them observable with IR and radio telescopes. An accelerated pace of discoveries has been witnessed over the years, owing to increases in sensitivity, resolution and wavelength coverage. Such insights are the stepping stones in the understanding of exoplanet formation and the origins of our Solar System, thus motivating the development of further facilities in the IR to mm and sub-mm ranges, such the Atacama Large Millimetre/Submillimetre Array (ALMA).

The determination of the properties of protoplanetary disks around Class 2 YSOs provides the basis for studying their evolution. Observations at mid-IR through mm wavelengths allow the deduction of the properties of the outer parts (> 1 au) of protoplanetary disks as shown in Figure 1.1.2. Disk radii and dust grain properties can be inferred from optical and near-IR scattered light.

(Sub)Millimetre wavelength observations of dust are most appropriate to determine disk masses. In the outer regions of the disk (scales $\gg 10$ au), the emission is optically thin at mm wavelengths and the observed flux is related to the mass by $M_{(gas+dust)} = \frac{F_\nu d^2}{\kappa_\nu B_\nu(T)}$, where d is the distance to the source, κ_ν is the dust opacity (a common expression for κ_ν at millimetre wavelengths is $\kappa_\nu = 0.1(\frac{\nu}{10^{12}Hz})^\beta \text{cm}^2\text{g}^{-1}$, in which the power-law index β is related to the size distribution and composition of the dust grains and the normalisation includes a ratio of gas mass to dust mass of 100) and $B_\nu \approx 2\nu^2 kT/c^2$ is the Plank function close to the Rayleigh-Jeans regime (as it is in mm wavelengths). CO is commonly used as a tracer of the total gas mass

in both the interstellar medium and in protoplanetary disks. Much debate has arisen about the utility of CO as a mass tracer in disks, following a range of CO abundances (with measurements of low CO to dust mass ratios in numerous systems) revealed from observations of CO in protoplanetary disks [Schwarz et al., 2018]. This simple mass derivation is reasonably accurate with a characteristic temperature of 20 K. The inner-most regions which constitutes a significant fraction of the planet-forming region of the disk, are optically thick at mm wavelengths, and require not only high resolution, but also wavelengths longer than 1 mm to be probed. The outer cool parts of disks emitting weakly make it challenging to measure disk sizes. Their efficient absorbing capabilities are therefore used in the simple and direct determination of their radii. Interferometry is required when imaging disks at mm wavelengths due to their small angular scales in nearby star-forming regions.
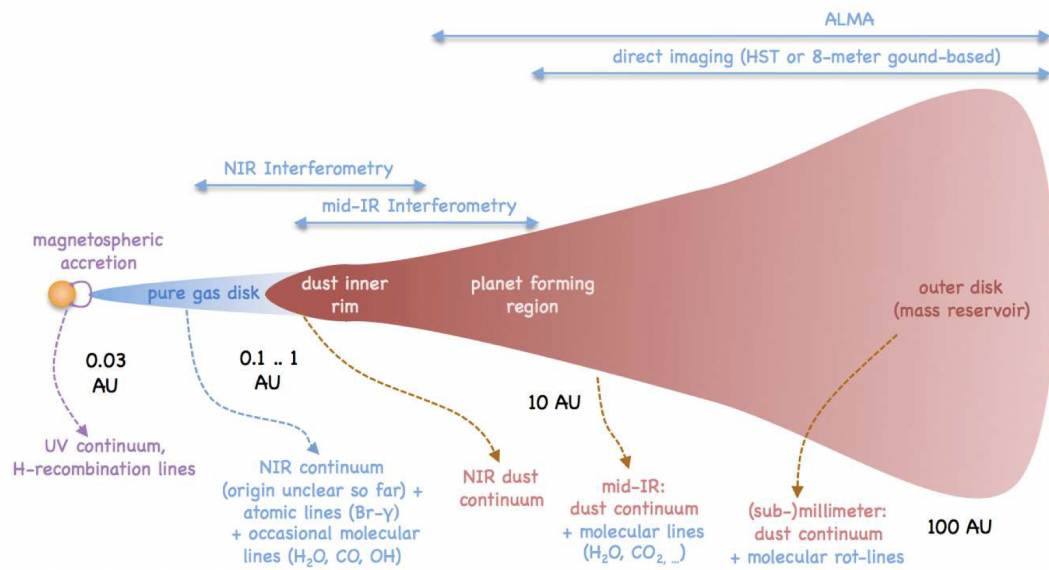
Figure 1.1: Techniques spatially resolving different scales of a protoplanetary disk and various kinds of emission arising from the different parts [Dullemond and Monnier, 2010]

1.1.3 Chemistry in Protoplanetary Disks

Protoplanetary disks host a rich and diverse chemistry which is implied by the strong vertical and radial temperature and density gradients, and largely differing radiation fields throughout the disk. Photochemistry, molecular-ion reactions, neutral-neutral reactions, gas-grain surface interactions and grain surface reactions are among the relevant active chemical reactions in disks.

The radial temperature gradient accounts for the distinction of inner disk chemistry from that in the outer regions (beyond 20 au). The high temperatures (100 K to 5000 K) and densities (up to 10^{12} cm^{-3}) in inner disks result in quasiequilibrium in the chemistry, with neutral-neutral reactions with barriers ($> 100 - 1000$ K) playing an important role in the absence of intense sources of ionising radiation. Therefore, inner disk chemistry mirrors conditions known for 'terrestrial' chemistry, driven by three-body collisions (the characteristic time scales of disk chemical processes are usually longer), which become significant in the very high density regime ($> 10^{12}$ cm^{-3}), such as the formation of molecular hydrogen by collisions of two hydrogen atoms and another particle that takes away the excess of energy of formation [Henning and Semenov, 2013]. Additionally, the inner high temperatures and densities imply a significantly higher abundance of gas-phase molecules until thermal dissociation at T$> 2500 - 3000$ K. The products of inner disk chemistry are observationally best characterised by infrared spectroscopy. High abundances of gas-phase H$_2$O and CO, and the presence of N-bearing molecules (e.g. NH$_3$, HCN, HNC) and hydrocarbons (e.g. CH$_4$ and C$_2$H$_2$) at 1 au are predicted by chemical models of inner disk chemistry.

On the other hand, the chemistry in the outer disk is mainly driven by high-energy radiation and cosmic rays. Rapid and mostly barrierless - hence effective at temperatures well below 100 K - ion-molecule processes are triggered and sustained by the proton transfer processes from ions - formed by the ionising radiation - to other neutrals. At low temperatures in the outer disks, freeze-out of molecules is another important feature, hence making them depleted for gas-phase chemistry. The ices on the surface of dust particles remain chemically active and they sublime at the higher temperatures in the inner disk, defining positions of snow lines which are a function of the luminosity of the central star and evolve with the evolutionary stage of the disks.

The outer disk (r> 20 au) chemistry can be classified in three vertical regimes (see Figure 1.3): the strongly irradiated hot disk surface layers, the partly shielded

warm molecular layer and the completely shielded cold disk midplane. In the topmost layer, a photon-dominated region prevails owing to stellar UV and interstellar radiation which ionises and dissociates molecules, subsequently driving ion-molecule chemistry. Depending on the actual radiation field, photodissociation operates differently for different molecules such that certain photons (e.g. Lyman alpha) selectively dissociate certain molecules (e.g. HCN and H_2O), leaving others (e.g. CO and H_2) unaffected. Apart from UV radiation, the keV X-ray radiation, driven by magnetic fields, enables a significant disk chemistry. X-ray photons are able to penetrate deeper into the disk and through higher gas columns (0.1-1 gcm^{-2}) due to their energies of several keV and also because the X-ray emitting source is often thought to be located high above the stellar photosphere at distances of several radii, causing the X-ray photons to reach the disk atmosphere at an oblique angle. X-ray-driven processes result in a rapid and rich gas-phase hydrocarbon chemistry which enriches the overall molecular complexity as X-ray photons can uniquely ionise He atoms, giving chemically active He^+, which is able to dissociate the tightly bound CO and other species, replenishing elemental gas-phase carbon and oxygen.
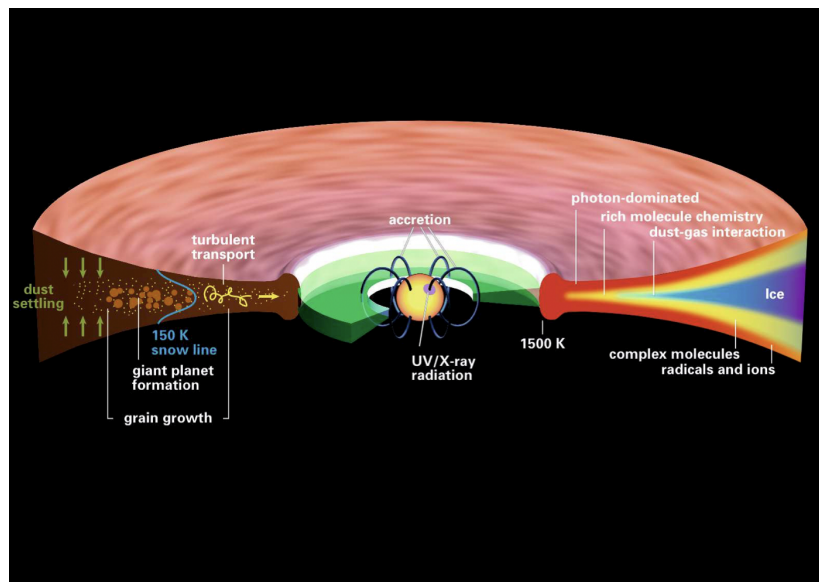
Figure 1.2: Physical and chemical structure of a $\sim 1-5$Myr-old protoplanetary disk around a Sun-like star [Henning and Semenov, 2013]

The middle warm (T= $30-70$ K) molecular layer houses a rich molecular, signi-

ficantly carbon-based, chemistry due to the high C/O ratio, accounted for by the CO being protected from freeze-out and the frozen water on dust grains decreasing the abundance of gas-phase oxygen. This layer also witnesses UV-driven photodesorption of molecules such as CO, H_2O, CH_4 and NH_3 in less opaque regions. The deepest layer is cold with temperatures < 20 K, causing the freeze-out of molecules and hence the chemistry to be dominated by hydrogenation reactions on grain surfaces. In the cold midplane of protoplanetary disks (densities of $10^6 - 10^8$ cm^{-3}), most of the material in the gas-phase is frozen out within a fraction of the disk lifetime (typical timescales are 10-1000 years). Volatiles such as CO, N_2 and CH_4 are primarily thermally desorbed, with the possibility of cosmic ray and X-ray spot heating releasing mantle material back to the gas phase.

Simulations, or models, of the chemistry are used to calculate the molecular abundances based on the rates of their formation and destruction by assorted chemical reactions. Their outputs are also good probes of the physical conditions as the rates of chemical reactions depend on them. Since these outputs are time-dependent, they also reveal the histories of the sources by comparison with observations. Models are undeniably an imperfect tool as our knowledge of the chemical processes is arguably incomplete and the time-varying physical conditions of the sources can put into question the predictions of the models which are based on current-day abundances. With a proper treatment of radiative transfer, predictions of the intensity and shape of spectral transitions and molecular abundances can be predicted.

1.2 Complex Organic Molecules

At present, 256 molecules [Guélin and Cernicharo, 2022], ranging from two-atom to seventy-atom species, have been detected in the interstellar medium, mainly via rotational emission spectra, obtained by the use of space-based and ground-based telescopes. The advent of radio astronomy in the early 1960s enabled a boom in the detection of new molecules, a trend which has continued at an average rate of 3.9 new detections per year ever since, with the development of newer facilities such as ALMA. Molecular hydrogen H_2 is the dominant molecule in all dense sources. It can be seen with difficulty: in infrared vibrational absorption in cool, dense sources; in UV absorption through diffuse matter; and via rotational and vibrational emission in warm or shocked matter. The second most abundant gas-phase molecule is carbon monoxide CO with

a typical fractional abundance of 10^{-4} relative to H_2. There is very little atomic hydrogen H in dense sources with $n_H \approx 2n_{H_2}$. Fractional abundances of molecules are expressed both relative to n_H, number density of hydrogen nuclei, and $2n_{H_2}$, number density of hydrogen molecules. Molecules can be categorised as terrestrial (commonly found on Earth) or exotic to space. The latter consists of molecular ions (e.g. HCO^+, C_4H^-), radicals (species with unpaired electrons; e.g. C_6H), isomers (species with the same atomic constituents but different structures, e.g. HCN and HNC), isotopologues (molecules containing unusual isotopes, e.g. H-2, C-13, N-15).

Most interstellar and circumstellar molecules are organic in nature - they contain carbon. These are the focus of many questions in astrochemistry, such as what is the exact form in which they exist under space conditions and how those of prebiotic importance survive the process of star and planet formation. Astronomical molecules are found in diverse environments, from nearby objects in our solar system to distant sources in the early universe. They are particularly associated with dense and cool neutral interstellar and circumstellar matter - comprising both a gaseous phase and a solid phase of tiny dust particles - in galaxies. Dense interstellar matter can be found in small individual objects, called globules or as part of giant molecular clouds (size ~ 100 pc and mass $\sim 10^5$ $M_\odot$) which are much larger irregular assemblies.

Bearing at least six atoms, complex organic molecules (COMs) bridge the gap between the simple two-or-three-atom molecules usually found in diffuse space and the more complex ones which are of prebiotic importance (e.g. amino acids and proteins), to which they are precursors. As opposed to simple molecules which are more often detected in disks, COMs may be present but are expected to be mostly locked up in ices. CO ice chemistry is indispensable for COMs to form and eventually be thermally released into the gas phase. COMs formed at the early stages of star formation are presumably important ingredients for the prebiotic chemistry of planetary systems and comparisons between the relative abundances of groups of molecules will arguably provide insights into the origin of chemical complexity and the link to planetary systems. COMs are detected in a wide range of environments, from cold gas in prestellar cores to warm gas close to protostars [Jørgensen et al., 2020]. Recent ALMA observations have revealed the presence of simple members of some key functional groups in organic chemistry - nitrile (acetonitrile, CH_3CN) [Öberg et al., 2015], alcohol (methanol, CH_3OH) [Walsh et al., 2016] and carboxylic acid (formic acid, HCOOH)

9

[Favre et al., 2018] - in cold disks. While these detections imply the presence of COMs at the epoch of planet formation, they do not elucidate their origin (in situ formation or inheritance).

Since the detection of methylidyne (CH), the first molecule identified in the interstellar medium (ISM) [Swings and Rosenfeld, 1937], observations of molecules have played crucial roles in broadening our understanding of interstellar chemical evolution [Herbst and van Dishoeck, 2009] and the formation of planets [Öberg et al., 2011]. Based on their spectra and chemistry, COMs are also excellent probes of the physical conditions, history and lifetime of the sources where they reside. As they are detected in young stellar objects, they are expected to be common ingredients for new planetary systems. Non-terrestrial molecules are interesting as they inform about the build-up of molecular complexity in the universe.

The richness of the molecular spectra reveals detailed information on the gas and dust, and characterises the species, for example: the density and temperature of the gas, and details about large-scale motion and collapse and rotation can be found from high-resolution rotational and vibrational spectra; information on the polar or nonpolar nature of the surroundings of dust particles can be obtained from the vibrational spectra of molecules found in them; chemical model outputs provide details on the physical conditions and history of the sources. The study of insterstellar molecules has helped to clarify the evolutionary stages of star formation in the Milky Way, especially for low-mass stars of luminosities $\lesssim 100$ $L_\odot$) [van Dishoeck and Blake, 1998]. In the absence of chemical fractionation (a process by which chemical reactions produce abundance ratios among isotopologues different from the actual elemental abundance ratios), isotopologues can be used to determine elemental abundance ratios at different places in the universe.

Of particular interest are oxygen-bearing COMs which have been relatively less often detected than hydrocarbons and nitrogen-bearing COMs. Since the latter can form in situ via gas-phase chemistry, their detection does not give clear indication on the degree of molecular inheritance in disks from the earlier, colder dark cloud stage which is known to be rich in oxygen-bearing COMs. Detection of the latter will clearly show the complex organic inventory available for planet formation. The simplest oxygen-bearing COM, methanol, CH_3OH has been so far detected three times, in disks around: the cold T-Tauri star TW Hya (with a low fractional abundance compared to

what is typically detected around protostars) [Walsh et al., 2016], the warm Herbig Be star HD 100546 [Booth et al., 2021b], the Herbig star IRS 48 [van der Marel et al., 2021].

Contrarily to all the other sources observed so far, HD 100546 and IRS 48 disks appear to have rich reservoirs of volatile oxygen, which makes them the best candidates to detect further molecular complexity, thus leading to our choice of HD 100546 disk as the target disk. The detection of methanol facilitated by ice sublimation implies inheritance of COMS-rich ices from an earlier cold dark cloud phase in protoplanetary disks [Booth et al., 2021b]. Further probing with regards to more complex species will provide a holistic view of the warm and rich inherited complex organic reservoir and chemistry. Their abundances relative to methanol in other environments will provide insights into the origin of COMs in disks. Simple members, 14 in total, of increasingly complex organic functional groups and 1 inorganic molecule, of equal interstellar importance, are chosen for this work.

1.3 The Protoplanetary Disk around the HD100546 Star

According to the luminosity and mass of their central stars, protoplanetary disks are classified as: brown dwarf disks (central star is not massive enough to trigger and power hydrogen burning), T-Tauri disks (central star is young, Sun-like of the F-M spectral types, has mass $\lesssim 2\mathrm{M}_\odot$, in which hydrogen burning starts at about 10^6 years), Herbig Ae/Be disks (central star have masses $\sim 2 - 8\mathrm{M}_\odot$ and are hot ($\sim 8000 - 15000\mathrm{K}$)). Herbig Ae/Be stars are more massive, hotter and more luminous than the T-Tauri counterparts of the spectral types A or B. They are optically visible intermediate pre-main sequence (PMS) stars which were first identified by Herbig in 1960 who described them as stars which have spectral type A and B with emission lines, lie in an obscured region and illuminate fairly bright nebulosity in their immediate vicinity.

HD 100546 is an isolated pre-main sequence star of spectral type B9 [Vioque et al., 2018]. It has a mass of 2.4 $\mathrm{M}_\odot$ [Vioque et al., 2018] and is located at a distance of 110.0 ± 0.6 pc [Gaia Collaboration et al., 2018]. It has an inner cavity at $r_{cav} \sim 11 - 13$ au, revealed by optical and near-IR observations (molecular ro-vibrational and scattered light emission) [Fedele et al., 2015], which is filled with atomic gas [Quanz et al., 2015a]. Multiple spiral arms at different spatial scales are indicated by high contrast imaging observations (Ardila et al. [2007] and Boccaletti et al. [2013]). Recent high-angular-

resolution ALMA observations resolved the disk at millimeter wavelengths and showed a compact ring at 20-40 au [Pineda et al., 2019], confirming the previously detected cavity and verifying part of the double ring structure suggested by Walsh et al. [2014a] from the early ALMA cycle 0 observations. The disk is host to HD 100546 b, of mass 15-20 M_{Jup}, which is the first directly imaged giant protoplanet candidate inside a disk [Quanz et al., 2015b]. The poorly constrained age of the star is estimated around 5-10Myr [Vioque et al., 2018]. Fedele et al. [2021] additionally reported, from new analysis of archival ALMA images, a wide dust gap between 40-150 au and a previously unresolved faint dust ring beyond 150 au. The emission in the outer disk is found to be unhomogeneous, with the detection of two main substructures at 180 au and 220 au. The presence of two giant protoplanets of masses 3.1 M_{Jup} and 8.5 M_{Jup} at 15 au and 110 au respectively are indicated by observations and comparison with hydrodynamical simulations [Fedele et al., 2021].
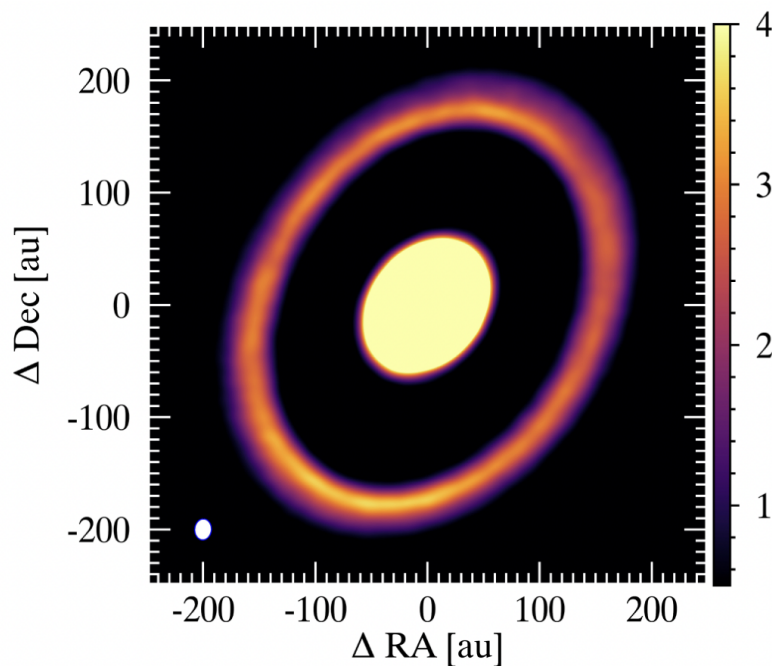
Figure 1.3: Synthetic ALMA 870 μm continuum image of the HD 100546 disk, with a zoom in on the inner disk [Fedele et al., 2021]

Being warm and hence lacking a significant CO-reservoir, the disks around Herbig stars cannot host the in situ formation of COMs. They are therefore thought to be

poor in COMs compared to their T Tauri counterparts. Booth et al. [2021b] confirmed the surprising detection of gas-phase methanol in HD 100546, which can be explained by inheritance from earlier cold dark cloud phase and radial transport followed by sublimation at its ice line. The detection of methanol facilitated by ice sublimation implies inheritance of ices in protoplanetary disks. Further probing with regards to more complex species will provide a holistic view of the warm and rich inherited complex organic reservoir and chemistry. Their abundances relative to methanol in other environments will provide insights into the origin of COMs in disks. It is of interest to further study the molecular inventory of the disk around HD 100546 as, being host to a substantial chemically complex reservoir inherited from an earlier cold phase, can either have its planets accrete icy, biologically important material during formation or have this material, which was previously present in the disk be delivered to the planets after formation.

1.4   This Thesis

In this project, we aim at investigating the complex organic molecular inventory of the protoplanetary disk around the Herbig Be star, HD 100546. This is crucial in determining the potential habitability of exoplanetary systems. The work done is documented in three chapters in this thesis:

1. In Chapter 2, Radiative Transfer of Molecular Emission of Formaldehyde and Methanol in the HD 100546 Protoplanetary Disk with the LIne Modelling Engine, we fit different components of formaldehyde and methanol along the disk to match the newly obtained radial profiles (obtained in a private communication from Booth, Booth et al. [2021a]) after performing ray-tracing calculations using the *LIME* code by Brinch and Hogerheijde [2010], while assuming LTE and neglecting dust.

2. In chapter 3, Chemical Modelling of Complex Organic Molecules in the HD 100546 Protoplanetary Disk, the output of a gas-grain chemical model previously run on a given physical structure of the disk is quantified, analysed and discussed, focusing on a choice of 15 molecules at four different timestamps.

3. In chapter 4, Line Survey of Complex Organic Molecules in the HD 100546 Protoplanetary Disk, molecular line emissions are calculated by performing ray-tracing

calculations in the ALMA and SKA regimes, using chemically modelled and parametrically modelled abundances, to predict the emergent spectra of the different species at 1Myr, using the code by Walsh et al. [2014b]. In these calculations, Local Thermodynamic Equilibrium (LTE) is considered and the disk is assumed to be face-on. Dust is not taken into account.

Overall, the findings will help to analyse new data from ALMA Cycle 8 and make predictions for requesting new data from ALMA and SKA in the future. If detected, these molecules will expand the complex organic molecular inventory of warm Herbig disks, revealing the presence of the precursors to biologically important molecules in the material from which planets form.

CHAPTER 2

Radiative Transfer of Molecular Emission of Formaldehyde and Methanol in the HD 100546 Protoplanetary Disk with the LIne Modelling Engine

2.1 Introduction

In this chapter, the LIne Modelling Engine, *LIME*, code by Brinch and Hogerheijde [2010] which solves the molecular excitation and radiation transfer problem in an arbitrary three dimensional geometry is used, after which radial profiles using the GoFish code by Teague [2019] are generated for two detected transitions of formaldehyde and methanol. The ray-tracing calculations are carried out in Local Thermodyamic Equilibrium (LTE) and without considering dust. The molecular reservoir is moved about in different models run in order to match the observed radial profiles obtained in a private communication from Booth et al. [2021a], thereby giving insights into the location of these molecules. An overview of the radiative transfer *LIME* code with insights into fishing for lines by GoFish is provided in the first section of this chapter. It is followed by the comparative plots of the radial profiles from the different models run in the Results section which are discussed in the subsequent section. A brief conclusion is then provided at the end of this chapter.

2.2 Methodology

In this section, the *LIME* code is briefly explained, with insights into generating radial profiles with GoFish and the parametric modelling done.

2.2.1 Radiative Transfer with LIME

The LIne Modelling Engine (*LIME*) code is designed to solve molecular and atomic excitation, and the radiative transfer problem in a molecular gas to predict the emergent spectra with models from (sub-)millimetre interferometers. It derives from the *RATRAN* code by Hogerheijde and van der Tak [2000] and is well-suited for modelling data of complex species and in very high spatial resolution for facilities such as ALMA as it can deal with cross-excitation and blended lines well. Using different physical models as input, it works in an arbitrary 3D-geometry using unstructured Delaunay latices for photon transport. Instead of mapping the source model onto a regular grid of cells, over each of which, model properties are taken to be constant, a random set of points representing the local environment is used and distributed in three-dimensional space. The molecular density profile of the source model is used as a probability distribution for the grid points, such that the average distance from a point to its neighbours is

inversely proportional to the density and proportional to the local mean free path , l, which is given by $l = (\alpha_\nu \rho)^{-1}$. These properties are particularly interesting when dealing with radiative transfer. The average grid point separation thus obtained scales with the local opacity in order to generate the random grid point distribution and its corresponding Delaunay triangulation on which the transport of photons occurs. The grid is ray-traced when convergence between level population, radiation field and point separation is attained and images are produced which can be readily compared with observations [Brinch and Hogerheijde, 2010].

Although the gas can be excited through both the absorption of a photon or through collisions with other molecules and *LIME* can consider collisional rates in calculations, LTE is assumed. The spectral intensity, I_ν of radiation propagating through a medium to be given in terms of the emission (j_ν) and absorption (α_ν) coefficients of the latter, given by:

$$\frac{dI_\nu}{ds} = j_\nu - \alpha_\nu I_\nu \tag{2.1}$$

and

$$J_\nu = \frac{1}{4\pi} \int I_\nu d\Omega \tag{2.2}$$

It is to note that the molecular excitation is therefore dependent on J_ν (as J_ν is in fact J_{il} for a transition between levels i and j). Equations for the mean radiation field and fractional population of an energy level form a recursive problem which must be solved iteratively.

In this work, the *LIME* code is run for the $4_{2,2} - 3_{2,1}$ transition of p-H_2CO and the $6_{2,5,1} - 5_{2,4,1}$ transition of $CH_3OH(E)$, using LAMDA molecular data, and models of H_2CO and CH_3OH abundances from Chapter 1 (derived from the chemical code described therein) and parametrically generated as explained further in the subsection 'Parametric Model Fitting', the latter being motivated and informed by the observed radial profiles recently obtained in a private communication.

2.2.2   Radial Profiles with GoFish

When studying protoplanetary disks, molecular line emission complement high resolution continuum data which exploit the bandwidths of telescopes. As opposed to continuum emission, line emission observations require a much higher sensitivity to

ensure robust detection. In order to achieve this, multiple observations are averaged (stacked) in order to cancel out the noise. Using the known rotation of a protoplanetary disk, GoFish shifts all emission to a common line center in order to stack them. Thus, the signal-to-noise of the spectrum increases, making the detection of weaker lines possible, or super-sampling the spectrum to better resolve the line profile. The rotation of a protoplanetary disk Doppler shifts the lines at a given location to a slightly offset frequency. For a disk with inclination i and rotation profile v_{rot}, the projected line of sight velocity, which is also the offset in the Doppler shifted line centre, at given coordinates (r, θ) in the disk, where r and θ are the disk-centric radius and polar angle respectively, is given by:

$$\delta v(r, \theta) = v_{rot}(r) cos(\theta) sin(i) \tag{2.3}$$

GoFish uses the image cube in the FITS format (with two spatial axes and one spectral axis), the inclination and position angle of the disk, and the distance and mass of the central star to extract the averaged or integrated spectra over a given radial range, providing the radial profile of the line.

2.2.3 Parametric Model Fitting

The observed radial profiles obtained from a private communication from Booth [Booth et al., 2021a] (Figure 2.1) are used as motivation for informing the models run in an attempt to reproduce them. Molecular reservoirs are moved across the disk by placing limits on their locations as a function of the temperature and/or radius. A linear ratio is employed when scaling the abundance used in the model in order to match the desired intensity. Nearly 30 models were run to reproduce the observed radial profile of the $4_{2,2} - 3_{2,1}$ transition of p-H_2CO and nearly 15 models, for the $6_{2,5,1} - 5_{2,4,1}$ transition of $CH_3OH(E)$. The progress of the parametric models for each transition is shown in Figure 2.1.
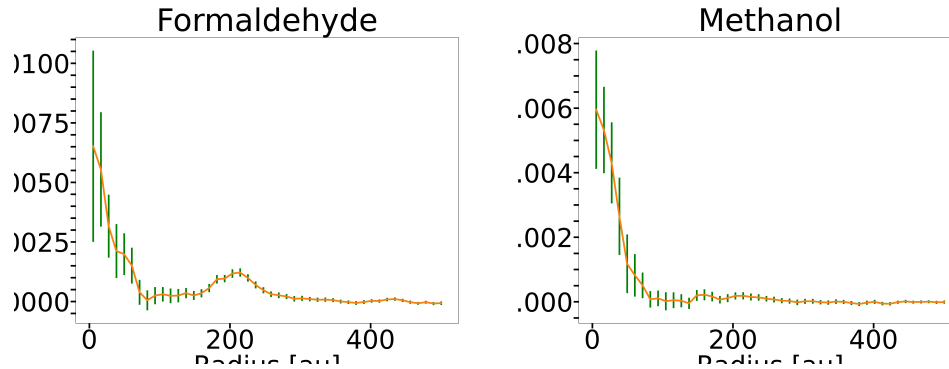
Figure 2.1: Observed radial profiles for the p-H$_2$CO $4_{2,2} - 3_{2,1}$ and E-CH$_3$OH $6_{2,5,1} -$ $5_{2,4,1}$ lines obtained in a private communication from Booth et al. [2021a] - plots of Intensity [Jy/beam km/s] against Radius [au] are shown

2.3 Results

In this section, the radial profiles calculated for the $4_{2,2} - 3_{2,1}$ formaldehyde line and the $6_{2,5,1} - 5_{2,4,1}$ methanol line to fit those observed are provided. The model on which *LIME* is run for the best fit with observations is also described for each line.

2.3.1 Radial Profiles of the $4_{2,2} - 3_{2,1}$ Line of p-Formaldehyde

Figure 2.2 shows the progress of the parametric modelling fitting for the $4_{2,2} - 3_{2,1}$ line for p-H$_2$CO, starting with the radial profiles when *LIME* is run with the chemical model in the top left panel, followed by the two of those when *LIME* is run with the parametric models int he top right and bottom left panels, and the radial profiles from the final parametric model run in the bottom right panel. *LIME* was first run by the abundances from the chemical model which is shown by the top left panel in Figure 2.2, which shows that although the chemical model predicts the right location of formaldehyde, it returns a higher abundance of the molecule, which results in the intensity to peak at 35 mJy beam^{-1} kms^{-1} at a radius of 19.2 au, as compared to an almost five times smaller value of 6.5 mJy beam^{-1} kms^{-1} at that same radius with the final parametric model. On the other hand, the observed radial profile for formaldehyde is seen to peak at 5.5 au at 6.5 mJy beam^{-1} kms^{-1}.
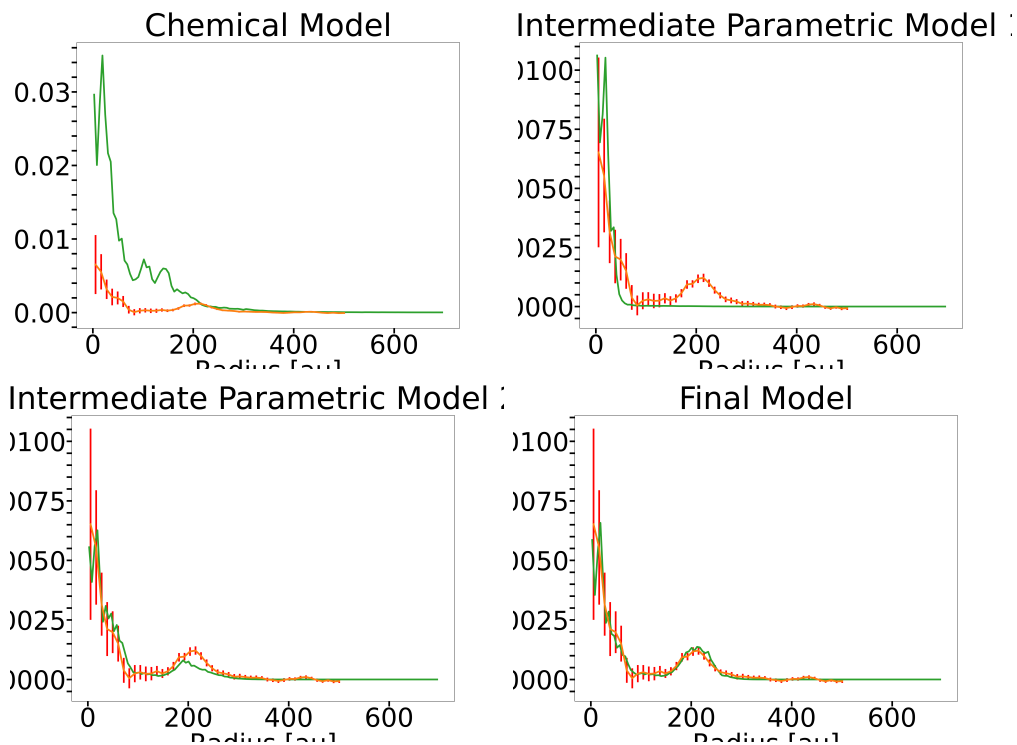
Figure 2.2: Fitting of radial profiles after running *LIME* with abundances from different models on the $4_{2,2} - 3_{2,1}$ line for p-H_2CO; top left: chemical model, top right: intermediate parametric model 1 (inner component fitting), bottom left: intermediate parametric model 2 (shoulder fitting), bottom right: final parametric model 3 (final fitting) - plots of Intensity [Jy/beam km/s] against Radius [au] are shown - *observed radial profiles: red, parametrically fitted radial profiles: green*

2.3.2 Radial Profiles of the $6_{2,5,1} - 5_{2,4,1}$ Line of Methanol(E)

Figure 2.3 shows the progress of the parametric modelling fitting for the $6_{2,5,1} - 5_{2,4,1}$ line for $CH_3OH(E)$, starting with the radial profiles when *LIME* is run with the chemical model in the top left panel, followed by the two of those when *LIME* is run with the parametric models in the top right and bottom left panels, and the radial profiles from the final parametric model run in the bottom right panel. *LIME* was first run by the abundances from the chemical model which is shown by the top left panel in Figure 2.3, which shows that unlike formaldehyde, it returns a comparable abundance of the molecule, which results in the intensity to peak at 11 mJy beam^{-1} kms^{-1} at a radius of

2.75 au, as compared to a smaller value of 6.1 mJy beam^{-1} kms^{-1} at a greater radius of 19.2 au with the final parametric model. On the other hand, the observed radial profile for methanol is seen to peak at 5.5 au at 6.0 mJy beam^{-1} kms^{-1}. It is noted that peak intensities are noted at the same radii for both methanol and formaldehyde in the final parametric model (19.2 au, which is the radius at which the intensity of formaldehdye also peaks in the chemical model) and the observed radial profiles (5.5 au).
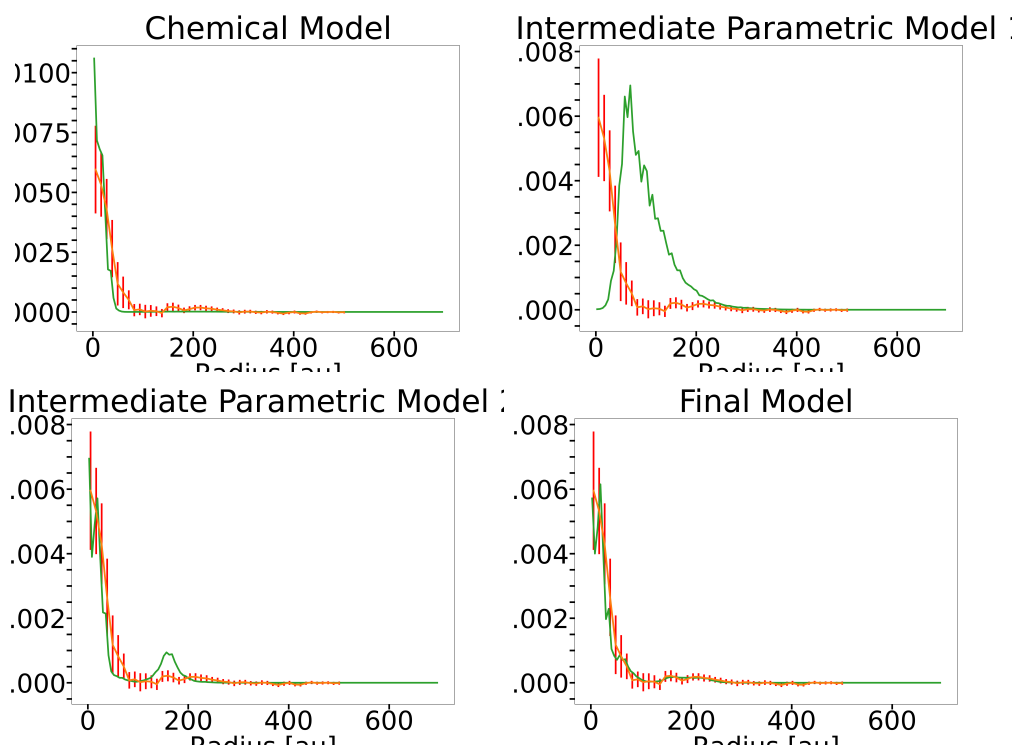
Figure 2.3: Fitting of radial profiles after running *LIME* with abundances from different models on the $6_{2,5,1} - 5_{2,4,1}$ line for CH$_3$OH(E); top left: chemical model, top right: parametric model 1, bottom left: parametric model 2, bottom right: parametric model 3 (final fitting) - plots of Intensity [Jy/beam km/s] against Radius [au] are shown - *observed radial profiles: red, parametrically fitted radial profiles: green*

2.4   Discussion

For formaldehyde, the fitting was done by constraining the molecular reservoir as a function of temperature and/or radius in order to reproduce the observed inner, shoulder and outer ring components. Table 2.1 shows the abundances, and the radius and temperature limits within which the molecular reservoir is placed, for each of the parametric models shown in Figure 2.2.

| Parametric Model | Radius/au | | Temperature/K | | |
	r_{min}/au	r_{max}/au	T_{min}/K	T_{max}/K	Abundance
Intermediate model 1	-	-	90	170	5.0×10^{-11}
Intermediate model 2	0	10	140	220	2.8×10^{-11}
	10	30	90	150	2.8×10^{-11}
	40	80	40	90	4.2×10^{-12}
	90	150	20	50	2.8×10^{-12}
	175	275	5	65	5.6×10^{-11}
Final Model	0	10	140	220	2.8×10^{-11}
	10	30	90	150	2.8×10^{-11}
	40	80	40	90	2.5×10^{-12}
	90	150	20	50	2.8×10^{-12}
	175	200	5	65	7.0×10^{-11}
	200	225	5	65	2.0×10^{-10}
	225	275	5	65	7.5×10^{-12}

Table 2.1: Parametric modelling fitting $4_{2,2} - 3_{2,1}$ p-H_2CO line, showing the locations in terms of the radius and/or temperature boundaries for the parametric models reported in Figure 2.2

As we move radially outwards from the star, a decreasing temperature gradient is expected, such that in order to fit the inner ring component of 0-30 au, formaldehyde was constrained within a temperature range of 140-220 K, followed by 90-150 K. As for the shoulder component within 40-150 au, the temperature was between 20 K and 90 K, and for the outer ring of 175-275 au, the temperature range was 5-65 K. A steeper temperature gradient is therefore seen closer to the star. The abundance within the

inner ring, at 2.8×10^{-11} was found to be less than the maximum abundance in the chemical model and the abundance predicted by the parametric model in Chapter 4 (to be seen later) by four orders and one order of magnitude respectively. It is then seen to decrease by one order of magnitude at radii of 40-150 K, and a subsequent significant increase by two orders of magnitude is seen at 200-225 au, within the outer ring. An abundance which is one order of magnitude greater than that in the inner ring is justified, despite the lower intensity at these radii, because of the low temperatures, which result in a smaller fraction of the reservoir having their 80 K-upper energy levels populated for the transition to take place and contribute in the emission of the photons.

For methanol, the fitting was done by constraining the molecular reservoir as a function of temperature and/or radius in order to reproduce the observed components. Table 2.2 shows the abundances, and the radius and temperature limits within which the molecular reservoir is placed, for each of the parametric models shown in Figure 2.3.

	Radius/au		*Temperature/K*		
Parametric Model	$\mathbf{r}_{min}$**/au**	$\mathbf{r}_{max}$**/au**	$\mathbf{T}_{min}$**/K**	$\mathbf{T}_{max}$**/K**	**Abundance**
Intermediate model 1	-	-	20	50	3.8×10^{-10}
Intermediate model 2	0	50	90	170	2.8×10^{-10}
	50	100	40	90	3.8×10^{-12}
	140	180	5	65	3.8×10^{-10}
	180	250	5	65	3.8×10^{-11}
Final Model	0	25	90	170	2.8×10^{-10}
	25	50	90	170	6.6×10^{-10}
	50	100	40	90	1.9×10^{-11}
	140	190	5	65	6.6×10^{-11}
	200	250	5	65	1.9×10^{-10}

Table 2.2: Parametric modelling fitting of the radial profile of the $6_{2,5,1} - 5_{2,4,1}$ $CH_3OH(E)$ line, showing the locations in terms of the radius and/or temperature boundaries for the parametric models reported in Figure 2.3

Like with formaldehyde, a decreasing temperature gradient is followed radially outwards from the star, such that in order to fit the inner component of 0-50 au, methanol

was constrained within a temperature range of 90-170 K. As for intermediate component between 50 au and 100 au, a temperature of 40-90 K was used, and for the colder outer component within 140-250 au, the temperature was between 5K and 65 K. The abundance within the inner ring, at 2.8×10^{-10} was found to be three orders of magnitude less than the maximum abundance in the chemical model and comparable to that predicted by the parametric model in Chapter 4 (to be seen later). It is then seen to decrease by one order of magnitude at radii of 40-150 K. A subsequent increase by one order of magnitude is seen at 200-250 au, making the abundance in the outer component of the same order of magnitude as that in the inner component. This is justified despite the lower intensity at these radii, because of the low temperatures, which result in a smaller fraction of the reservoir having their 70 K-upper energy levels populated for the transition to take place and contribute in the emission of the photons.

2.5 Conclusions

From the radiative transfer calculations, significant reservoirs of gas-phase methanol and formaldehyde, with abundances reaching 10^{-10} are predicted to be located in an inner range of radii and an outer shoulder, possibly in line with the double ring structure suggested by Walsh et al. [2014a]. The wide dust gap between 40-150 au and the faint dust ring beyond 150 au reported in [Fedele et al., 2021] can account for the components at these radii in the final models for both molecules. The peak fractional abundances obtained from the chemical model in Chapter 2 are found to be 5 to 7 orders of magnitude greater than those reported at the same radii from the parametric modelling done in this chapter, suggesting that the chemical model calculates overestimates of the fractional abundances. The abundances in this parametric are more comparable to those predicted in the parametric modelling in the coming Chapter 4.

CHAPTER 3

Chemical Modelling of Complex Organic
Molecules in the HD 100546 Protoplanetary Disk

3.1 Introduction

In order to understand the chemical evolution of the material in astrophysical objects, astrochemical models are developed and used. In this chapter, the abundances of 15 chosen COMs in the protoplanetary disk around the Herbig Be star HD 100546 are analysed and discussed. The output from a chemical model, using a chemical network including gas-phase and grain-surface reactions is used to compute the column densities and fractional abundances. An overview of astrochemical modelling, with insights into the chemical model and network used is provided in the first section of this chapter. It is followed by the plots of column densities and maps of fractional abundances in the Results section which are discussed in the subsequent section. A brief conclusion is then provided at the end of this chapter.

3.2 Methodology

In this section, insights into astrochemical modelling and the chemical network employed are provided, with elaboration on the calculations of column densities of the different COMs.

3.2.1 Astrochemical Modelling

The gas and dust in the ISM are constantly refreshed and modified during the life cycle of stars. Material, previously formed inside a star, spreads throughout the ISM after its death, in the form of atoms and 'grains' (refractory dust particles). Chemical processes and the strong interstellar UV field modifies this material, such that different chemistries take place in different regions and under different conditions, e.g. in the interior of dense clouds, a rich gas-phase chemistry, involving molecular ions, radicals, isomers and large linear unsaturated molecules, takes place, and during the star and planet formation phase within these clouds, the molecular complexity develops into a more terrestrial organic chemistry including saturated molecules such as basic esters, alcohols and nitriles. In order to compute the chemical composition and evolution of the mixture of gas and dust under astrophysical conditions, astrochemical models are developed and adapted to the different objects being studied (e.g. dark clouds, star-forming regions, protoplanetary disks), based on their characteristics, such as history, geometry, temperatures, densities, UV radiation fields and X-rays. Moreover, as seen

in section 1.2, a large number of molecules have now been observed in the ISM and this number is expected to increase over the coming years, owing to powerful interferometric facilities such as ALMA, although the most recent detections of new molecular species in the ISM have been accomplished with single-dish telescopes operating at centimeter wavelengths such as the GBT and the Yebes 40m telescopes [McGuire, 2022]. The physical properties of astrophysical objects are probed through the excitation of the observed spectral lines of simple molecules such as CO and CS [Dutrey et al., 2007]. It is equally important for observers to know the distribution of these and other species, in terms of abundances (defined as the ratio of the density of a species to the total density of hydrogen atoms).

Understanding the chemical composition and evolution of astrophysical objects is possible through chemical models. When combined with radiative transfer, predictions from the latter are useful in determining the detectability of some species. Astrochemical models are therefore a crucial tool in the understanding of various physical and chemical processes in space, the need of which is becoming increasingly relevant with the advent of ground-based and space-borne facilities making spectroscopic observations at high spatial and spectral resolution possible and accessible. As a result, a detailed grasp of chemical kinetics, especially reaction rate coefficients over a large range of temperatures, is required.

Numerically, chemical models solve a system of differential equations of the type:

$$\frac{dn_i}{dt} = \sum production - \sum destruction \tag{3.1}$$

where n_i is the density of species i in cm^{-3}. The production and destruction terms refer to all chemical and physical processes that produce and destroy this species respectively. Sophisticated and optimised ODE solvers are used to numerically propagate the ODEs (Ordinary Differential Equations) in time (e.g., ODEPACK), to finally compute the evolution of the abundances of species for a set of parameters and from an initial composition.

Astrochemical models have to take into account several parameters which can influence the chemical composition, such as elemental abundances and initial conditions, the geometry of the object and the dynamics (physical conditions varying with time). The material constantly modifying the ISM make-up consists of various elements which are eventually stored in three forms: in the gas-phase (in atomic or molecular form);

in refractory cores of interstellar grains (formed in circumstellar envelopes); in an icy mantle of volatile species on top of grain cores [Draine, 2003]. Some elements also get depleted, by mechanisms which still remain a puzzle [Draine, 2009], although it is commonly assumed that the missing elements in the gas-phase stick on grains. Direct measurements of the fraction of the elements partaking in the molecule building in dense clouds in the gas and grain mantles are not available. Therefore, chemical models of protoplanetary disks (and other dense sources such as molecular clouds and protostellar envelopes) include depletion of elements heavier than oxygen as initial input. Additionally, the assumed initial conditions (initial composition of species) will impact the prediction of the chemical composition by the model as the chemistry is not steady-state in most objects. Since there is not any model so far which can map the complete cycle of chemical evolution of the gas and dust from the material ejected from stars to the collapse of clouds to form new stars, mainly due to a lack of understanding of the evolution between different stages of planet formation (e.g. diffuse clouds, protostellar envelopes, protoplanetary disks), assumptions about previous steps are made [Wakelam et al., 2013]. In the specific case of protoplanetary disks, the assumed initial conditions are usually the chemical composition of the parent cloud [Hersant et al., 2009].

Since turbulence (or any kind of mixing) is non-negligible in astrophysical sources, the chemistry cannot be treated in a zero-dimensional approximation (a single spatial point), where the temperature and density are kept constant in space and time. The presence of temperature and density gradients result in a radially varying chemistry. In protoplanetary disks with radial and vertical mixing, 2D chemical models such as that in Semenov et al. [2006] have been developed. As such, the geometry is particularly important, especially in the treatment of the interaction with UV photons, where in the case of protoplanetary disks, UV penetration has to be computed in two dimensions to account for the stellar and interstellar UV radiation fields. Finally, since astrophysical objects are dynamic over a significant period of time (long enough for the chemistry to reach steady state), the changes in the physical conditions with time have to be also considered in the models. A realistic way of including the dynamics is to couple the chemistry to a 1D hydrodynamic collapse model to compute the evolution of the physical conditions, e.g. in a Lagrangian approach as in Aikawa et al. [2008].

In this work, the output from a code that reads in a physical model with fixed con-

ditions; computes the rate coefficients; passes them to an ordinary differential equation (ODE) solver; then outputs the fractional abundances as a function of a 2-D grid and time, is used.

3.2.2   The Chemical Network

Four main physico-chemical processes govern the chemistry in the ISM depending on the physical conditions, namely interaction with high-energy cosmic-ray particles, UV photon-induced photo-processes, bimolecular gas-phase reactions and interactions with grains Wakelam et al. [2013], as illustrated in Figure 3.2.2.
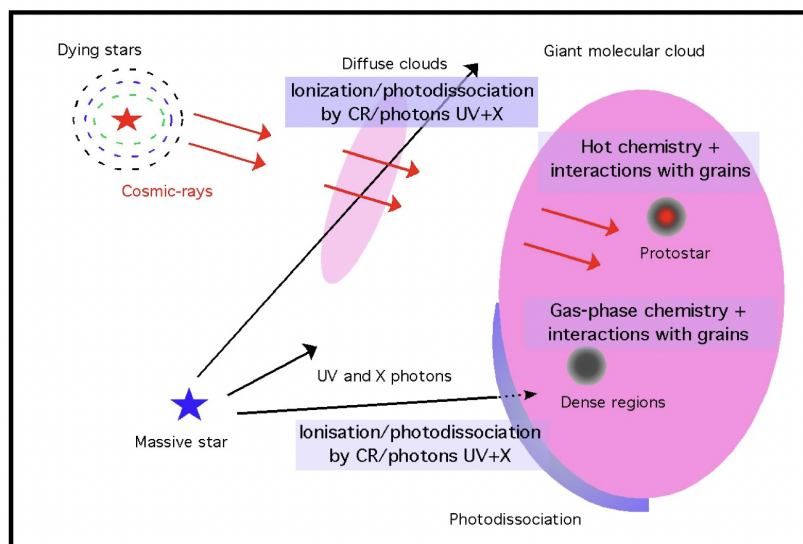
Figure 3.1: Dominant physico-chemical processes in the ISM [Wakelam et al., 2013]

The gas-grain chemical network used to calculate the disk chemical evolution and generate the chemical model of the HD 100546 disk analysed in this work originates from Walsh et al. [2010] and includes two-body gas-phase reactions, gas-grain interactions (freezeout and desorption), and grain-surface chemistry. The photoreaction rates and X-ray ionisation rates are computed using the methods outlined in Walsh et al. [2012]. The gas-phase chemistry is from the UMIST Database for Astrochemistry [McElroy et al., 2013]. Freezeout of gas-phase material onto dust grains; thermal and non-thermal desorption; photodesorption by both external and internal UV photons; desorption via cosmic-ray heating of dust grains are included. For the synthesis of COMs, the grain-

surface network from [Garrod et al., 2008] is included. The photodestruction of grain mantle material by UV photons, X-rays, and cosmic rays and UV- and X-ray-induced chemistry in the ice are also considered. The equivalent gas-phase photorates for ice species are adopted and products are allowed to remain on the grain to take part in further grain-surface reactions.

Gas-Phase Chemistry

The gas-phase chemistry is the complete network from the UMIST Database for Astrochemistry (UDfA) termed "RATE12" [McElroy et al., 2013] and is described by 6173 reactions, among 467 species which include 268 cations, 28 anions and 171 neutral species. The RATE12 reaction network is an upgrade of the RATE06 reaction network of Woodall et al. [2007] and includes gas-phase two-body reactions, photodissociation and photoionisation, direct cosmic-ray ionisation, and cosmic-ray-induced photodissociation and ionisation. A more comprehensive list of the reactions and the number of each reaction in the network is given in table 3.1

Reaction type	Count
Associative Detachment	132
Collisional Dissociation	14
Charge Exchange	579
Cosmic-Ray Proton	11
Cosmic-Ray Photon	249
Dissociative Recombination	531
Ion-Neutral	2589
Mutual Neutralisation	981
Neutral-Neutral	619
Photoprocess	336
Radiative Association	92
Radiative Electron Attachment	24
Radiative Recombination	16

Table 3.1: Reaction type and number of each reaction type in Rate12 (adapted from McElroy et al. [2013])

The rate coefficients are calculated as follows for the different reaction types, with special care taken to avoid any discontinuities between temperature ranges:

- Two-body reactions (Arrhenius-type formula)

$$k = \alpha \frac{T}{300}^{\beta} \exp\left(\frac{-\gamma}{T}\right) cm^3 s^{-1} \tag{3.2}$$

where T is the gas temperature in Kelvin.

- Direct cosmic-ray ionisation

$$k = \alpha s^{-1} \tag{3.3}$$

- Cosmic-ray-induced photoreactions

$$k = \alpha \frac{T}{300}^{\beta} \frac{\gamma}{1 - \omega} s^{-1} \tag{3.4}$$

where α is the cosmic-ray ionisation rate, γ is the efficiency of the cosmic-ray ionisation event, and ω is the dust-grain albedo in the far ultraviolet (typically 0.4-0.6 at 150nm).

- For interstellar photoreactions

$$k = \alpha \exp(-\gamma A_V) s^{-1} \tag{3.5}$$

where α represents the rate coefficient in the unshielded interstellar ultraviolet radiation field, A_V is the dust extinction at visible wavelengths and γ is the parameter used to take into account the increased dust extinction at ultraviolet wavelengths.

Gas-Grain Interactions

In large areas of protoplanetary disks where the dust temperature possibly reaches values below that of the freezeout of molecules, gas-grain interactions are important. The adsorption (freezeout) of molecules on dust grains forming ice mantles and the desorption (sublimation) of ices via thermal desorption and photodesorption play an important role in the chemistry. For the thermal desorption of a particular molecule to occur, the dust-grain temperature must exceed the freezeout temperature of that molecule. For the simplified calculation of the gas-grain interaction rates, grains are

assumed to be compact negatively-charged spherical grains with a radius of 0.1 μm and a fixed fractional abundance of $\sim 10^{-12}$ relative to the gas number density (equivalent to a gas-to-dust mass ratio of ~ 100), resulting in each grain having $\sim 10^6$ surface binding sites. Photodesorption by both external photons and photons generated internally via the interaction of cosmic rays with H_2 molecules are considered. In the calculation of the freezeout rates, a sticking coefficient, $S \sim 1$, is assumed for all species (except H).

Grain-Surface Chemistry

In the outer disk, where the freezeout of molecules is most prevalent, the abundances of COMs are enhanced to potentially observable values when grain-surface chemistry and photodesorption are included in chemical models [Walsh et al., 2015]. The chemically "active" zone is limited to the top two monolayers of the ice mantle and the size of the barrier to surface diffusion is assumed to be 0.3 times (as this allows the efficient formation of COMs via radical-radical association reactions at $\gtrsim 20$ K [Walsh et al., 2014b]) the binding energy. Thus, volatile species diffuse at a faster rate than strongly bound species. Grain-surface association reactions from the grain-surface network of Garrod et al. [2008] are included, where reactions between the radicals (an atom or molecule with at least one unpaired electron, which can easily react; or an unsaturated molecule, whose multiple bonds may be broken according to some activation energy, e.g. CO), H, OH, CO, HCO, CH_3O, CH_2OH, CH_3, NH and NH_2 are considered. With the exception of H and CO, the radicals are mainly derived from the photolysis of ices (e.g. H_2O, CH_4, H_2CO, CH_3OH) or from accretion from the gas phase. When these primary radicals react, secondary radicals or stable (typically saturated) molecules form. The latter can also be formed from further reactions between primary and secondary radicals. Figure 3.2.2 [Garrod et al., 2008] shows all reactions between the primary radicals. Reactions are assumed to occur only at the radical sites without any intramolecular rearrangement, leading to the preservation of the structure of the component radicals in the product and the possible formation of structural isomers through the combination of primary and secondary radicals.

E_b(K)	225	557	588	800	1189	1250	1425	1978	2254
Radical	H	CO	CH$_3$	HCO	NH	CH$_3$O	OH	NH$_2$	CH$_2$OH
H	H$_2$								
CO	HCO	x							
CH$_3$	CH$_4$	CH$_3$CO	C$_2$H$_6$						
HCO	H$_2$CO	x	CH$_3$CHO	OHCCHO					
NH	NH2	HNCO	CH$_3$NH	HNCHO	N$_2$H$_2$				
CH$_3$O	CH$_3$OH	CH$_3$OCO	CH$_3$OCH$_3$	HCOOCH$_3$	CH$_3$ONH	(CH$_3$O)$_2$			
OH	H$_2$O	COOH (CO$_2$ + H)	CH$_3$OH	HCOOH	HNOH	CH$_3$OOH	H$_2$O$_2$		
NH$_2$	NH$_3$	NH$_2$CO	CH$_3$NH$_2$	NH$_2$CHO	HNNH$_2$	CH$_3$ONH$_2$	NH$_2$OH	(NH$_2$)$_2$	
CH$_2$OH	CH$_3$OH	CH$_2$(OH)CO	C$_2$H$_5$OH	CH$_2$(OH)CHO	CH$_2$(OH)NH	CH$_3$OCH$_2$OH	CH$_2$(OH)$_2$	CH$_2$(OH)NH$_2$	(CH$_2$OH)$_2$
E_A (K)	2500	1500 (80)							

Figure 3.2: Reaction between primary radicals ($\times$: reaction not considered) [Garrod et al., 2008]

The grain-surface reaction rates are calculated assuming the Langmuir-Hinshelwood mechanism, and using the rate-equation method as described in Hasegawa et al. [1992], given by:

$$\frac{dN(A)}{dt} = k_{acc}n(A) - k_{des}N(A) - \sum(k_{hop,A} + k_{hop,i})\frac{N(A)N(i)}{N} + \sum(k_{hop,i_1} + k_{hop,i_2})\frac{N(i_1)N(i_2)}{N} \tag{3.6}$$

where $n(A)$ is the gas phase abundance of species A. The first term accounts for accretion of A from the gas phase to the surface, where k_{acc} is the accretion rate coefficient (obtained by the product of the velocity of A in the gas phase, the cross section of the grain, and the sticking fraction of A to the grain, which depends on the gas and surface temperatures). The second term represents the loss of A from the surface due to thermal or non-thermal desorption, which includes photodesorption; cosmic-ray desorption due to sputtering or flash heating of the grain; and desorption upon reaction. The rate coefficient for thermal desorption, $k_{des,therm}$ is given by:

$$k_{des,therm} = \nu \exp\{-E_{des}/k_B T_{grain}\} \tag{3.7}$$

where ν is the attempt frequency, E_{des} is the desorption energy, k_B is the Boltzmann constant, and T_{grain} is the grain temperature. The third term refers to the loss of species A due to Langmuir-Hinshelwood reactions with species i. The rate coefficient $k_{hop,i}$, defined as the rate of hopping of species i over the potential barrier between two adjacent sites, is given by:

$$k_{hop,i} = \nu_0 \exp\{-E_{b,i}/k_B T_{grain}\} \tag{3.8}$$

Similarly, the last term represents the gain in species A by formation mechanisms.

Initial Abundances

To generate a set of initial abundances for input into the disk model, a single-point dark cloud chemical model from atomic conditions for 1 Myr was run. The gas and dust temperatures were set at 10K, a density of H nuclei of 2.0×10^4 cm^{-3} was assumed and the cosmic ray ionisation rate was set to 10^{-17} s^{-1}. The initial abundances of different molecules in the gas and grain states are given in Table 3.2. The listed species are limited to those which have an abundance $\gtrsim 1\%$ that of water ice, the dominant O-bearing species. These initial abundances assume inheritance of the ice from an earlier cold phase.

Gas		*Ice*	
Species	**Initial Abundance**	**Species**	**Initial Abundance**
H_2	5.0×10^{-1}	H_2	6.9×10^{-4}
He	9.8×10^{-2}	H_2O	1.5×10^{-4}
O	6.1×10^{-5}	CO	3.6×10^{-5}
CO	3.6×10^{-5}	NH_2OH	1.7×10^{-5}
N	1.6×10^{-5}	H_2CO	1.1×10^{-5}
C	5.3×10^{-6}	N_2	8.8×10^{-6}
H	3.9×10^{-6}	C_2H_6	8.6×10^{-6}
N_2	1.9×10^{-6}	HCN	7.7×10^{-6}
		HNC	5.9×10^{-6}
		CH_4	4.2×10^{-6}
		NH_2CHO	2.4×10^{-6}
		NH_3	1.4×10^{-6}
		CO_2	6.7×10^{-7}
		CH_3OH	2.9×10^{-8}

Table 3.2: Initial abundances of different species in the gas and grain states

3.2.3 Analysis of the Chemical Model of the HD 100546 Protoplanetary Disk

Considering the chemical modelling of Walsh et al. [2014b] of COMs in the T-Tauri protoplanetary disk around TW Hya, the experimental production rates of complex organics in CH$_3$OH-rich ices by Öberg et al. [2009] and the laboratory experiments on the formation of COMs at low temperature by Chuang et al. [2016], the 15 molecules in Table 3.3 are thought of interest for this work. Chuang et al. [2016] particularly showed that methyl formate, glycolaldehyde and ethylene glycol can form through recombination of free radicals formed via H-atom addition and abstraction reactions at different stages in the CO-to-H$_2$CO-to-CH$_3$OH hydrogenation network at 15 K. They are mostly simplest members of different organic functional groups as we aim to explore further molecular complexity in the HD 100546 disk after the detection of gas-phase methanol therein [Booth et al., 2021b].

Molecule	Functional Group	Formula
Oxygen-bearing COMs		
Methanol	simplest alcohol	CH$_3$OH
Formaldehyde	simplest aldehyde	H$_2$CO
Acetaldehyde	second simplest aldehyde	CH$_3$CHO
Glycolaldehyde	simplest molecule containing both an aldehyde and a hydroxyl groups	CH$_2$OHCHO
Formic acid	simplest carboxylic acid	HCOOH
Methanoic acid	second simplest carboxylic acid	CH$_3$COOH
Dimethyl ether	simplest ether	CH$_3$OCH$_3$
Ketene	simplest ketene	CH$_2$CO
Methyl methanoate	simplest ester	HCOOCH$_3$
Nitrogen-bearing COMs		
Methyl amine	simplest amine	CH$_3$NH$_2$
Methyl cyanide	simplest nitrile	CH$_3$CN
Methyl cyanide radical	radical of simplest nitrile	CH$_2$CN
Oxygen-and-Nitrogen-bearing COMs		
Isocyanic acid	simplest isocyanate (the simplest molecule containing C, N and O)	HNCO
Formamide	simplest amide	NH$_2$CHO
Inorganic Molecule		
Hydroxyl amine	-	NH$_2$OH

Table 3.3: Molecules considered in this work

Note: For the sake of convenience, COMs will most of the times be used to refer

to all the molecules, (including the inorganic molecule hydroxyl amine) when employed generally.

To predict the abundances of the different COMs in the HD100546 disk, the output of the gas-grain chemical model previously ran by Booth et al. [2021b] over the physical structure, specific to the disk by Kama et al. [2016], shown in Figure 3.2.3 from Booth et al. [2021b], is quantified, and the plots of the column densities and fractional abundances of the gas-phase and grain-surface species at four different time-stamps are provided in this section.
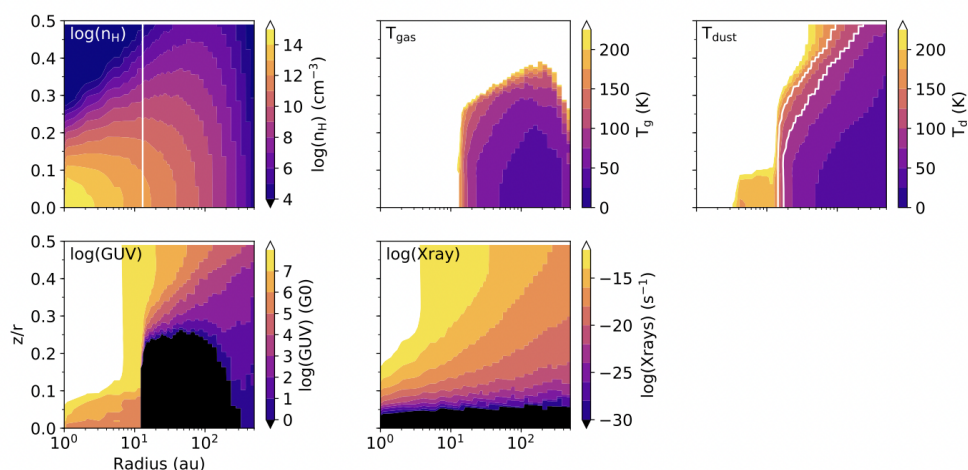
Figure 3.3: Model of HD 100546 disk from Kama et al. [2016], reported in Booth et al. [2021b]; top, left to right: the n_H density (cm^{-3}), gas temperature (K), dust temperature (K); bottom, left to right: UV field (in units of the interstellar radiation field, G_0) and X-ray ionization rate (s^{-1}). The white contours denote the T$_{dust}$ of 100 K and 150 K, and the location of the dust cavity

In order to trace the radial mass distribution in the disk and to determine the species sensitive to each chemical process, the radial column densities of each species in both the gas and grain states are computed at 1 Myr, 2 Myr, 5 Myr and 8 Myr, thereby giving an evolution with time of the abundances of the different species in the disk. The column density, N_i, at each radius, r, for each species, i, is calculated by integrating the number density over the depth of the disk:

$$N_i(r) = \int_{z_{-\infty}}^{z_{+\infty}} n_i(r,z)dz cm^{-2} \tag{3.9}$$

3.3 Results

This section provides the plots of the column densities of the species in both the gas and ice state at 1 Myr, 2 Myr, 5 Myr and 8 Myr, and their fractional abundances at 1 Myr, 2 Myr and 5 Myr (fractional abundances at 8 Myr were not included as the colour maps were not successfully plotted for some of the molecules at this timestamp).

3.3.1 Column Densities of COMs as a Function of Time in the HD 100546 Protoplanetary Disk

Figures 3.3.1 and 3.3.1 display the column densities of gas-phase (solid lines) and grain-surface (dotted lines) species as a function of radius at 1 Myr, 2 Myr, 5 Myr and 8 Myr.
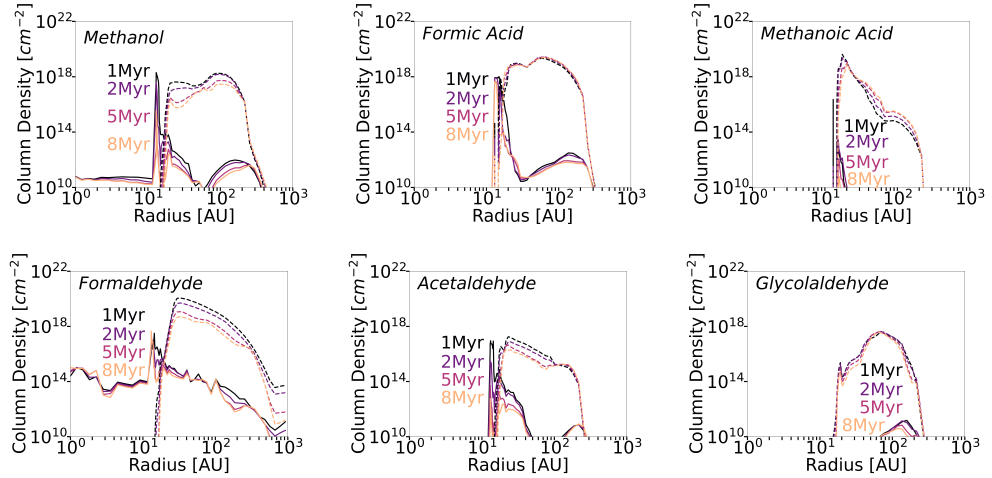
Figure 3.4: Column densities of COMs at 1 Myr, 2 Myr, 5 Myr and 8 Myr - solid lines: gas-phase, dotted lines: grain-surface
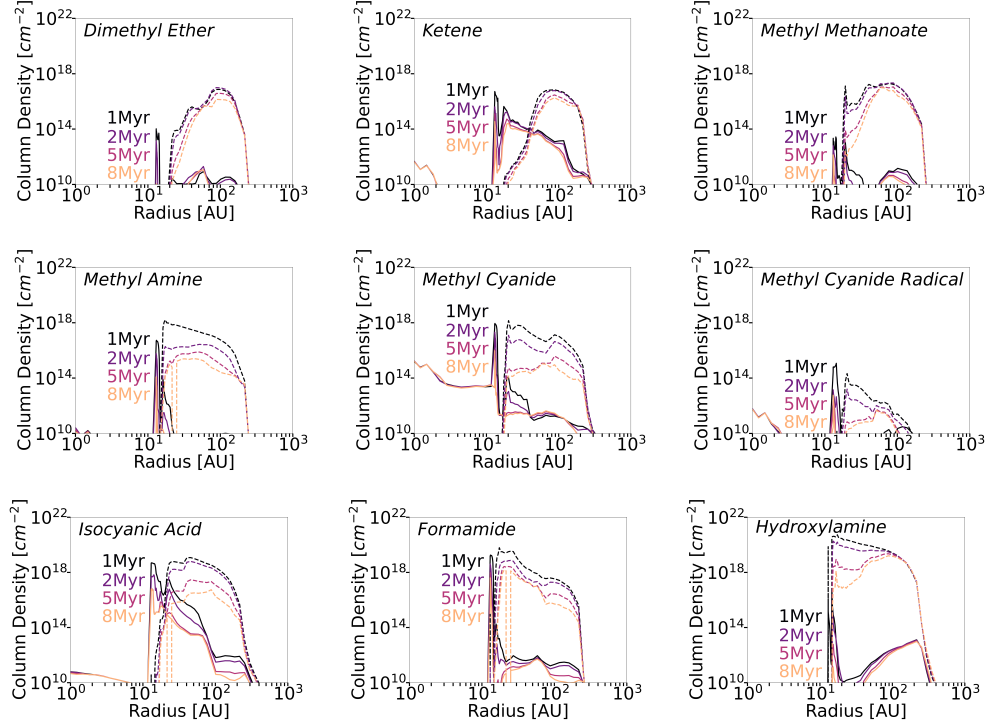
Figure 3.5: Column densities of COMs at 1 Myr, 2 Myr, 5 Myr and 8 Myr - solid lines: gas-phase, dotted lines: grain-surface - *continued*

Substantial reservoirs (reaching as high as 10^{19} cm^{-2} in the gas state and 10^{20} cm^{-2} in the ice state) of COMs in both the gas and ice states are seen in disk with little depletion in most of them over the years. In the gas state, formaldehyde (H$_2$CO) is seen to be appreciably abundant (with its maximum reaching 1.1×10^{20} cm^{-2} at 33 au) over the whole range of radii. It is followed by methyl cyanide, CH$_3$CN (a maximum of 1.4×10^{18} cm^{-2} at 20 au) which gets relatively more scarce in the outer disk. Larger organics, such as methanoic acid (CH$_3$COOH), dimethyl ether (CH$_3$OCH$_3$), glycolaldehyde (CH$_2$OHCHO) are among the least abundant in the gas state over the years, with the lowest maximum column density being that of glycolaldehyde at 3.8×10^{10} cm^{-2} at 117 au at 8 Myr. Ice-state COMs are seen in significant reservoirs in the outer disk, with the exception of the methyl cyanide radical (CH$_2$CN). The co-existence of the gas and ice states of the COMs is also seen, with the radial ice-to-gas ratio of the COMs reaching as high as 0.5 for formaldehyde (H$_2$CO), ketene (CH$_2$CO) and isocyanic acid (HNCO).

The maximum column densities of gas-phase COMs vary from as high as 1.8×10^{19} cm^{-2} for nitrogen- and oxygen-bearing COM, formamide, NH$_2$CHO, (making it the most abundant gas-phase COM of those considered) at 1 Myr to as low as 3.8×10^{10} cm^{-2} for glycolaldehyde, CH$_2$OHCHO, (thereby, the least abundant) at 8 Myr. In the ice state, the peak column densities range from 5.3×10^{20} cm^{-2} for formamide at 1 Myr to 4.6×10^{11} cm^{-2} for methyl cyanide radical at 8 Myr. With the exception of the latter, all the COMs are seen to be more abundant in the ice state at almost all timestamps. The column densities of the gas-phase COMs peak closer to the star for all timestamps, mostly in the range of 13-16 au. The maxima of the column densities of the oxygen-bearing COMs in the ice state are located further out (within 50 au to 100 au) in the disk at all timestamps, except for formaldehyde (33 au), acetaldehyde (23 au) and methanoic acid (17-20 au). As for the ice-state nitrogen-bearing COMs, the column densities of all of them peak relatively closer to the star, with the closest being 17 au (at which most of the nitrogen-bearing COMs peak) and 15 au for the inorganic hydroxyl amine, NH$_2$OH at 2 Myr.

As we progress over the years from 1 Myr to 8 Myr, a general decrease in the maximum column densities of all the gas-phase species is noted, with a more significant decline of up to 4 orders of magnitude (for the oxygen-bearing organic COM, acetaldehyde, CH$_3$CHO, from 9.0×10^{16} cm^{-2} at 1 Myr to 5.7×10^{12} cm^{-2} at 8 Myr; and the inorganic molecule, hydroxyl amine from 6.0×10^{16} cm^{-2} at 1 Myr to 9.7×10^{12} cm^{-2} at 8 Myr) in the gas state. As for oxygen-bearing COMs in the ice state, the maximum column densities are not seen to change significantly, with net decreases of at most one order of magnitude from 1 Myr to 8 Myr, except for formaldehyde which goes from 1.1×10^{20} cm^{-2} at 1 Myr to 5.1×10^{18} cm^{-2} at 8 Myr. On the other hand, the peak column density of ice-state nitrogen-bearing COMs suffer significant decreases by three orders of magnitude, the maximum decrease being that of methyl cyanide from 1.4×10^{18} cm^{-2} at 1 Myr to 1.1×10^{15} cm^{-2} at 8 Myr. Contrarily to its gas state, hydroxyl amine in the ice bears a relatively small decrease in its peak column density, going from 5.3×10^{20} cm^{-2} at 1 Myr to 1.6×10^{19} cm^{-2} at 8 Myr.

Table 3.4 outlines the radii, r/au, at which the column densities, y/cm^{-2} peak for each molecule in both the gas and ice states at each timestamp. In order to assess the gradient of the change at different regions of the disk, the column densities at 1 au, 11 au and 100 au at each timestamp for all the molecules in both the gas and ice states

are reported in tables 3.5, 3.6 and 3.7. As seen in the column density graphs, most molecules have reached steady state by 1 Myr as their abundances remain of the same order of magnitude over the years at the three chosen radii, except at 100 au, where the maximum column density of methanol gas and ice, formaldehyde ice, methyl cyanide ice decreases by at most three orders of magnitude; and that of the two carboxylic acids ices see increases by one order of magnitude. These changes are discussed in section 3.4, where elaboration on the chemistry is provided. The largest gradient of change is seen at 100 au with methyl cyanide ice decreasing from 1.0×10^{17} cm^{-2} at 1 Myr to 3.5×10^{14} cm^{-2} at 8 Myr.

Molecule	1 Myr		2 Myr		5 Myr		8 Myr	
	y/cm^{-2}	r/au	y/cm^{-2}	r/au	y/cm^{-2}	r/au	y/cm^{-2}	r/au
Methanol$_{gas}$	2.0×10^{18}	13.0	3.7×10^{17}	13.0	6.8×10^{14}	13.0	3.4×10^{15}	13.0
Methanol$_{ice}$	1.7×10^{18}	87.8	1.4×10^{18}	101	5.4×10^{17}	101	2.8×10^{17}	101
Formaldehyde$_{gas}$	3.1×10^{17}	14.4	6.8×10^{16}	13.1	1.7×10^{17}	13.0	4.6×10^{17}	13.0
Formaldehyde$_{ice}$	1.1×10^{20}	32.7	4.9×10^{19}	32.7	1.2×10^{19}	32.7	5.1×10^{18}	32.7
Acetaldehyde$_{gas}$	9.0×10^{16}	13.2	3.2×10^{15}	13.1	5.4×10^{13}	13.1	5.7×10^{12}	13.1
Acetaldehyde$_{ice}$	1.8×10^{17}	23.1	7.5×10^{16}	23.1	4.4×10^{16}	23.1	2.1×10^{16}	21.6
Glycolaldehyde$_{gas}$	1.5×10^{11}	159	1.4×10^{11}	136	6.7×10^{10}	136	3.8×10^{10}	117
Glycolaldehyde$_{ice}$	3.3×10^{17}	66.6	4.4×10^{17}	66.6	4.0×10^{17}	66.6	3.7×10^{17}	66.6
Methyl Methanoate$_{gas}$	2.7×10^{13}	14.2	6.2×10^{12}	13.0	1.0×10^{12}	13.1	1.4×10^{12}	13.0
Methyl Methanoate$_{ice}$	2.0×10^{17}	76.3	2.2×10^{17}	87.8	1.1×10^{17}	87.8	9.8×10^{16}	58.4
Ketene$_{gas}$	5.2×10^{16}	13.1	4.0×10^{15}	13.1	1.2×10^{15}	13.1	3.5×10^{14}	13.1
Ketene$_{ice}$	6.8×10^{16}	87.8	6.0×10^{16}	87.8	2.9×10^{16}	87.8	1.8×10^{16}	87.8
Dimethyl Ether$_{gas}$	1.0×10^{14}	13.0	1.4×10^{13}	13.0	1.2×10^{11}	58.4	1.1×10^{11}	58.4
Dimethyl Ether$_{ice}$	7.3×10^{16}	101	9.8×10^{16}	87.8	3.8×10^{16}	101	1.4×10^{16}	87.8
Formic Acid$_{gas}$	1.0×10^{18}	14.9	8.2×10^{17}	13.1	4.9×10^{17}	13.1	4.5×10^{17}	13.1
Formic Acid$_{ice}$	2.1×10^{19}	58.4	2.6×10^{19}	58.4	2.6×10^{19}	66.6	2.5×10^{19}	66.6
Methanoic Acid$_{gas}$	4.4×10^{13}	13.0	3.2×10^{13}	15.3	1.1×10^{12}	15.7	6.3×10^{10}	15.7
Methanoic Acid$_{ice}$	4.1×10^{19}	17.4	2.2×10^{19}	17.4	1.1×10^{19}	20.3	8.7×10^{18}	20.3
Methyl Amine$_{gas}$	5.3×10^{16}	13.1	5.9×10^{15}	13.1	9.0×10^{13}	13.1	1.2×10^{14}	13.1
Methyl Amine$_{ice}$	1.6×10^{18}	17.4	2.7×10^{16}	51.4	7.6×10^{15}	51.4	2.5×10^{15}	40.5
Methyl Cyanide$_{gas}$	8.8×10^{17}	13.1	2.0×10^{17}	13.1	8.8×10^{16}	25.5	8.8×10^{16}	25.5
Methyl Cyanide$_{ice}$	1.4×10^{18}	20.3	1.2×10^{17}	20.3	3.9×10^{15}	87.8	1.1×10^{15}	58.4
Methyl Cyanide Radical$_{gas}$	1.2×10^{15}	14.4	3.0×10^{13}	0.26	3.0×10^{13}	0.26	3.0×10^{13}	0.26
Methyl Cyanide Radical$_{ice}$	2.1×10^{14}	20.3	1.6×10^{13}	20.3	5.4×10^{11}	51.4	4.6×10^{11}	51.4
Isocyanic Acid$_{gas}$	4.9×10^{18}	13.2	6.7×10^{17}	14.2	6.5×10^{16}	13.3	6.4×10^{16}	13.1
Isocyanic Acid$_{ice}$	1.2×10^{19}	45.5	6.3×10^{18}	45.5	2.9×10^{17}	45.5	5.5×10^{16}	87.8
Formamide$_{gas}$	1.8×10^{19}	13.1	4.0×10^{18}	13.1	9.3×10^{17}	13.1	4.0×10^{17}	13.1
Formamide$_{ice}$	6.1×10^{19}	17.4	7.3×10^{18}	25.0	2.7×10^{18}	20.3	1.5×10^{18}	20.3
Hydroxyl Amine$_{gas}$	6.0×10^{16}	14.6	1.3×10^{15}	14.9	1.1×10^{13}	216	9.7×10^{12}	216
Hydroxyl Amine$_{ice}$	5.3×10^{20}	17.4	1.8×10^{20}	15.3	2.2×10^{19}	87.8	1.6×10^{19}	87.8

Table 3.4: Maximum column densities of the different COMs in both the gas and ice states and the corresponding radii at 1 Myr, 2 Myr, 5 Myr and 8 Myr

Molecule	Radius/au	1 Myr	2 Myr	5 Myr	8 Myr
Methanol	1	6.2×10^{10}	5.9×10^{10}	5.6×10^{10}	5.5×10^{10}
gas	11	4.2×10^{10}	2.4×10^{10}	1.8×10^{10}	1.6×10^{10}
CH_3OH	100	2.8×10^{11}	1.8×10^{11}	6.3×10^{10}	3.6×10^{10}
Methanol	1	-	-	-	-
ice	11	5.3×10^{-21}	-	-	9.6×10^{-13}
GCH_3OH	100	1.7×10^{18}	1.4×10^{18}	5.4×10^{17}	2.8×10^{17}
Formaldehyde	1	2.6×10^{14}	6.0×10^{14}	4.9×10^{14}	1.0×10^{15}
gas	11	9.6×10^{13}	8.1×10^{13}	6.8×10^{13}	6.2×10^{13}
H_2CO	100	1.5×10^{14}	1.2×10^{14}	1.3×10^{14}	1.5×10^{14}
Formaldehyde	1	-	-	-	-
ice	11	1.1×10^{-17}	1.3×10^{-14}	-	2.5×10^{-21}
GH_2CO	100	1.1×10^{19}	5.5×10^{18}	1.3×10^{18}	6.8×10^{17}
Acetaldehyde	1	3.3×10^{3}	4.1×10^{3}	3.5×10^{3}	4.0×10^{3}
gas	11	4.7×10^{4}	6.8×10^{4}	7.2×10^{4}	6.0×10^{4}
CH_3CHO	100	4.7×10^{9}	3.3×10^{9}	2.5×10^{9}	2.2×10^{9}
Acetaldehyde	1	-	-	-	-
ice	11	-	-	-	-
GCH_3CHO	100	1.8×10^{15}	1.7×10^{15}	1.5×10^{15}	1.3×10^{15}
Glycolaldehyde	1	2.9×10^{-3}	1.2×10^{-2}	2.3×10^{-3}	2.1×10^{-3}
gas	11	4.6×10^{-7}	1.6×10^{-5}	7.6×10^{-6}	5.0×10^{-7}
CH_2OHCHO	100	4.4×10^{10}	4.3×10^{10}	3.0×10^{10}	2.7×10^{10}
Glycolaldehyde	1	-	-	-	-
ice	11	8.5×10^{-28}	-	-	-
GCH_2OHCHO	100	1.6×10^{17}	1.7×10^{17}	1.2×10^{17}	1.0×10^{17}
Methyl Methanoate	1	4.3×10^{2}	1.5×10^{3}	8.2×10^{2}	2.3×10^{3}
gas	11	8.3	7.2	5.5	4.1
$HCOOCH_3$	100	1.4×10^{11}	8.3×10^{10}	3.0×10^{10}	2.0×10^{10}
Methyl Methanoate	1	-	-	-	-
ice	11	-	-	-	-
$GHCOOCH_3$	100	1.2×10^{17}	1.2×10^{17}	5.0×10^{16}	2.4×10^{16}

Table 3.5: Column densities, in cm^{-2}, of the different species at 1 au, 11 au and 100 au at 1 Myr, 2 Myr, 5 Myr and 8 Myr

Molecule	Radius/au	1 Myr	2 Myr	5 Myr	8 Myr
Ketene	1	4.3×10^{11}	4.7×10^{11}	4.3×10^{11}	4.2×10^{11}
gas	11	8.2×10^{7}	9.6×10^{7}	1.1×10^{8}	1.0×10^{8}
CH_2CO	100	1.4×10^{13}	9.3×10^{12}	3.9×10^{12}	2.7×10^{12}
Ketene	1	-	-	-	-
ice	11	-	-	-	-
GCH_2CO	100	5.6×10^{16}	5.0×10^{16}	2.1×10^{16}	1.2×10^{16}
Formic Acid	1	1.1×10^{8}	9.1×10^{7}	6.5×10^{7}	6.0×10^{7}
gas	11	1.5×10^{7}	1.2×10^{7}	9.1×10^{6}	8.1×10^{6}
$HCOOH$	100	1.2×10^{12}	9.8×10^{11}	5.9×10^{11}	5.1×10^{11}
Formic Acid	1	-	-	-	-
ice	11	-	-	-	-
$GHCOOH$	100	7.1×10^{18}	9.3×10^{18}	1.1×10^{19}	1.1×10^{19}
Methanoic Acid	1	4.8×10^{-6}	1.1×10^{-86}	2.3×10^{-6}	1.7×10^{-9}
gas	11	2.0×10^{-6}	-	7.9×10^{-17}	-
CH_3COOH	100	1.4×10^{8}	2.0×10^{8}	2.8×10^{8}	2.8×10^{8}
Methanoic Acid	1	-	-	-	-
ice	11	-	-	-	-
GCH_3COOH	100	5.3×10^{14}	1.1×10^{15}	2.3×10^{15}	2.6×10^{15}
Dimethyl Ether	1	2.8×10^{-3}	4.3×10^{-3}	2.5×10^{-3}	2.4×10^{-3}
gas	11	2.9×10^{-3}	3.3×10^{-3}	3.0×10^{-3}	2.4×10^{-3}
CH_3OCH_3	100	2.4×10^{10}	1.4×10^{10}	3.7×10^{9}	1.6×10^{9}
Dimethyl Ether	1	-	-	-	-
ice	11	-	-	-	-
GCH_3OCH_3	100	7.3×10^{16}	9.5×10^{16}	3.8×10^{16}	1.3×10^{16}
Isocyanic Acid	1	6.1×10^{10}	5.8×10^{10}	5.1×10^{10}	4.5×10^{10}
gas	11	5.4×10^{9}	5.4×10^{9}	5.4×10^{9}	5.4×10^{9}
$HNCO$	100	6.6×10^{11}	3.1×10^{11}	6.4×10^{10}	3.9×10^{10}
Isocyanic Acid	1	-	3.6×10^{-20}	-	-
ice	11	4.4×10^{-19}	-	-	-
$GHNCO$	100	2.2×10^{18}	1.3×10^{18}	1.1×10^{17}	1.7×10^{16}

Table 3.6: Column densities, in cm^{-2}, of the different species at 1 au, 11 au and 100 au at 1 Myr, 2 Myr, 5 Myr and 8 Myr - *continued*

Molecule	Radius/au	1 Myr	2 Myr	5 Myr	8 Myr
Formamide	1	2.0×10^9	3.6×10^9	2.7×10^9	3.9×10^9
gas	11	3.4×10^6	3.4×10^6	3.7×10^6	3.9×10^6
NH_2CHO	100	2.1×10^{11}	1.3×10^{11}	3.3×10^{10}	1.7×10^{10}
Formamide	1	-	-	-	-
ice	11	-	-	-	-
GNH_2CHO	100	3.4×10^{17}	1.9×10^{17}	2.7×10^{16}	5.0×10^{15}
Methyl Cyanide	1	1.5×10^{15}	1.7×10^{15}	1.6×10^{15}	1.6×10^{15}
gas	11	2.5×10^{13}	2.9×10^{13}	3.3×10^{13}	3.1×10^{13}
CH_3CN	100	1.5×10^{11}	1.6×10^{11}	1.6×10^{11}	1.7×10^{11}
Methyl Cyanide	1	-	-	-	-
ice	11	-	-	-	-
GCH_3CN	100	1.0×10^{17}	3.2×10^{16}	2.5×10^{15}	3.5×10^{14}
Methyl Cyanide Radical	1	5.2×10^{11}	5.9×10^{11}	5.3×10^{11}	5.4×10^{11}
gas	11	4.3×10^9	3.7×10^9	2.2×10^9	1.7×10^9
CH_2CN	100	2.3×10^{10}	5.4×10^9	9.0×10^8	5.5×10^8
Methyl Cyanide Radical	1	-	-	-	-
ice	11	-	-	-	-
GCH_2CN	100	2.5×10^{11}	7.6×10^{10}	1.6×10^{10}	9.2×10^9
Methyl Amine	1	1.4×10^{10}	2.5×10^{10}	1.8×10^{10}	1.3×10^{10}
gas	11	8.2×10^8	2.8×10^8	2.3×10^8	2.2×10^8
CH_3NH_2	100	9.1×10^9	3.7×10^9	8.4×10^8	5.1×10^8
Methyl Amine	1	-	-	-	-
ice	11	-	-	-	-
GCH_3NH_2	100	5.5×10^{16}	9.1×10^{15}	9.4×10^{14}	2.5×10^{14}
Hydroxyl Amine	1	0.18	0.14	1.5×10^{-5}	3.5×10^{-5}
gas	11	2.7×10^{-25}	4.1×10^{-8}	6.5×10^{-3}	1.9×10^{-5}
NH_2OH	100	2.7×10^{12}	2.6×10^{12}	2.0×10^{12}	1.6×10^{12}
Hydroxyl Amine	1	-	-	-	-
ice	11	-	-	-	-
GNH_2OH	100	2.5×10^{19}	2.3×10^{19}	1.9×10^{19}	1.5×10^{19}

Table 3.7: Column densities, in cm^{-2}, of the different species at 1 au, 11 au and 100 au at 1 Myr, 2 Myr, 5 Myr and 8 Myr - *continued*

3.3.2 Fractional Abundances of COMs as a Function of Time in the HD 100546 Protoplanetary Disk

In this subsection, the colour maps of the fractional abundances of the different species in both the gas and ice states at 1 Myr, 2 Myr and 5 Myr are provided. A description of the variation of the fractional abundances is also provided for both gas and ice states, with particular attention to the maxima and their locations in the disk.

Fractional Abundances of Gas-Phase COMs at 1 Myr, 2 Myr and 5 Myr in the HD 100546 Protoplanetary Disk

Figures 3.3.2, 3.3.2 and 3.3.2 show the fractional abundances of COMs (relative to the total number density) as a function of disk radius, r and height, z/r, for gas-phase species at 1 Myr, 2 Myr and 5 Myr. For all the species, the maximum fractional abundance of their gas state generally decrease as we progress from 1 Myr to 5 Myr.
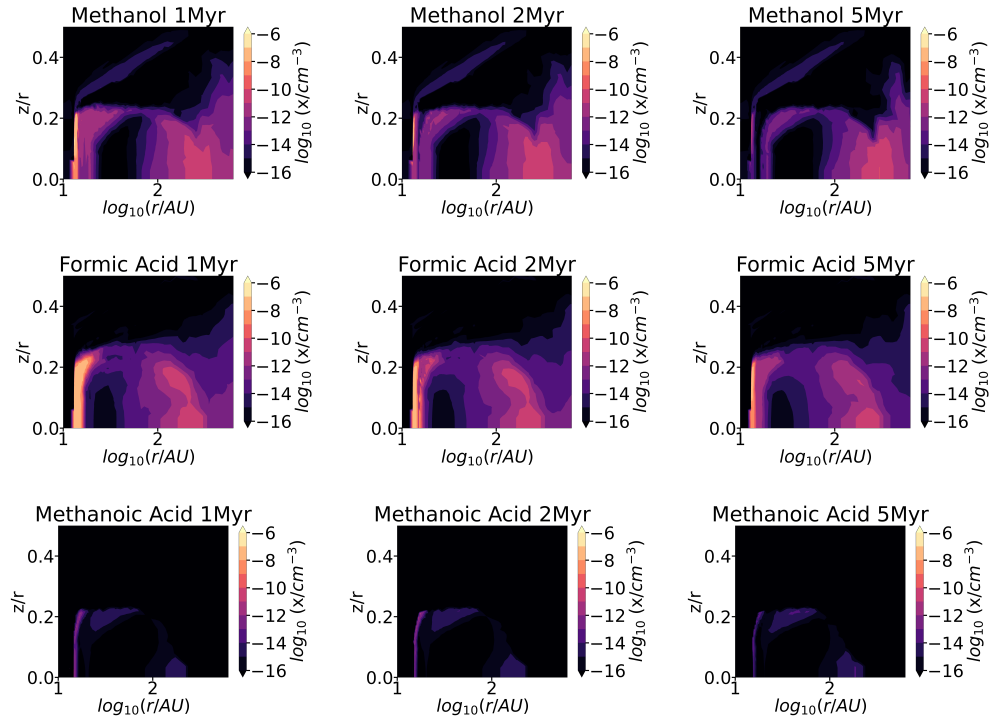
Figure 3.6: Fractional abundances of gas-phase COMs at 1 Myr, 2 Myr and 5 Myr
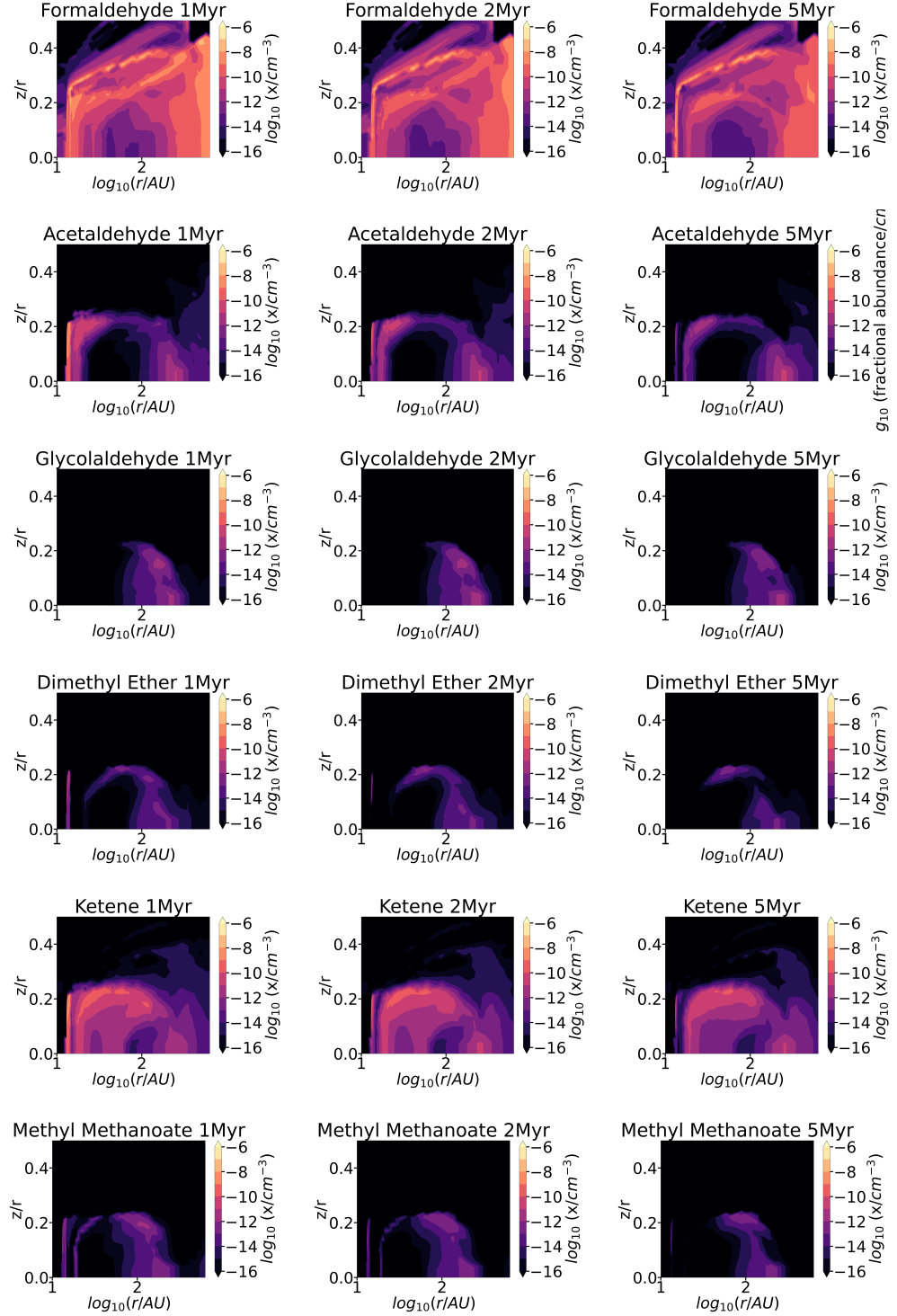
Figure 3.7: Fractional abundances of gas-phase COMs at 1 Myr, 2 Myr and 5 Myr - *continued*
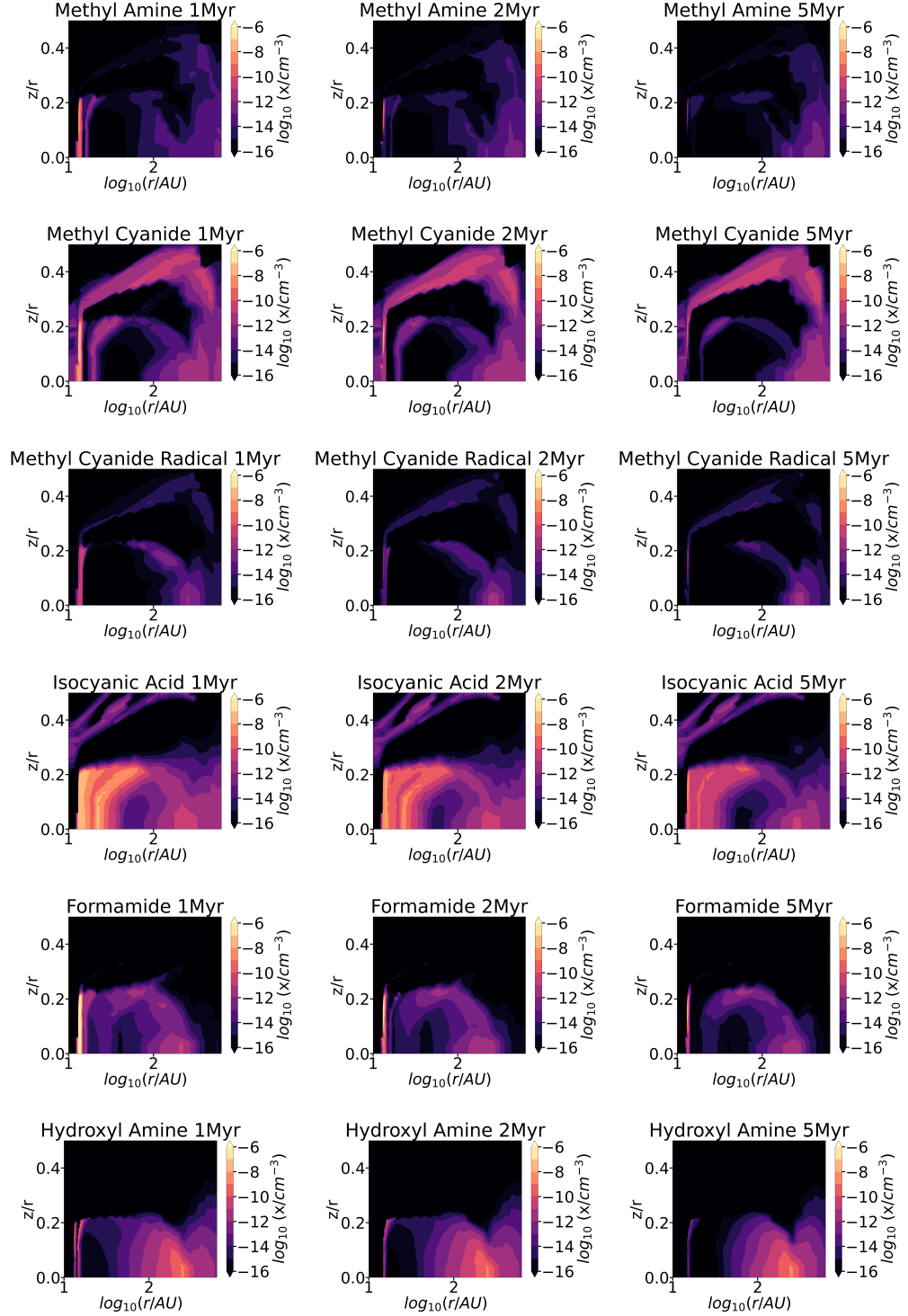
Figure 3.8: Fractional abundances of gas-phase COMs at 1 Myr, 2 Myr and 5 Myr - *continued*

Glycolaldehyde, formic acid, formamide and hydroxyl amine have the least signific-
ant changes in their peak fractional abundances with the latter being of the same order
of magnitude over the years. The molecules to suffer the most significant decrease in
their fractional abundance (of three orders of magnitude) over the years from 1 Myr to
5 Myr are methanol which goes from 1.8×10^{-7} cm^{-3} at 1 Myr to 5.4×10^{-10} cm^{-3}
at 5 Myr, and acetaldehyde, from 1.2×10^{-8} cm^{-3} at 1 Myr to 1.9×10^{-11} cm^{-3} at
5 Myr. The most abundant molecule in the gas state at all three timestamps is the
N- and O-bearing organic molecule formamide which peaks at 4.7×10^{-7} cm^{-3} at 1
Myr to 2.3×10^{-7} cm^{-3} at 5 Myr, at the constant location of (185, 6.42) in (r,z) co-
ordinates. The least abundant molecule in the gas state is methanoic acid at 1 Myr,
peaking at 4.7×10^{-12}cm^{-3}. The maximum fractional abundances of most species in
the gas state at all the timestamps occur very close to the star (from 13 au to 15 au
radially outwards, with most molecules peaking at the closest radius of 13 au) and to
the midplane (within 3 au vertically). Table 3.8 gives the coordinates of the points (r,z)
for the radius from the star and the height above the midplane respectively at which
the fractional abundances, x/cm^{-3}, of the different species peak in the gas state at 1
Myr, 2 Myr and 5 Myr.

GAS	*1 Myr*			*2 Myr*			*5 Myr*		
Molecule	**x/cm^{-3}**	**r/au**	**z/au**	**x/cm^{-3}**	**r/au**	**z/au**	**x/cm^{-3}**	**r/au**	**z/au**
Methanol	1.8×10^{-7}	13.0	1.32	4.2×10^{-8}	13.0	1.47	5.4×10^{-10}	13.1	2.10
Formaldehyde	1.1×10^{-7}	924	431	5.0×10^{-8}	40.5	13.1	5.4×10^{-8}	101	37.3
Acetaldehyde	1.2×10^{-8}	14.4	1.84	5.8×10^{-10}	13.5	2.84	1.9×10^{-11}	13.1	2.27
Glycolaldehyde	3.2×10^{-12}	159	23.0	3.7×10^{-12}	216	7.80	2.4×10^{-12}	216	7.80
Formic Acid	2.5×10^{-8}	14.9	2.85	1.6×10^{-8}	13.3	1.35	1.8×10^{-8}	13.2	2.13
Methanoic Acid	4.7×10^{-12}	13.0	0.39	2.2×10^{-12}	17.4	3.68	5.5×10^{-11}	348	448
Methyl Methanoate	2.1×10^{-12}	13.0	1.32	7.8×10^{-13}	216	7.80	6.0×10^{-13}	216	7.80
Dimethyl Ether	2.0×10^{-11}	14.0	2.97	1.8×10^{-12}	58.4	12.6	4.2×10^{-9}	348	448
Ketene	1.6×10^{-8}	14.2	3.01	7.86×10^{-10}	13.1	2.27	5.8×10^{-10}	13.1	2.27
Methyl Amine	2.1×10^{-9}	13.0	1.786	6.3×10^{-10}	13.0	1.786	6.0×10^{-11}	13.1	2.27
Methyl Cyanide	4.2×10^{-8}	13.1	1.94	2.71×10^{-8}	13.1	1.94	5.7×10^{-9}	13.0	1.94
Methyl Cyanide Radical	4.7×10^{-11}	14.4	1.84	4.1×10^{-12}	13.1	2.26	2.0×10^{-12}	297	11.6
Isocyanic Acid	1.1×10^{-7}	14.4	1.84	1.5×10^{-8}	14.2	2.67	7.5×10^{-9}	13.4	2.64
Formamide	4.4×10^{-7}	13.0	1.32	3.8×10^{-7}	13.0	1.47	2.3×10^{-7}	13.1	1.94
Hydroxyl Amine	4.4×10^{-9}	14.6	2.24	1.3×10^{-9}	253	9.50	1.4×10^{-9}	253	9.50

Table 3.8: Peak fractional abundances of each molecule in the gas state and the loca-
tions at which they occur at 1 Myr, 2 Myr and 5 Myr

Fractional Abundances of Grain-Surface COMs at 1 Myr, 2 Myr and 5 Myr in the HD 100546 Protoplanetary Disk

Figures 3.3.2, 3.3.2 and 3.3.2 show the fractional abundances of COMs (relative to the total number density) as a function of disk radius, r and height, z/r, for grain-surface species at 1 Myr, 2 Myr and 5 Myr.
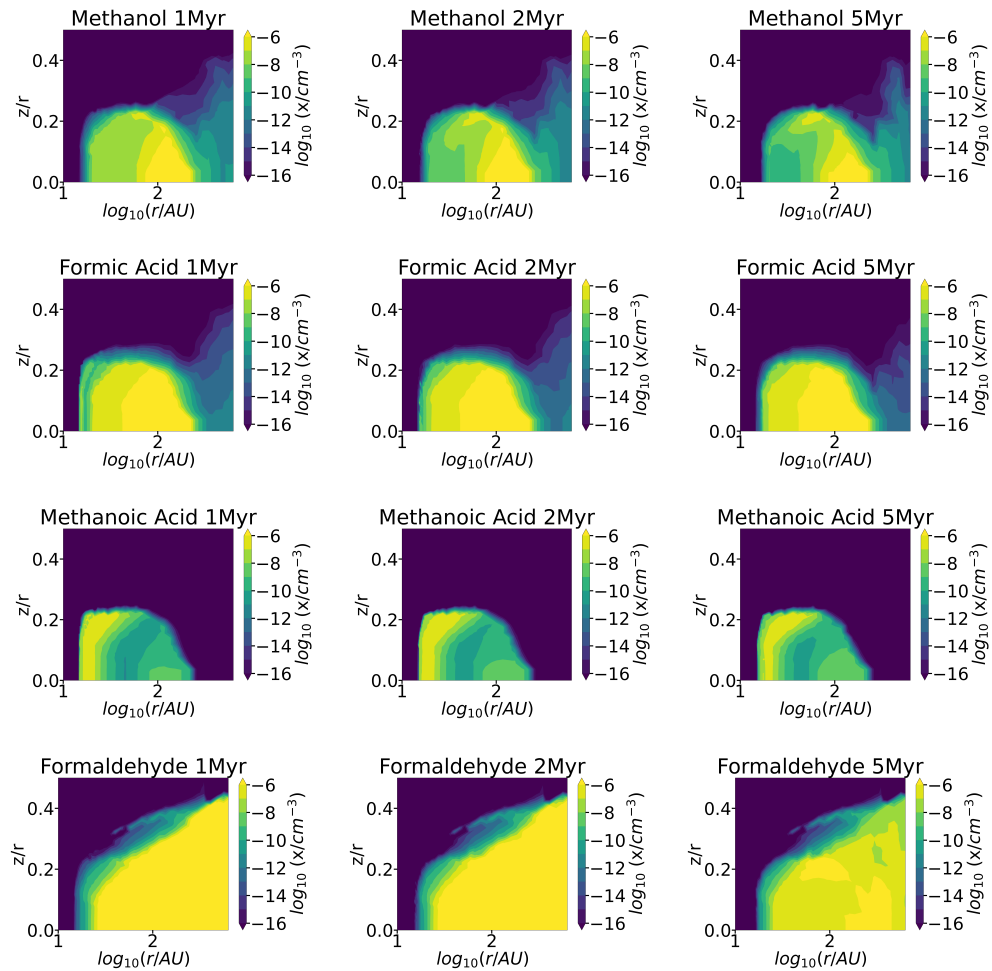
Figure 3.9: Fractional abundances of grain-surface COMs at 1 Myr, 2 Myr and 5 Myr
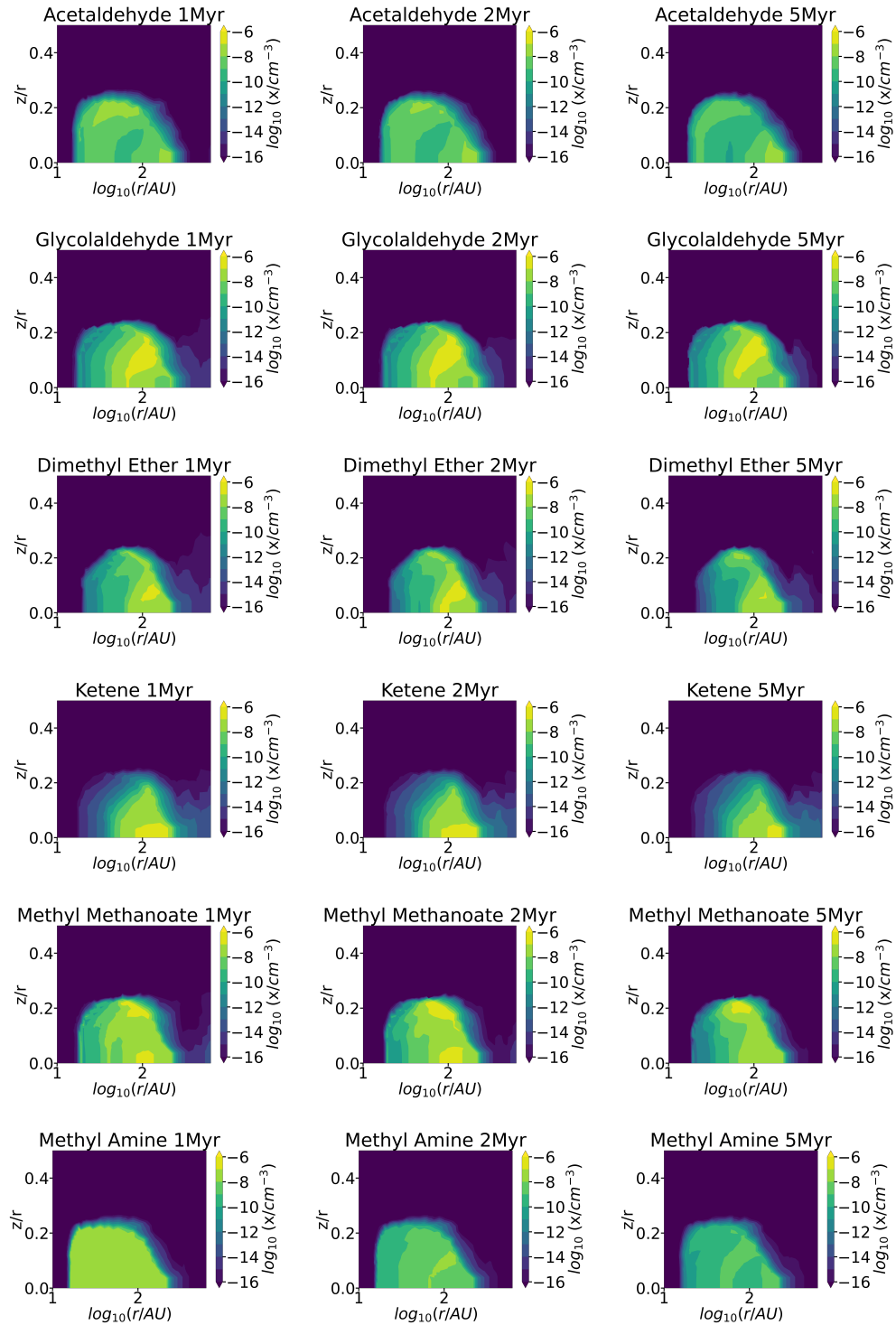
Figure 3.10: Fractional abundances of grain-surface COMs at 1 Myr, 2 Myr and 5 Myr - *continued*
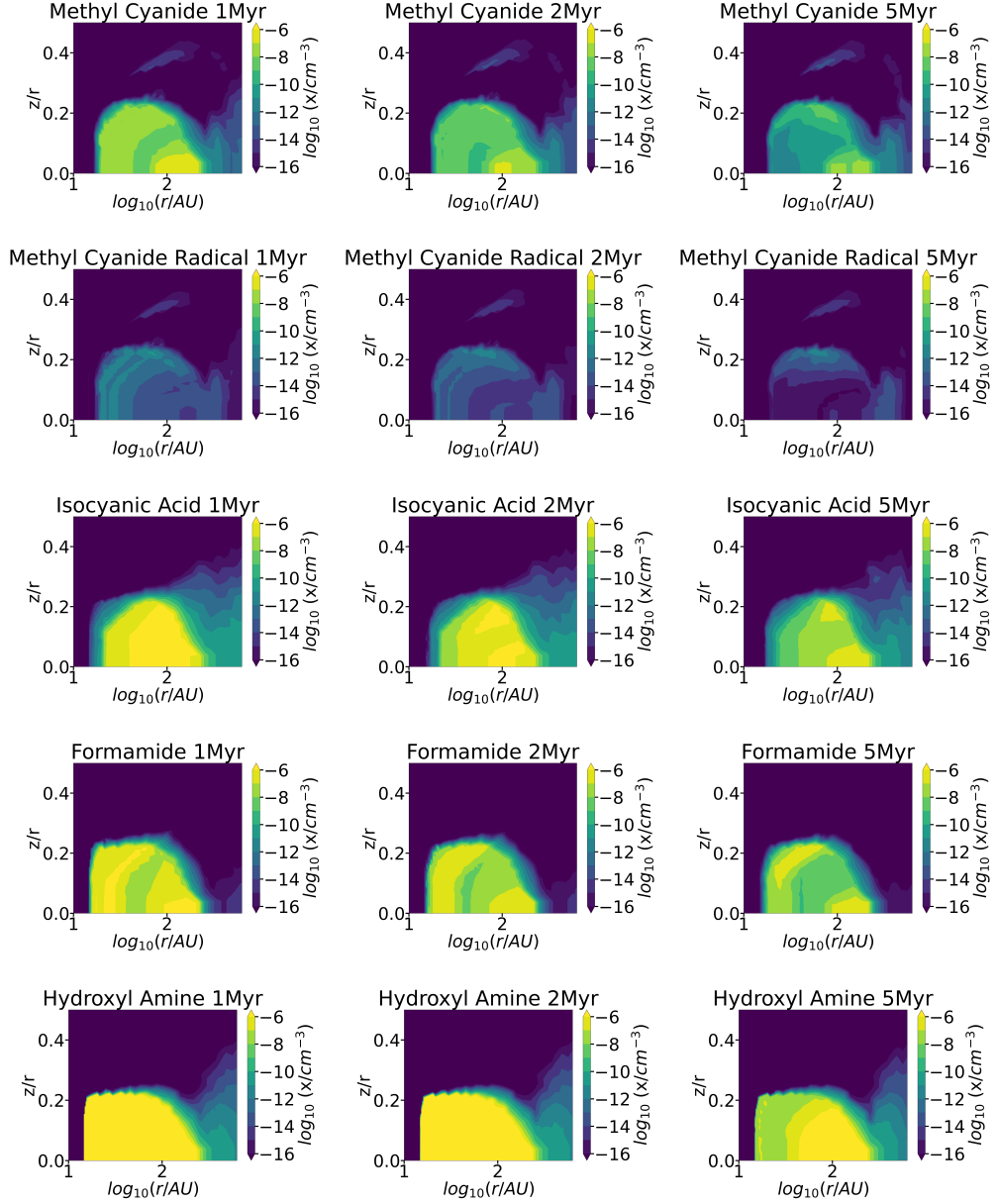
Figure 3.11: Fractional abundances of grain-surface COMs at 1 Myr, 2 Myr and 5 Myr - *continued*

For most of the species, little to almost no variation is seen in the maximum fractional abundance of their ice state as we progress from 1 Myr to 5 Myr. The most abundant molecule in the ice-state at all three timestamps is the inorganic molecule

hydroxyl amine which peaks at $\sim 10^{-5}$ cm^{-3} at (185, 6.42) in (r,z) coordinates. The most abundant organic molecule in the ice state is formaldehyde which peaks at the same order of magnitude at (76.3, 16.3). The least abundant molecule in the ice state is methyl cyanide radical, with a maximum fractional abundance of $\sim 10^{-11}$ cm^{-3}, with the peak moving closer to the star and the midplane with time from (66.6, 14.9) at 1 Myr to (51.4, 11.7) at 5 Myr. The maximum fractional abundances of all the species in the ice state occurs from as close to the star as 18 au for methanoic acid at 1 Myr to as far as 216 au for methyl amine at 5 Myr. The maxima of the fractional abundances are located from 2.24 au from the midplane where methanoic acid peaks at 1 Myr to 20.6 au where formic acid peaks at 1 Myr and glycolaldehyde at 5 Myr. Where the fractional abundances peak for the different species in the ice state varies for almost all of them with time. As we move from 1 Myr to 5 Myr, the peak fractional abundance occurs further out from the star and higher up from the midplane for most of them. Of all locations at which the fractional abundances of the different species in the ice state peak over the years, (185, 6.42) is where most maxima are witnessed - *See Table 3.9 for further quantitative details.*

ICE	1 Myr			2 Myr			5 Myr		
Molecule	**x/cm^{-3}**	**r/au**	**z/au**	**x/cm^{-3}**	**r/au**	**z/au**	**x/cm^{-3}**	**r/au**	**z/au**
Methanol	3.9×10^{-6}	159	12.4	3.7×10^{-6}	159	12.4	3.1×10^{-6}	185	6.42
Formaldehyde	2.2×10^{-5}	76.3	16.3	1.9×10^{-5}	76.3	16.3	1.3×10^{-5}	76.3	16.3
Acetaldehyde	4.2×10^{-8}	45.5	10.0	2.8×10^{-8}	185	6.42	4.2×10^{-8}	185	6.42
Glycolaldehyde	4.1×10^{-7}	136	19.0	6.4×10^{-7}	136	19.0	4.8×10^{-7}	117	20.6
Formic Acid	1.0×10^{-5}	117	20.6	1.6×10^{-5}	185	6.42	2.9×10^{-5}	185	6.42
Methanoic Acid	7.1×10^{-7}	18.2	2.24	4.5×10^{-7}	19.1	2.64	5.1×10^{-7}	29.7	5.43
Methyl Methanoate	7.3×10^{-7}	76.3	16.3	9.0×10^{-7}	87.8	17.7	6.2×10^{-7}	87.8	17.7
Dimethyl Ether	1.3×10^{-7}	136	10.2	1.8×10^{-7}	136	10.2	1.1×10^{-7}	136	7.30
Ketene	2.8×10^{-7}	185	6.42	3.2×10^{-7}	185	6.42	4.6×10^{-7}	185	6.42
Methyl Amine	6.2×10^{-8}	101	5.04	1.1×10^{-8}	117	10.9	6.3×10^{-9}	216	7.80
Methyl Cyanide	5.2×10^{-7}	87.8	2.53	1.8×10^{-7}	87.8	2.53	2.5×10^{-8}	185	6.42
Methyl Cyanide Radical	1.8×10^{-11}	66.6	14.9	8.7×10^{-12}	51.4	11.7	5.0×10^{-12}	51.4	11.7
Isocyanic Acid	3.4×10^{-6}	87.8	2.53	2.2×10^{-6}	87.8	2.53	7.0×10^{-7}	87.8	17.7
Formamide	2.1×10^{-6}	58.4	12.6	1.0×10^{-6}	58.4	12.6	8.1×10^{-7}	58.4	12.6
Hydroxyl Amine	4.1×10^{-5}	185	6.42	4.8×10^{-5}	185	6.42	6.1×10^{-5}	185	6.42

Table 3.9: Peak fractional abundances of each molecule in the ice state and the locations at which they occur at 1 Myr, 2 Myr and 5 Myr

Table 3.9 gives the coordinates of the points (r,z) for the radius from the star and the height above the midplane respectively at which the fractional abundances, x/cm^{-3}, of the different species peak in the ice state at 1 Myr, 2 Myr and 5 Myr.

3.4   Discussion

When compared to their T Tauri counterparts, Herbig Ae/Be disks are thought to be poor in COMs due to their warmer midplane temperatures, higher levels of UV irradiation, smaller CO ice reservoir due to very little CO freezeout [Bosman et al., 2018] and less formaldehyde [Pegues et al., 2020]. The surprising detection of methanol in the HD 100546 disk, the bulk originating from the inner warmer disk, by Booth et al. [2021b] was the first evidence for warm rich complex organic chemistry due to thermal sublimation in a Class II disk in hot regions ($\gtrsim$100 K) or via non-thermal desorption triggered by, e.g., UV photons, in cooler regions (100 K)). As seen in the results, the abundance of methanol and most of the other COMs peak at 13 au, which is the location of the dust cavity of the HD 100546 disk [Grady et al., 2005]. The latter also aids the detection as both TW Hya and HD 163296 do not have large (greater than 5 au) inner cavities, thereby providing a possible explanation of the non-detections of an inner warm CH$_3$OH component by optically thick dust at millimeter wavelengths. Direct evidence for the high dust temperature at the cavity edge for the HD 100546 disk comes from the detection of crystalline silicates [Mulders et al., 2011].

In order to extract the chemical processes controlling the abundances of different species, we ran the chemical model at two points **A** and **B**, whose respective (r,z) coordinates in au are given by (13.1, 1.32) and (159, 12.4) at each timestamp of 1 Myr, 2 Myr, 5 Myr and 8 Myr. These are the points at which the fractional abundance of methanol peaks at 1 Myr in the gas and ice states respectively. Point A is near the midplane and in the inner disk and point B is in the outer disk and further up from the midplane. Table 3.10 summarises the main formation mechanisms of each species in both the ice gas and ice states at both points A and B at 1 Myr. It is seen therein that at Point B (the ice peak) which is further out and up in the disk, and at which the temperature is lower, 100% of almost all COMs form on the grain, starting with simple species such as H, OH and HCO, showing the effective formation of COMs on the grain in the outer disk and at low temperature, hence explaining their relatively high and constant abundances in the ice state at 100 au.

Molecule	Point A	Point B	Count
Methanol	$CH_3OH_2^+ + NH_3 \rightarrow CH_3OH + NH_4^+$	$GH + GCH_3O \rightarrow CH_3OH$	100%,100%
CH_3OH	$GOH + GCH_3 \rightarrow GCH_3OH$	$GH + GCH_3O \rightarrow GCH_3OH$	100%,100%
Formaldehyde	$NH_2CH_2O^+ - GRAIN \rightarrow H_2CO + NH$	$GO + GCH_2 \rightarrow H_2CO$	84%,93%
H_2CO	$GCH_3OH + CR_{Photon} \rightarrow GH_2CO + GH$	$GO + GCH_2 \rightarrow GH_2CO$	100%,93%
Methyl Methanoate	$H_5C_2O_2^+ - GRAIN \rightarrow HCOOCH_3 + H$	$GCH_3O + GHCO \rightarrow HCOOCH_3$	93%,100%
$HCOOCH_3$	$GCH_3O + GHCO \rightarrow GHCOOCH_3$	$GCH_3O + GHCO \rightarrow GHCOOCH_3$	100%,100%
Glycolaldehyde	$CH_2OHCH_2O^+ - GRAIN \rightarrow CH_2OHCHO + H$	$GH + GHOCHCHO\,or\,GOCH_2CHO \rightarrow CH_2OHCHO$	100%,40%
CH_2OHCHO	$GCH_2OH + GHCO \rightarrow GCH_2OHCHO$	$GH + GHOCHCHO\,or\,GOCH_2CHO \rightarrow GCH_2OHCHO$	100%,40%
Methyl Cyanide	$CH_3CNH^+ - GRAIN \rightarrow CH_3CN + H$	$GH + GCH_2CN \rightarrow CH_3CN$	100%,100%
CH_3CN	$GCH_3 + GCN \rightarrow GCH_3CN$	$GH + GCH_2CN \rightarrow GCH_3CN$	100%,100%
Methyl Cyanide Radical	$CO + CH_3CN^+ \rightarrow CH_2CN + HCO^+$	$GCH_2 + GCN \rightarrow CH_2CN$	82%,98%
CH_2CN	$GCH_3CN + CR_{Photon} \rightarrow GCH_2CN + GH$	$GCH_2 + GCN \rightarrow GCH_2CN$	100%,98%
Acetaldehyde	$CH_3CHCH_2 + OH \rightarrow CH_3CHO + CH_3$	$GCH_3 + GHCO \rightarrow CH_3CHO$	68%,95%
CH_3CHO	$GCH_3 + GHCO \rightarrow GCH_3CHO$	$GCH_3 + GHCO \rightarrow GCH_3CHO$	100%,95%
Ketene	$O + C_2H_4 \rightarrow CH_2CO + H_2$	$GH + GHC_2O \rightarrow CH_2CO$	89%,100%
CH_2CO	$GCH_3CHO + CR_{Photon} \rightarrow GCH_2CO + GH$	$GH + GHC_2O \rightarrow GCH_2CO$	100%,100%
Methanoic Acid	$CH_3COOH_2^+ - GRAIN \rightarrow CH_3COOH + H$	$GCH_3 + GCOOH \rightarrow CH_3COOH$	100%,98%
CH_3COOH	$GCH_3 + GCOOH \rightarrow GCH_3COOH$	$GCH_3 + GCOOH \rightarrow GCH_3COOH$	66%,98%
Methyl Amine	$CH_3NH_3^+ - GRAIN \rightarrow CH_3NH_2 + H$	$GH + GCH_3NH \rightarrow CH_3NH_2$	100%,100%
CH_3NH_2	$GNH_2 + GCH_3 \rightarrow GCH_3NH_2$	$GH + GCH_3NH \rightarrow GCH_3NH_2$	100%,100%
Dimethyl Ether	$CH_3OCH_4^+ - GRAIN \rightarrow CH_3OCH_3 + H$	$GCH_3 + GCH_3O \rightarrow CH_3OCH_3$	100%,100%
CH_3OCH_3	$GCH_3 + GCH_3O \rightarrow GCH_3OCH_3$	$GCH_3 + GCH_3O \rightarrow GCH_3OCH_3$	100%,100%
Isocyanic Acid	$H_2NCO^+ - GRAIN \rightarrow HNCO + H$	$GH + GOCN \rightarrow HNCO$	57%,100%
$HNCO$	$GH + GOCN \rightarrow GHNCO$	$GH + GOCN \rightarrow HNCO$	100%,96%
Formic Acid	$H_2O + HCOOH_2^+ \rightarrow HCOOH + H_3O^+$	$GOH + GCHCO \rightarrow HCOOH$	54%,100%
$HCOOH$	$GOH + GHCO \rightarrow GHCOOH$	$GOH + GHCO \rightarrow GHCOOH$	100%,100%
Formamide	$NH_2 + H_2CO \rightarrow NH_2CHO + H$	$GH + GHNCHO \rightarrow NH_2CHO$	91%,68%
NH_2CHO	$GNH_2 + GHCO \rightarrow GNH_2CHO$	$GH + GHNCHO \rightarrow GNH_2CHO$	100%,68%
Hydroxyl Amine	$GNH_2OH \rightarrow NH_2OH$	$GH + GHNOH \rightarrow NH_2OH$	100%,100%
NH_2OH	$GOH + GNH_2 \rightarrow GNH_2OH$	$GH + GHNOH \rightarrow GNH_2OH$	100%,100%

Table 3.10: Main formation mechanisms of all species in both the gas and grain (denoted by the prefix 'G' in the chemical formulae of the molecules) states at points A and B at 1 Myr

At Point A (the gas peak), which is the location of the dust cavity at 13 au, the abundance of most COMs are seen to peak, with abundances comparable to the observed methanol. However, from table 3.10, the formation mechanisms for most of the gas-phase COMs involve protonated complex species, e.g. $CH_3OH_2^+$ to form CH_3OH and CH_3CNH^+ to form CH_3CN, showing an inherited reservoir of COMs in the ice. This can also indicate that earlier in the evolution of the disk, there was a substantial cold (less than 20 K) reservoir in the outer disk which would allow for in-situ formation, as postulated by Booth et al. [2021b]. These ices would then sublimate, be protonated and participate in the reactions shown by the chemistry in table 3.10.

The modelled gas-phase abundances of almost all the other COMs being comparable

to that of the observed methanol, with the exception of the much larger 8-or-9-atom-bearing organics glycolaldehyde, methyl methanoate, dimethyl ether and methanoic acid, indicate a possible similar inheritance or earlier in-situ formation within the disk, followed by thermal processing. Apart from the detection of methanol in disks around the cold T-Tauri star TW Hya (with a low fractional abundance compared to what is typically detected around protostars) [Walsh et al., 2016] and the Herbig star IRS 48 [van der Marel et al., 2021], there has been the detection of dimethyl ether in the latter [Brunken et al., 2022]. Therefore, the detection in the gas-phase of the more complex COMs in HD 100546 will be representative of their total ice content in the system and will prove that disks can host a substantial chemically complex reservoir that is inherited from an earlier cold phase, also showing that complete chemical reprocessing of ice during disk formation may not occur. As a result, potential planets and moons forming from the material of these disks will be able to accrete icy, organic-rich material, showing that the building blocks of pre-biotic molecules are present during the formation of planets.

3.5 Summary and Conclusions

Some of the important findings in this chapter are:

- Substantial reservoirs (reaching as high as 10^{19} cm^{-2} in the gas state and 10^{20} cm^{-2} in the ice state) of COMs in both the gas and ice states are seen in disk with little depletion in most of them over the years.

- Larger organics, such as methanoic acid (CH$_3$COOH), dimethyl ether (CH$_3$OCH$_3$), glycolaldehyde (CH$_2$OHCHO) are among the least abundant in the gas state over the years, with the lowest maximum column density being that of glycolaldehyde at 3.8×10^{10} cm^{-2} at 117 au at 8 Myr.

- Ice-state COMs are seen in significant reservoirs in the outer disk, with the exception of the methyl cyanide radical (CH$_2$CN).

- The co-existence of the gas and ice states of the COMs is also seen, with the radial ice-to-gas ratio of the COMs reaching as high as 0.5 for formaldehyde (H$_2$CO), ketene (CH$_2$CO) and isocyanic acid (HNCO).

- As we progress over the years from 1 Myr to 8 Myr, a general decrease in the maximum column densities of all the gas-phase species is noted.

- Contrary to oxygen-bearing COMs, the peak column density of ice-state nitrogen-bearing COMs suffer significant decreases by three orders of magnitude, the maximum decrease being of methyl cyanide.

- For all the species, the maximum fractional abundance of their gas state generally decrease as we progress from 1 Myr to 5 Myr as opposed to little to no variation in that of the ice state.

- The most abundant molecule in the gas state at all three timestamps is the N- and O-bearing organic molecule formamide which peaks at 4.7×10^{-7} cm^{-3} at 1 Myr to 2.3×10^{-7} cm^{-3} at 5 Myr, at the constant location of (185, 6.42) in (r,z) coordinates.

- The most abundant molecule in the ice-state at all three timestamps is the inorganic molecule hydroxyl amine which peaks at $\sim 10^{-5}$ cm^{-3} at (185, 6.42) in (r,z) coordinates.

- The modelled gas-phase abundances of almost all the other COMs being comparable to that of the observed methanol indicate a possible similar inheritance or earlier in-situ formation, followed by thermal processing.

In this section of the project, it is seen from the chemical model of the HD 100546 protoplanetary disk that the 15 chosen COMs, with the exception of the much larger 8-or-9-atom-bearing organics glycolaldehyde, methyl methanoate, dimethyl ether and methanoic acid, have abundances comparable to the observed methanol in the gas phase, especially at the location of the dust cavity at 13 au. If detected, they will further strengthen the hypothesis of the inheritance of COMs-rich ices from an earlier cold phase and will also confirm the availability of biologically important molecules at the epoch of planet formation.

CHAPTER 4

Line Survey of Complex Organic Molecules in the HD 100546 Protoplanetary Disk

4.1   Introduction

Since the discovery of the first molecules CH$^+$ [Douglas and Herzberg, 1941] and OH [Weinreb et al., 1963] in space, line emission has been an important probe of the physics and chemistry of their residing environment, making the spectra and chemistry of molecules useful astrophysical and astrochemical tracers. As seen in Chapter 2, the models computing the molecular abundances from the rates of their formation and destruction provide information about both the current physical conditions and the histories of the sources. On the other hand, molecular spectra reveal detailed physical information of the gas and dust, and characterise the species. The density and temperature of the gas can be inferred from the high-resolution rotational and vibrational absorption spectra which also tell us about large-scale motions such as collapse and rotation. Information on the polar or non-polar nature of the mantles surrounding the particles can be obtained from the vibrational spectra of the molecules.

In this section, a disk line survey is run, whereby a treatment of radiative transfer with the molecular abundances from the chemical model described in Chapter 2 and a parametric model run as described in this chapter is carried out, predicting the intensity and shape of the different spectral transitions of the species considered. An overview of rotational spectroscopy and radiative transfer, with insights into observations with the Atacama Large Millimetre/Submillimetre Array (ALMA) and the Square Kilometre Array (SKA) is provided in the first section of this chapter. ALMA is a transformative radio telescope, making observations at millimeter and submillimeter wavelengths. Located in the dry climate and extreme elevation (5000 m) of the site in the Atacama Desert in Chile, ALMA uses 66 high-precision dish antennas of two sizes: 54 of them are 12 meters across and 12 of them are 7 meters across. The total collecting area of this array is over 71,000 square feet. SKA is the world's largest radio telescope, with eventually over a square kilometre (one million square metres) of collecting area. It consists of two radio telescopes that will complement each other scientifically: SKA-Mid and SKA-Low, allowing observations at cm and metre wavelengths. The first phase of SKA will consist of: SKA1-Low which will have 512 stations of 256 log periodic dipole antennas each operating between 50 and 350 MHz, and SKA1-Mid, which will have a total of 197 antennas (including the 64 antennas of the MeerKAT array) operating between 350 MHz and 15 GHz [Braun et al., 2019].

The Methodology section is followed by the plots of the integrated intensities and

line profiles of the different species from both the chemical and the parametric models in the ALMA and SKA regimes in the Results section. These plots are then discussed in the subsequent section. A brief conclusion is provided at the end of this chapter.

4.2 Methodology

In this section, rotational spectroscopy and radiative transfer are explained in order to understand the disk line survey done, with brief insights into the parametric modelling done in order to reproduce the observed fluxes.

4.2.1 Rotational Spectroscopy and Molecular Data

Rotational spectroscopy plays a crucial role in the investigation of protoplanetary disks and the interstellar medium (ISM). Most of the detected gaseous interstellar and circumstellar molecules, and virtually all of the complex species are observed via their rotational spectral lines. Incident electromagnetic waves can excite the rotational levels of molecules provided they have an electric dipole moment and the electromagnetic field exerts a torque on the molecule as seen in Figure 4.1.
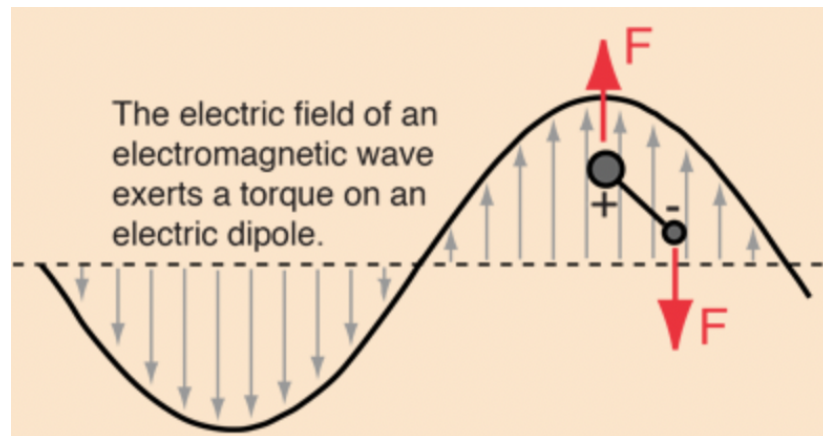
Figure 4.1: Torque exerted by the electromagnetic field on a molecule with an electric dipole moment

The spectra for rotational transitions of molecules are typically in the submillimetre region of the electromagnetic spectrum. Each electronic state of a molecule has several vibrational states associated with it and most commonly, rotational transitions which

are associated with the ground vibrational state are observed as seen in Figure 4.2. The rotational spectra of molecules have been studied by microwave spectroscopists in the laboratory from as early as the late 1930s [Townes and Schawlow, 1955]. Although ab initio quantum chemical calculations have been improving, they are still not capable of experimental accuracy, which is $\sim 1 - 10$ kHz or even better with selected methods [Herbst and van Dishoeck, 2009].
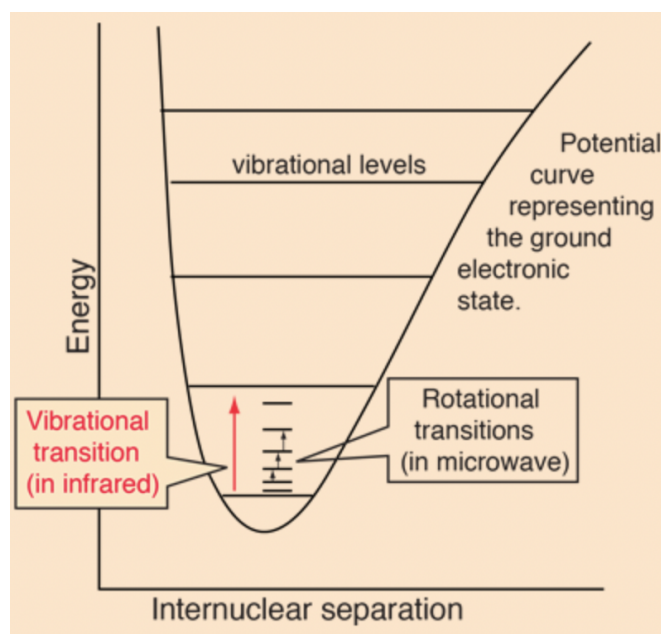
Figure 4.2: A portion of the potential energy diagram for a stable electronic state of a diatomic molecule

Considering the classical energy, E of a freely-rotating molecule, the rotational kinetic energy of the latter can be expressed in terms of the angular momenta and moments of inertia about the principal axes, a, b and c (L_a and I_a respectively about the a-axis):

$$E = \frac{L_a^2}{2I_a} + \frac{L_b^2}{2I_b} + \frac{L_c^2}{2I_c} \qquad (4.1)$$

Effective Hamiltonian operators are typically used by rotational spectroscopists to interpret their spectra. The effective Hamiltonian describes a quasi-rigid-body rotational motion in the presence of vibrational motions of higher frequency and is developed along the principal axes for tops (nonlinear molecules). It is normally written

as an expansion in terms of products of angular momentum operators raised to even powers that multiply spectroscopic constants (parameters). The Hamiltonian operator is expressed in terms of the angular momentum operator as:

$$H\Psi = \frac{L^2}{2I}\Psi = \frac{J(J+1)\hbar^2}{2I}\Psi \tag{4.2}$$

where J is the quantum number for total rotational angular momentum, such that the energy levels of all molecules can be written in terms of these spectroscopic constants, which consist of one or more rotational constants, $A \geq B \geq C$. The latter are the inverses of the moments of inertia as they are given by the ratio $\frac{\hbar^2}{2I}$ ($I_A \geq I_B \geq I_C$) in appropriate (frequency or wavenumber) units, and the centrifugal distortion constants. There are three types of non-linear rotors: spherical tops which possess three equal moments of inertia along the principal axes; symmetric tops, which possess two equal moments; asymmetric tops, in which all three moments of inertia are different. Purely rigid molecules have only second-order terms in angular momenta (a total exponent of 2) and the treatment of nonrigidity involves the centrifugal distortion terms, starting from fourth-order terms (a total exponent of 4). The identification of molecules is often aided by the presence of multiplets which are sub-levels into which rotational energy levels split in the presence of interactions involving unpaired electronic spin and orbital angular momentum (fine structure) and nuclear spin angular momentum (hyperfine structure).

Spectral line frequencies are derived from the energy differences between pairs of levels connected by non-zero dipolar transition moments. The intensities of these lines can be obtained from the dipolar matrix elements. The direction of the dipole moment components determine the selection rules: a-, b-, and c-type transitions pertain to dipole components along the a, b, c principal axes. Larger molecules have larger moments of inertia and smaller rotational constants, and hence denser spectra. Rotational and centrifugal distortion constants can be used to predict the frequencies of other lines measured in the laboratory and subsequently, improved constants, which can eventually be used to predict lines not studied in the laboratory. Transitions involving larger rotational quantum numbers generally occur at higher frequencies. It is therefore often difficult to predict higher frequency lines accurately in the laboratory due to limitations on the frequencies that we can go to. The rotational spectrum can be complicated by an additional large-amplitude motion which is possessed by some of the more satur-

ated complex molecules such as methanol. Called torsion (or internal rotation), this motion leads to transitions (and hence lines in the spectra) between thermally populated excited torsional levels; sublevels due to the splitting of the torsional levels; and the torsional and quasi-rigid rotational levels. It also results in the existence of conformers (such as trans and gauche) which are structures having the potential minima corresponding to torsional motion at different energies. Consequently, the presence of torsional motion has the effect of increasing the density of spectral lines of internal rotors, such as methanol, methyl methanoate, dimethyl ether. For COMs, the spectra can already be quite dense at 100-300 K in the millimeter-wave and submillimeter-wave regions without torsional motion [Herbst and van Dishoeck, 2009].

A definite detection is characterised by certain rules which are: rest frequencies are known from either laboratory measurements or a high-precision Hamiltonian model to an accuracy of 1:107; there is an agreement between the observed and rest frequencies, at roughly their predicted relative intensities, of clean, non-blended lines for a single well-determined velocity of the source; the observed spectrum of a molecule contains all the lines predicted from an LTE spectrum at a well-defined rotational temperature and appropriately corrected for beam dilution; consistency is ensured and contaminating blended features are eliminated by simulating the entire spectrum of a source using all identified molecules; and all lines of the new molecule are shown to come from the same location through interferometric images (Belloche et al. [2008] and Ziurys and Apponi [2005]). As such, facilities such as ALMA and SKA are vital in the detection of new molecules, especially COMs. Since a single anti-coincidence (a missing predicted line in the observational data) as criterion for rejection takes precedence over numerous coincidences for identification, it is very useful to simulate complete line surveys of molecules of interest in order to facilitate and ensure such detections. In this section, line surveys of the chosen 15 molecules in the HD 100546 protoplanetary disk are carried out to generate their entire spectra over the full frequency ranges of ALMA and SKA. These spectra can be used as a background against observed lines to confirm potential detections. The strongest lines for each molecule in each frequency regime are also tabulated.

Laboratory work and simulations altogether strive to populate spectral databases for rotational transitions, which facilitate the assignment of interstellar molecular lines. With useful computer interfaces enabling the downloads of single-molecule or composite

spectra in different frequency ranges, they contain the quantal assignments, frequencies, and intensities of both measured and predicted rotational lines for many species. Examples of such databases are: the JPL Catalog [Pickett et al., 1998], the Cologne Database for Molecular Spectroscopy [Müller et al., 2005], the Lovas/NIST database of recommended rest frequencies for known astronomical transitions (http://physics.nist.gov/PhysRefData the Leiden Atomic and Molecular Database (LAMDA) [Schöier et al., 2005] which collects spectroscopic information and collisional rate coefficients for molecules, atoms, and ions of astrophysical and astrochemical interest. In this work, the molecular data from the LAMDA is used. It is however to note that spectral databases tend to be incomplete and somewhat biased towards existing interstellar species.

4.2.2 Radiative Transfer

Radiative transfer is the physical phenomenon of energy transfer in the form of electromagnetic radiation. The propagation of radiation through a medium is affected by absorption, emission, and scattering processes, which can be described mathematically by the equation of radiative transfer. Simply put, the latter depicts that as a beam of radiation travels, it loses energy to absorption, gains energy by emission processes, and redistributes energy by scattering. The prediction of the radiation signature associated with a physical model, which can be done by solving the equation of radiative transport, is of paramount significance in the interpretation of astronomical observations. In the sub-millimetre regime, the scattering term is of little significance [Brinch and Hogerheijde, 2010], leading to the spectral intensity, I_ν of radiation propagating through a medium to be given in terms of the emission (j_ν) and absorption (α_ν) coefficients of the latter, given by

$$\frac{dI_\nu}{ds} = j_\nu - \alpha_\nu I_\nu \tag{4.3}$$

For transitions of energy of $h\nu$, between any two adjacent energy levels of energies E_1 and E_2 ($h\nu$ being the difference between E_1 and E_2), the emission and absorption coefficients, j_ν) and α_ν, are related to the Einstein coefficients A_{12}, B_{12} and B_{21}, for the line emission through:

$$j_{\nu;gas} = \frac{h\nu}{4\pi} n_2 A_{12} \phi(\nu) \tag{4.4}$$

63

$$\alpha_{\nu;gas} = \frac{h\nu}{4\pi}(n_1 B_{12} - n_2 B_{21})\phi(\nu) \tag{4.5}$$

where $\phi(\nu)$, a function of frequency, contains the contribution of several line broadening mechanisms (the most dominant of which is Doppler broadening - Teague and Loomis [2020]), and for the thermal dust emission, through:

$$j_{\nu;dust} = -\alpha_{\nu;dust}B_\nu(T_{dust}) \tag{4.6}$$

$$\alpha_{\nu;dust} = \kappa_\nu \rho_{dust} \tag{4.7}$$

where B_ν is the Planck function for a given dust temperature, κ is the dust opacity and ρ_{dust} is the dust mass density.

Equation 4.3 can be solved for I_ν, which can then be integrated over all solid angles to obtain the local mean radiation field at any given position:

$$J_\nu = \frac{1}{4\pi}\int I_\nu d\Omega \tag{4.8}$$

High computational capabilities are required to solve the equation of radiative transfer, which can be accomplished only by numerical analysis, except for the simplified and limiting cases of little interaction between matter and radiation in local thermodynamic equilibrium (LTE) or the optically thin regime. The simplest way to estimate a molecular column density from an observed line intensity is actually two-fold: estimate the molecular column density in the initial state of the observed line (upper state for emission lines, lower state for absorption lines); and account for the other, unobserved states of the molecule by assuming that a Boltzmann distribution population of the energy levels, whereby the characteristic 'excitation temperature' (T_{ex}) is often taken to be equal to T_{kin}, which is the case of LTE (applies at high densities when collisions determine the excitation) [van der Tak, 2011]. Altogether, these two steps consequently avoid radiative transfer. Numerical algorithms such as those by Bernes [1979], Juvela [1997], Hogerheijde and van der Tak [2000], Pavlyuchenkov and Shustov [2004] and Brinch and Hogerheijde [2010] (used in the fourth chapter of this work) are available in the community for the prediction of molecular line emission in the non-LTE regime. In most of such codes, the source model is mapped onto a regular grid of cells, over each of which, model properties (such as density, temperature, molecular abundance,

radiation field J_ν, level populations n_i) are taken to be constant. The mean radiation field J_ν for a cell can then be obtained by summing over all photons, which are each traced in random directions from random points of absorption within a cell, followed by an integration of equation 4.3 along the paths. Radiative transfer calculations have many limitations, some of which are disagreement between observations at different wavelengths, presence of unresolved substructure in the data, observations covering only part of the source and a few molecular levels, limited availability of molecular data [van der Tak, 2011].

In this chapter, the code by Walsh et al. [2014b] is used to calculate the molecular line emission for the chosen 15 molecules in the HD 100546 disk. Comparison of the model results with current observations will allow the selection of potential molecules and line transitions which may be observable with either ALMA or SKA in the HD 100546 disk. The rotational line transition intensities for molecules considered in this work are calculated based on two assumptions made in the computations: the disk is face-on (it has an inclination of $0°$ - this allows the quick and efficient calculation of line emission without considering geometrical effects due to disk inclination) and local thermodynamic equilibrium (LTE) holds throughout, making the computation of an entire spectrum of a particular molecule possible in a single calculation. Despite its numerous caveats (such as the possibility of strong masing lines by the radiative pumping of particular transitions by the intense thermal background radiation in warm regions of the disk), the latter assumption is particularly important for COMs which, bearing many energy levels, have relatively complex spectra [Walsh et al., 2014b]. Also, disk conditions are expected to deviate from LTE mainly in the outer, colder more diffuse regions of the disk and LTE disk-integrated line intensities are expected to differ from those calculated assuming non-LTE conditions by a factor of a few only [Pavlyuchenkov et al., 2007]. Despite these assumptions, the line intensities calculated in this exploratory work are useful in determining which transitions in which molecules may be detectable with ALMA and SKA. Fractional abundances from the chemical model analysed in Chapter 3 at 1 Myr are used as input when running the disk line survey code in this chapter. This timestamp of 1 Myr is chosen as it is an optimistic value at which most abundances peak.

The population of an energy level i (in terms of the number density, n_i in level i) is given by the Boltzmann distribution as LTE is assumed throughout and is given, in

terms of the degeneracy of the level, g_i, the energy in units of K of the level, E_i, the gas temperature, T and the total partition function, $Z(T)$, by

$$\frac{n_i}{n} = \frac{g_i \exp\left\{\frac{-E_i}{T}\right\}}{Z(T)} \tag{4.9}$$

where n is the total number density of the molecule, given by

$$n = \Sigma_i n_i \tag{4.10}$$

Since COMs can be vibrationally excited at relatively moderate temperatures ($\approx$300 K) [Walsh et al., 2014b], in the inner regions of the disk, the gas temperature is high enough to allow for the vibrational excitation. Hence, the vibrational partition function is also included in the determination of the total partition function, $Z(T)$, given by the product of the rotational and vibrational partition functions:

$$Z(T) = Z_{vib}(T) \times Z_{rot}(T) \tag{4.11}$$

where the rotational partition function, $Z_{rot}(T)$ is explicitly calculated by summing over populated energy levels in colder regions:

$$Z_{rot}(T) = \Sigma_i g_i \exp\left\{\frac{-E_i}{T}\right\} \tag{4.12}$$

and using the high temperature approximation once the higher energy levels become sufficiently populated:

$$Z_{rot}(T) \approx \frac{\sqrt{\pi}(kT)^{\frac{3}{2}}}{\sigma\sqrt{ABC}} \tag{4.13}$$

where k is the Boltzmann's constant, σ is the number of indistinguishable rotational orientations of the molecule (the symmetry factor) and A, B and C are the rotational constants in energy units.

The vibrational partition function, $Z_{vib}(T)$ is given by

$$Z_{vib}(T) = \prod_i \frac{1}{1 - \exp\left\{\frac{-h\nu_i}{kT}\right\}} \tag{4.14}$$

The disk-integrated line flux density, F_ν, is determined by integrating the solution of the radiative transfer equation vertically and radially.

$$F_\nu = \frac{1}{4\pi D^2} \int_{r_{min}}^{r_{max}} \int_{-z_{max}(r)}^{+z_{max}(r)} 2\pi r \overline{\eta}(r, z) \, dz \, dr \tag{4.15}$$

where D is the distance to the source (a distance of 103 pc to the source HD 100546 is used), and $\overline{\eta}(r, z)$ is the product of the emissivity at grid point (r, z) and the absorption in the upper disk and is given by:

$$\overline{\eta}(r, z) = n_u(r, z) A_{ul} \phi_\nu \frac{h\nu}{4\pi} e^{-\tau_\nu(r,z)} \tag{4.16}$$

where n_u is the abundance in the upper energy level of the transition, A_{ul} is the Einstein coefficient for spontaneous emission from the upper energy level u to the lower energy level, l, ϕ_ν is the value of the line profile function (assumed to be Gaussian) at the frequency ν, h is the Plank's constant and $\tau_\nu(r, z)$ is the optical depth, where

$$\tau_\nu(r, z) = \int_z^{z_{max}} \chi_\nu(r, z') \, dz' \tag{4.17}$$

where χ_ν is the absorption coefficient and is a function of ρ, the dust mass density in g cm^{-3} and the dust mass absorption coefficient, κ_ν in cm^2 g^{-1}, and is given by

$$\chi_\nu = \rho\kappa_\nu + (n_l B_{lu} - n_u B_{ul})\phi_\nu \frac{h\nu}{4\pi} \tag{4.18}$$

where n_l is the abundance in the lower energy level in the transition, and B_{lu} and B_{ul} are the Einstein coefficients for absorption and stimulated emission respectively.

4.2.3 Parametric Modelling of the Ray Tracing of the Emission from COMs in the HD 100546 Disk

After carrying out the disk line survey using the chemically modelled abundances of the species, parametric models were run to reproduce the observed fluxes of formaldehyde and methanol at 1 Myr from Booth et al. [2021b]. The parametric modelling revolved around generating fractional abundance files for each molecule which were fed to the disk line survey code as input, mainly for formaldehyde and methanol. The principal factor governing the location of the COMs in this parametric modelling was temperature. We started by placing the maximum chemically modelled abundances (from the chemical model analysed in chapter 3) of formaldehyde and methanol - which is of the order of 10^{-7} - within the temperature range of 20 K to 50 K. A linear relationship was assumed between the abundance of the species and the flux predicted by the code,

such that the next parametric model would be informed by scaling the abundance in the previous model by the same ratio of the desired flux to the obtained flux, while respecting the same temperature boundaries of 20 K and 50 K. Once the final abundance input file which reproduced the desired flux for methanol was obtained, the line survey was run for all the other COMs by assuming that they have the same abundance and are located in the same region as methanol.

4.3 Results

In this section, the results of the parametric modelling are documented. The plots of the integrated line intensities and the disk-integrated line spectra over the whole frequency ranges of ALMA (50-950GHz) and SKA (0-30GHz) are also provided for surveys ran with abundances from both the chemical and parametric models. The integrated intensities are obtained by integrating the emission at a given frequency over a velocity and the disk. The line spectra generates line profiles, showing the maximum emission at a given frequency from the whole disk. The strongest line, and therefore deemed the most qualified for observations, for each molecule is tabulated alongside the corresponding transition for both the ALMA and SKA regimes.

4.3.1 Parametric Models

For formaldehyde, the 11th model reproduced the strongest observed flux (corresponding to the transition $4_{2,2} - 3_{2,1}$ of p-H_2CO - shown as transition 161 in Figure 4.3), within 10%, with a fractional abundance of 2.8×10^{-10}, which is three orders of magnitude smaller than the maximum fractional abundance of gas-phase formaldehyde at 1 Myr from the chemical model. The observed flux of the other p-H_2CO-line (corresponding to the transition $4_{2,3} - 3_{2,2}$ - transition 158 in Figure 4.3) - was reproduced within 10% in parametric model 5, with a fractional abundance of 2.0×10^{-10}. Lines from transitions in o-H_2CO (transitions 159 and 160 in Figure 4.3) were observed to be partially blended and were therefore not used as a guide in the parametric modelling.

For methanol, the 5th model reproduced the strongest observed flux (corresponding to the transition $6_{1,5,1} - 5_{1,4,1}$ of E-CH_3OH - shown as transition 996 in Figure 4.3) - within 10%, with a fractional abundance of 3.3×10^{-10}, which is also three orders of magnitude less than the maximum fractional abundance of gas-phase methanol at 1

Myr from the chemical model. The lack of agreement by several orders of magnitudes between the chemically modelled and parametrically modelled abundances can be explained by the fact that the chemical and/or physical model of the disk lack certain ingredients. The line from transition $6_{2,4,0} - 5_{2,3,0}$ (transition 997 in Figure 4.3) of A-CH$_3$OH had an observed upper limit and the line from transitions $6_{2,5,1} - 5_{2,4,1}$ and $6_{2,4,0} - 5_{2,3,0}$ of E-CH$_3$OH are blended the sum of their fluxes are reported as transition 998 (except for parametric models 4 and 5, for which the intensities are shown separately as transitions 998 and 999) in Figure 4.3.
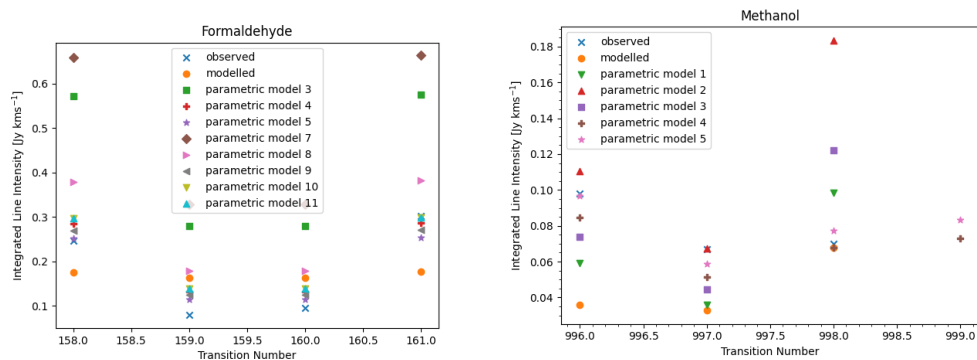
Figure 4.3: Formaldehyde (left) and methanol (right) parametric modelling

4.3.2 Line Survey of Complex Organic Molecules in the HD 100546 Disk with ALMA

In this subsection, the integrated line intensities and disk-integrated line spectra of the chosen COMs predicted in the line survey using both the chemical and parametric models in the ALMA frequency range of 50-950 GHz are reported in two parts. In the parametric models, the reservoir of the COMs is constrained within 20-50 K at a fixed fractional abundance of 3.3×10^{-10}. Comparisons between the predictions made from each model are also provided in terms of the highest-integrated intensity and the maximum-flux lines.

Integrated Intensities of the Molecular Emission of Complex Organic Molecules in the HD 100546 Disk from the Chemical Model and the Parametric Model in the ALMA Frequency Range

Figures 4.4 and 4.5 show the plots of the integrated intensities (the plots of the following are included: methanoic acid - no molecular data available; acetaldehyde - integrated intensities not successfully plotted; glycolaldehyde, dimethyl ether and methyl methanoate - integrated intensities not generated) from the line survey using the abundances from the chemical model over the whole frequency range of ALMA.

Figure 4.4: Integrated intensities of the molecular emission of COMs simulated with abundances from the chemical model at 1Myr over the whole frequency coverage of ALMA
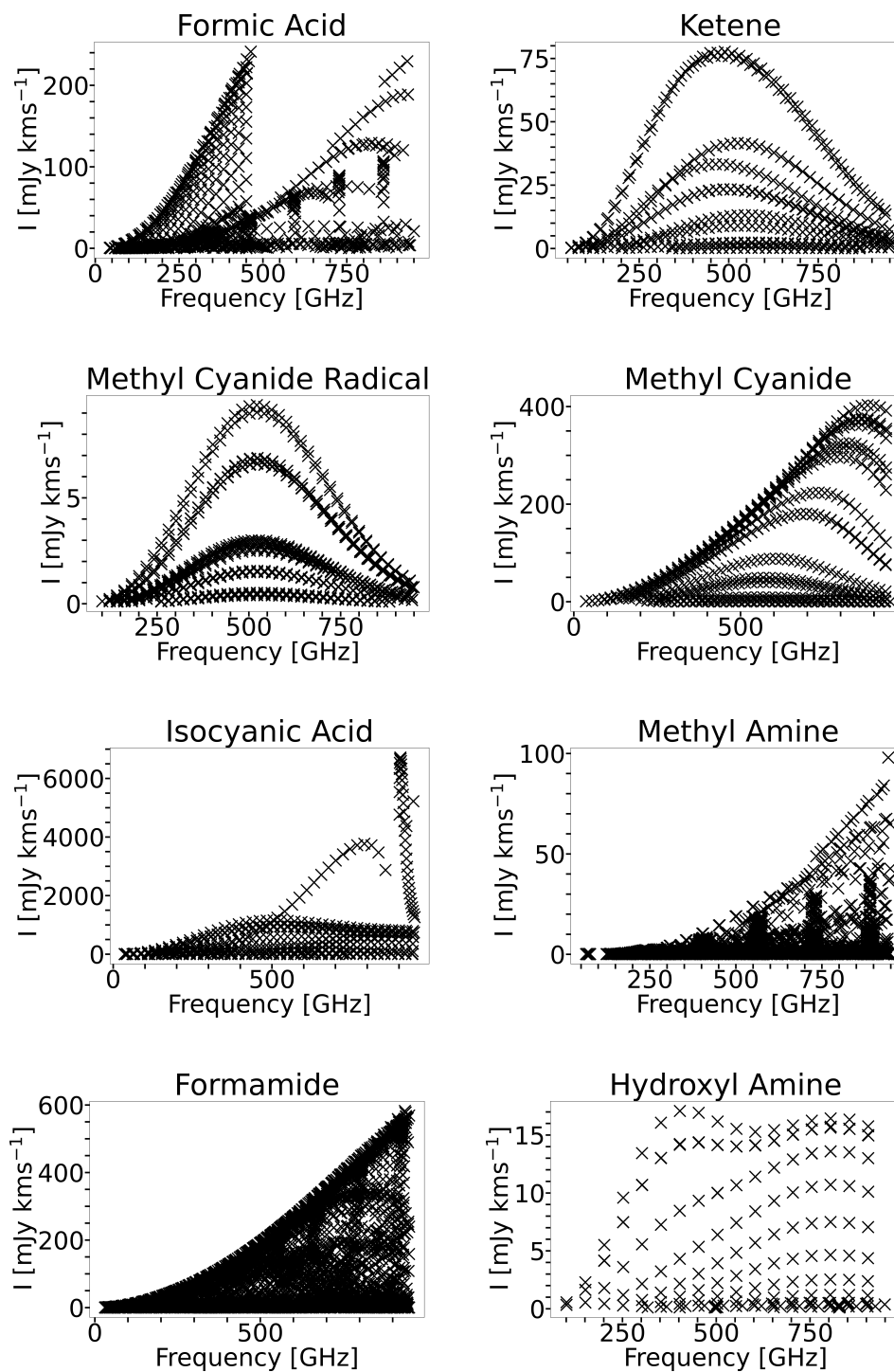
Figure 4.5: Integrated intensities of the molecular emission of COMs simulated with abundances from the chemical model at 1Myr over the whole frequency coverage of ALMA - *continued*

When the disk line survey is run with abundances from the chemical model, it is seen that significant ranges of integrated intensities are predicted for the different species over the whole frequency range, with the most densely populated plots beings those of acetaldehyde and formamide. The maximum integrated intensity predicted is that of isocyanic acid at 6.7 Jy kms^{-1} at a frequency of 905 GHz, followed by formaldehyde at 4.2 Jy kms^{-1} at a frequency of 897 GHz. The integrated intensity is seen to peak at the higher end (850 GHz - 950 GHz) of the ALMA frequency range for most molecules, with the exception of acetaldehyde, formic acid, methyl cyanide radical and hydroxyl amine. The maximum integrated intensities range all the way down to 17 mJy kms^{-1} and 9 mJy kms^{-1} for hydroxyl amine and methyl cyanide radical respectively, making the latter the molecule with the minimum peak integrated intensity at 522 GHz predicted in the survey when run with abundances from the chemical model.

Figures 4.6, 4.7 and 4.8 show the plots of the integrated intensities (the plot of methanoic acid is not included as the molecular data file for it was not available) from the line survey using the abundances from the parametric model over the whole frequency range with ALMA. In these models, the reservoir of the COMs is constrained within 20-50 K at a fixed fractional abundance of 3.3×10^{-10}.
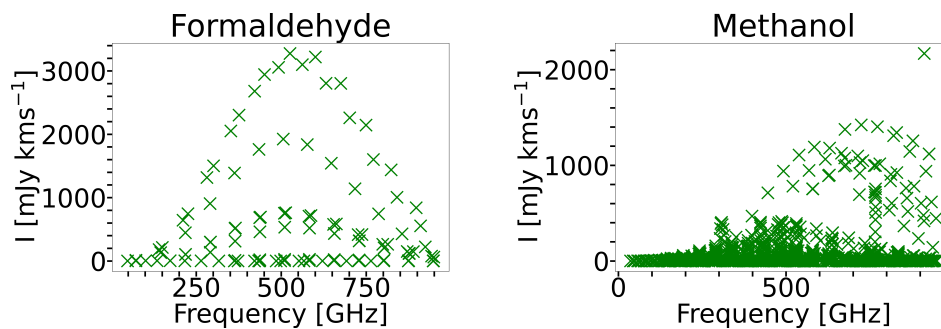
Figure 4.6: Integrated intensities of the molecular emission of COMs simulated with abundances from the parametric model over the whole frequency coverage of ALMA
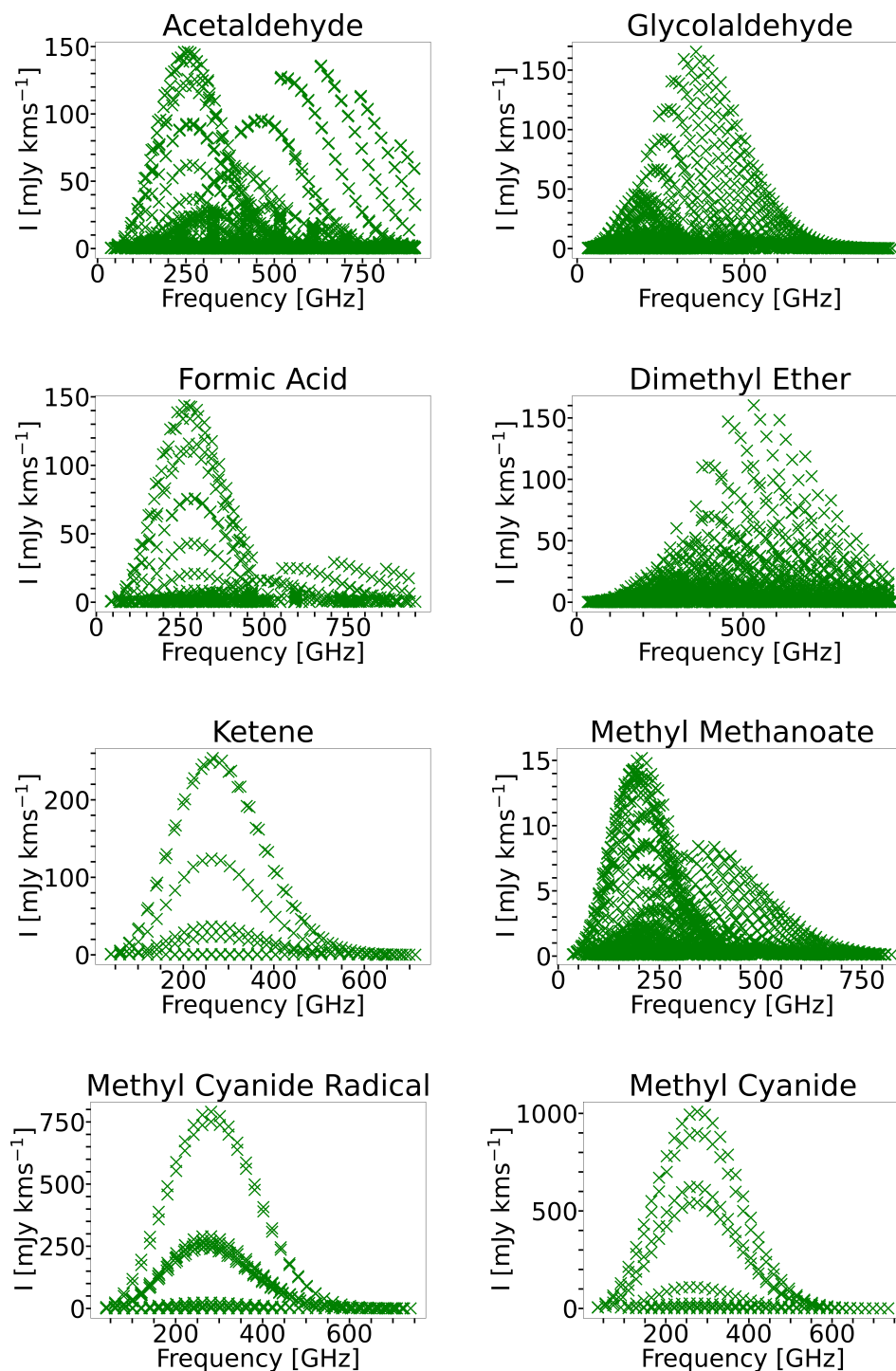
Figure 4.7: Integrated intensities of the molecular emission of COMs simulated with abundances from the parametric model over the whole frequency coverage of ALMA - *continued*
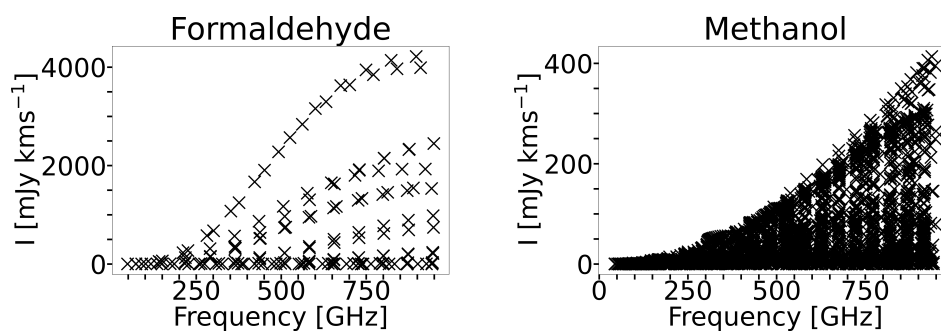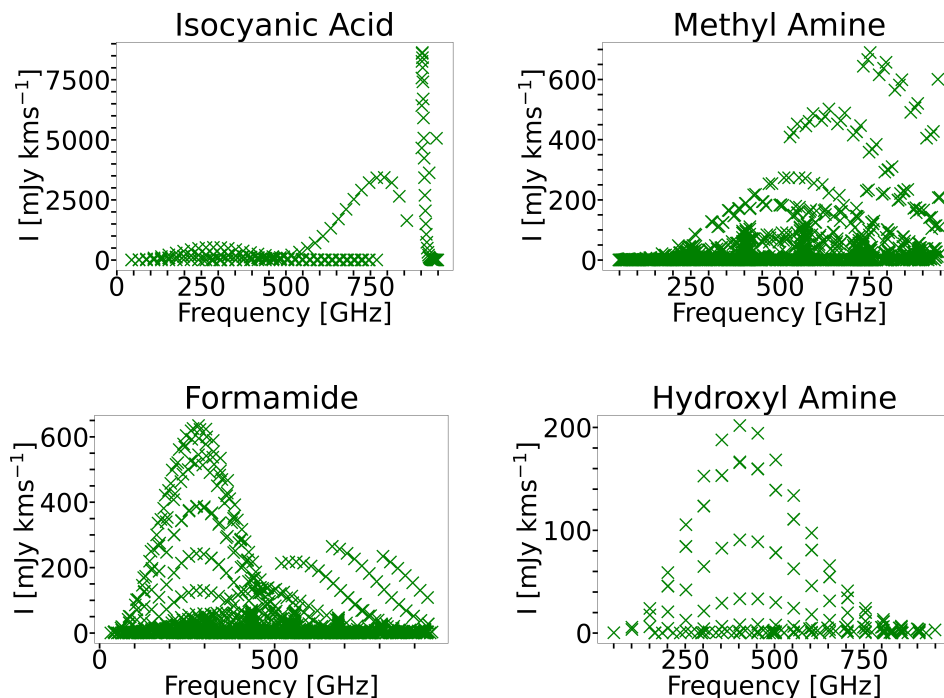
Figure 4.8: Integrated intensities of the molecular emission of COMs simulated with abundances from the parametric model over the whole frequency coverage of ALMA - *continued*

When the disk line survey is run with abundances from the parametric model, it is seen that significant ranges of integrated intensities are predicted for the different species over the whole frequency range, with the most densely populated plots beings those of the larger COMs glycolaldehyde, dimethyl ether and methyl methanoate. The maximum integrated intensity predicted is again that of isocyanic acid, but at a higher magnitude of 8.6 Jy kms^{-1} at about the same frequency of 903 GHz, followed again by formaldehyde at a lower magnitude of 3.3 Jy kms^{-1}, occurring at a lower frequency of 526 GHz. The integrated intensity is seen to generally peak in the relatively lower, but over a larger range (200 GHz - 550 GHz) of the ALMA frequency range for most molecules, with the exception of methanol and methyl amine. The maximum integrated intensities range all the way down to 15 mJy kms^{-1} for methyl methanoate, making the latter the molecule with the minimum peak integrated intensity at also the lowest frequency of 207 GHz at which the integrated intensities of the molecules are predicted

to peak in the survey when run with abundances from the parametric model.

Table 4.1 shows the frequencies at which the integrated intensity is maximum from the chemical model and the parametric model in the ALMA frequency range.

Molecule	Chemical Model		Parametric Model	
	Frequency/GHz	Integrated Intensity/mJy km s^{-1}	Frequency/GHz	Integrated Intensity/mJy km s^{-1}
Formaldehyde	896.805	4216	525.666	3275
Methanol	937.478	414	912.109	2168
Acetaldehyde	529.391	35	255.385	146
Glycolaldehyde	-	-	356.137	165
Formic acid	463.588	241	262.104	144
Methanoic acid	*No molecular data available*			
Dimethyl ether	-	-	532.325	160
Ketene	489.105	78	265.095	254
Methyl methanoate	-	-	206.619	15
Methyl cyanide radical	521.834	9	281.500	791
Methyl cyanide	881.260	403	275.916	1008
Isocyanic acid	904.547	6713	903.369	8633
Methyl amine	942.618	98	752.906	690
Formamide	936.881	582	282.569	634
Hydroxyl amine	402.847	17	402.847	202

Table 4.1: Comparison of the lines with the maximum integrated intensity predicted by the line survey using abundances from the chemical model and the parametric model in the ALMA regime

As seen from Table 4.1, when the disk line survey is run with abundances from the parametric model, the integrated intensities peak at lower frequencies, with the exception of isocyanic acid and hydroxyl amine, for which the predicted maximum intensities occur at the about the same frequencies of 904 GHz and 403 GHz respectively. The values of the peak integrated intensities are predicted to be generally higher for all the molecules (with the exception of formaldehyde and formic acid) with the parametric model, with ratios of the predicted maximum integrated intensity with the parametric model to that with the chemical model being as high as 88 for methyl cyanide radical and reaching values of 1.1 for formamide, for which the difference is relatively smaller. When the reservoir of the COMs is constrained within 20-50 K at a fixed fractional abundance of 3.3×10^{-10}, relatively stronger integrated intensities at generally lower frequencies are therefore predicted than when the abundances are taken from the chemical model.

Disk-Integrated Line Spectra of Complex Organic Molecules in the HD 100546 Disk from the Chemical Model and the Parametric Model in the ALMA Frequency Range

Figures 4.9 and 4.10 provide the disk-integrated line spectra of the chosen COMs from the line survey using the abundances from the chemical model over the whole frequency range with ALMA.
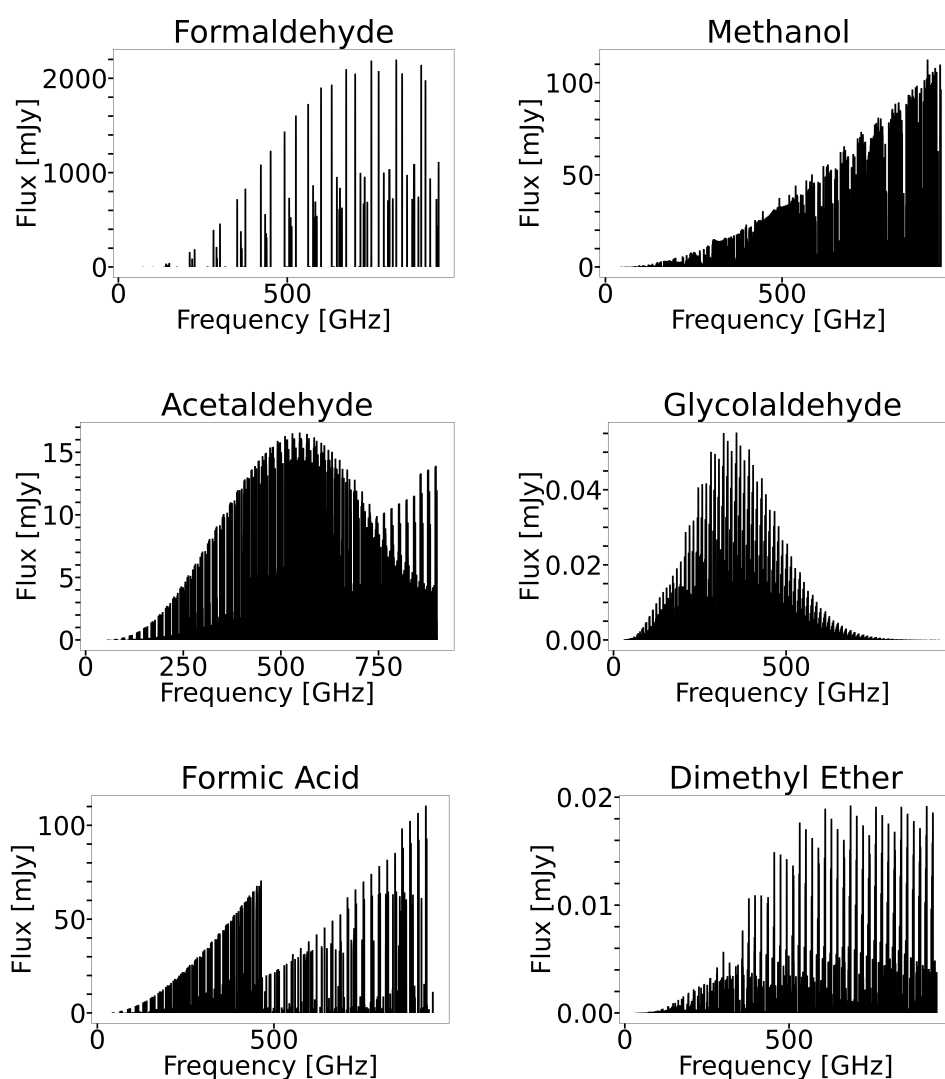

Figure 4.9: Disk-integrated line spectra of COMs simulated with abundances from the chemical model at 1Myr over the whole frequency coverage of ALMA
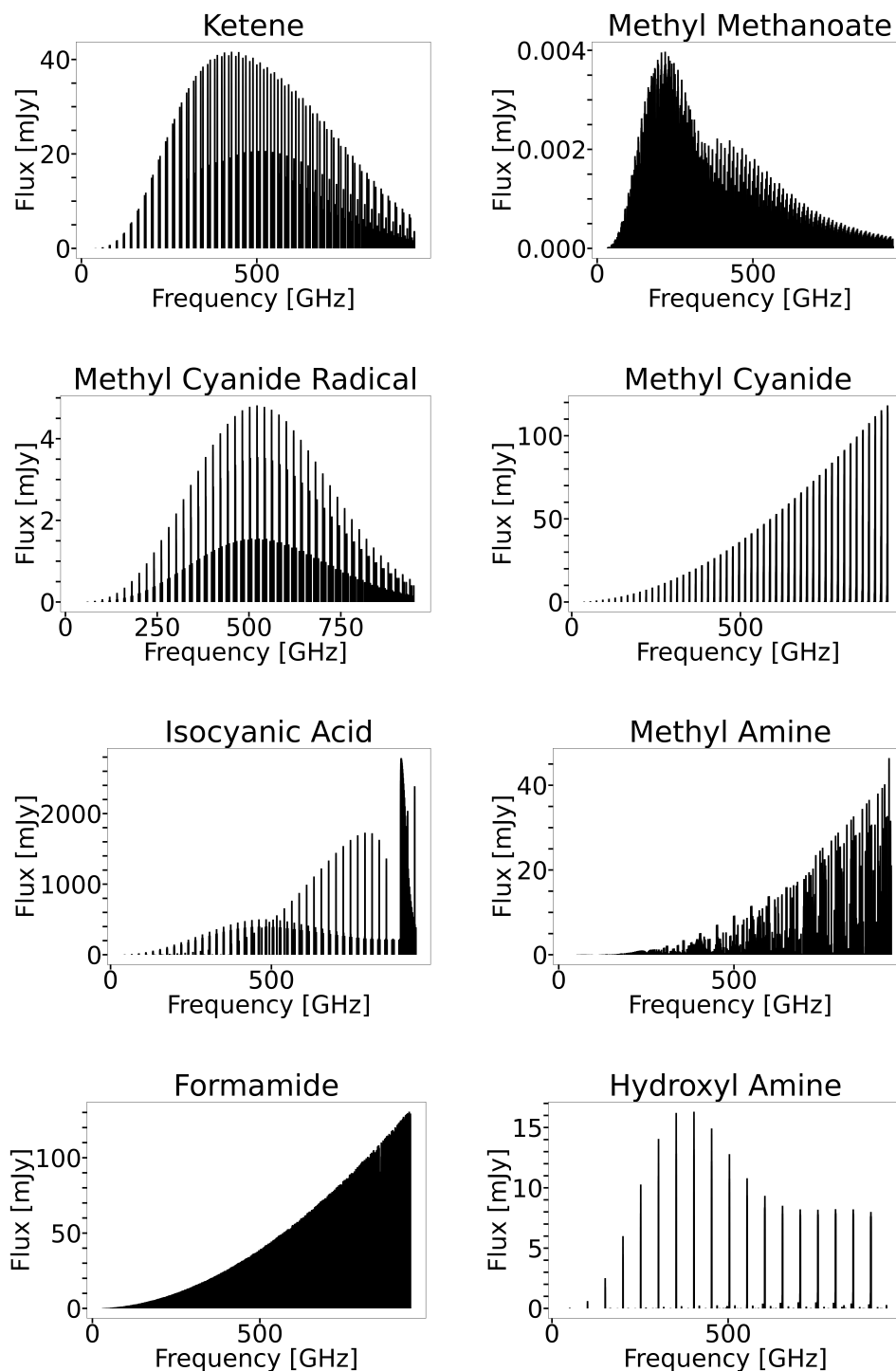
Figure 4.10: Disk-integrated line spectra of COMs simulated with abundances from the chemical model at 1Myr over the whole frequency coverage of ALMA - *continued*

When the disk line survey is run with abundances from the chemical model, it is seen that very densely populated spectra are predicted for almost all the molecules, especially the oxygen-bearing COMs, over the frequency range of ALMA. The maximum line flux predicted is that of isocyanic acid at 2.8 Jy at a frequency of 904 GHz, followed by formaldehyde at 2.2 Jy at a frequency of 823 GHz, which are also the molecules for which the peak integrated intensities were highest. The lines are seen to gain strength in terms of flux as we move towards larger frequencies (>500 GHz) for most of the species, with the exception of glycolaldehyde, ketene, methyl methanoate and hydroxyl amine whose lines fluxes are seen to peak at frequencies below 450 GHz. The maximum disk-integrated line fluxes range all the way down to 0.06 mJy, 0.02 mJy and 0.004 mJy for glycolaldehyde, dimethyl ether and methyl methanoate respectively, making the latter the molecule with the weakest lines in the survey when run with abundances from the chemical model.

Figures 4.11, 4.12 and 4.13 provide the disk-integrated line spectra of the chosen COMs from the line survey using the abundances from the parametric model over the whole frequency range with ALMA. In the parametric models, the reservoir of the COMs is constrained within 20-50 K at a fixed fractional abundance of 3.3×10^{-10}.
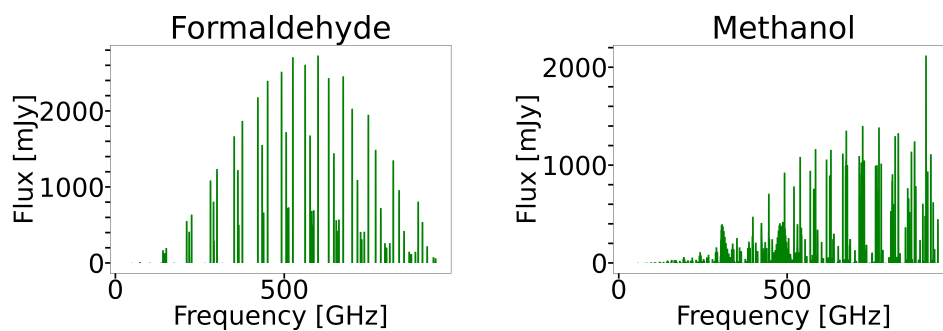
Figure 4.11: Disk-Integrated Line Spectra of COMs simulated with abundances from the parametric model over the whole frequency coverage of ALMA
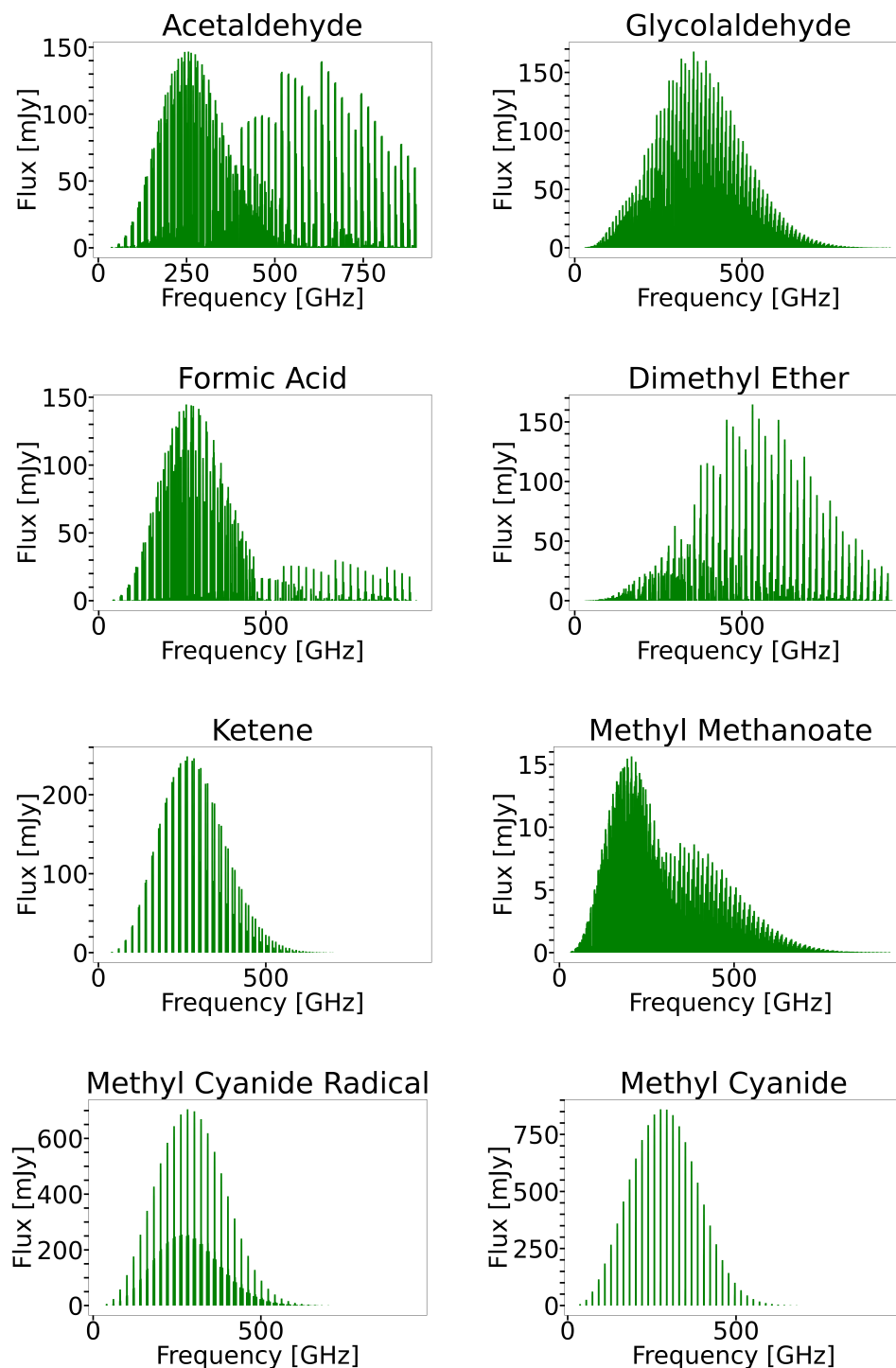
Figure 4.12: Disk-Integrated Line Spectra of COMs simulated with abundances from the parametric model over the whole frequency coverage of ALMA - *continued*
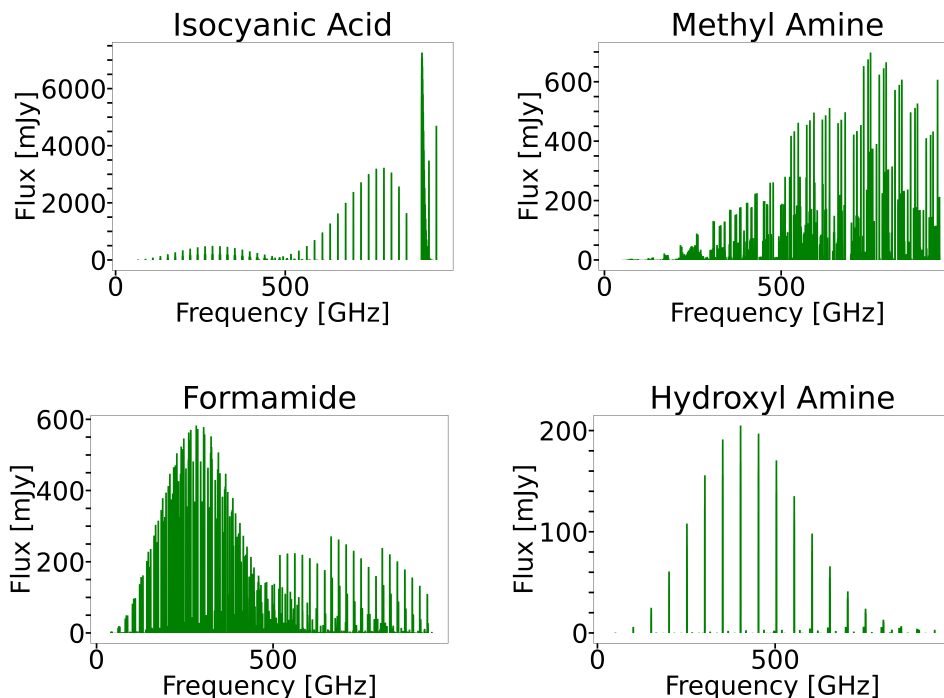
Figure 4.13: Disk-Integrated Line Spectra of COMs simulated with abundances from the parametric model over the whole frequency coverage of ALMA - *continued*

When the disk line survey is run with abundances from the parametric model, it is seen that the maximum predicted line strength is greater for all molecules and they occur at lower frequencies (except for methanol, glycolaldehyde, isocyanic acid and hydroxyl amine, for which the peaks occur at the same frequencies of 912 GHz, 356 GHz, 903 GHz and 403 GHz respectively, as when the survey is run with abundances from the chemical model) than those predicted with the chemical model. The maximum integrated line flux is again that of isocyanic acid, but at an almost three times larger magnitude of 7.2 Jy, followed again by formaldehyde at 2.7 Jy. The peaks are now seen to have shifted towards the lower end of the spectrum, except for methanol, isocyanic acid and hydroxyl amine whose lines still peak at frequencies >750 GHz. The maximum line flux ranges all the way down to 16 mJy for methyl methanoate, making the latter again the molecule with the weakest lines whose maximum also occurs at the lowest frequency of 207 GHz, in the survey when run with abundances from the parametric model.

Table 4.2 shows how the strongest lines observable with ALMA from the chemical model compare with those from the parametric model.

Molecule	Chemical Model		Parametric Model	
	Frequency/GHz	**Peak Flux/mJy**	**Frequency/GHz**	**Peak Flux/mJy**
Formaldehyde	823.083	2199	600.331	2728
Methanol	912.109	113	912.109	2119
Acetaldehyde	548.125	17	255.385	147
Glycolaldehyde	356.137	0.06	356.137	168
Formic acid	930.261	110	262.104	145
Methanoic acid	*No molecular data available*			
Dimethyl ether	687.037	0.02	532.325	165
Ketene	428.055	42	265.095	248
Methyl methanoate	218.298	0.004	206.619	16
Methyl cyanide radical	521.834	5	281.500	705
Methyl cyanide	936.109	118	275.916	860
Isocyanic acid	903.919	2786	903.369	7262
Methyl amine	942.618	46	752.906	698
Formamide	946.209	131	282.569	583
Hydroxyl amine	402.847	16	402.847	205

Table 4.2: Comparison of the strongest lines predicted by the line survey using abundances from the chemical model and the parametric model in the ALMA regime

As seen from table 4.2, when the disk line survey is run with abundances from the parametric model, the line fluxes peak at lower frequencies (with the exception of methanol, glycolaldehyde, isocyanic acid and hydroxyl amine). The magnitudes of the peak fluxes are also larger for all the molecules with the parametric model, with ratios of the predicted maximum line strength with the parametric model to that with the chemical model being as high as 8250 for dimethyl ether and reaching values of 1.2 for formaldehyde, for which the difference is relatively smaller. When the reservoir of the COMs is constrained within 20-50 K at a fixed fractional abundance of 3.3×10^{-10}, relatively stronger line at generally lower frequencies are therefore predicted than when the abundances are taken from the chemical model.

4.3.3 Line Survey of Complex Organic Molecules in the HD 100546 Disk with SKA

In this subsection, the integrated line intensities and line profiles of the chosen COMs (except hydroxyl amine, for which no output file was generated, as the intensities predicted were below the cut-off value) predicted in the line survey using both the chemical and parametric models in the SKA frequency range of 0-30 GHz are reported in two parts. Given the exploratory nature of this work, the whole frequency coverage over the two prospective phases of SKA has been considered in this work. Comparisons between the predictions made from each model are also provided in terms of the highest-integrated intensity and the maximum-flux lines.

Integrated Intensities of the Molecular Emission of Complex Organic Molecules in the HD 100546 Disk from the Chemical Model and the Parametric Model in the SKA Frequency Range

Figures 4.14, 4.15 and 4.16 show the plots of the integrated intensities from the line survey using the abundances from the chemical model over the whole frequency range with SKA.

Figure 4.14: Integrated intensities of the molecular emission of COMs simulated with abundances from the chemical model at 1Myr at SKA wavelengths

Figure 4.15: Integrated intensities of the molecular emission of COMs simulated with abundances from the chemical model at 1Myr at SKA wavelengths - *continued*

Figure 4.16: Integrated intensities of the molecular emission of COMs simulated with abundances from the chemical model at 1Myr at SKA wavelengths - *continued*

When the disk line survey is run with abundances from the chemical model, it is seen that most of the molecules do not have many transitions to contribute to significant integrated intensities in the SKA frequency range, such that sparsely-populated plots of were returned. The maximum integrated intensity predicted is that of isocyanic acid at 813 μJy kms^{-1} at a frequency of 22 GHz, followed by formaldehyde at 243 μJy kms^{-1} at a frequency of 29 GHz. The integrated intensity is seen to peak in the prospective phase 3 frequency range (14-30 GHz) of SKA for all molecules. The maximum integrated intensities range all the way down to 0.006 μJy kms^{-1} and 0.004 μJy kms^{-1} for methyl methanoate and dimethyl ether respectively, making the latter the molecule with the minimum peak integrated intensity predicted at the upper limit of 30 GHz of the phase 3 frequency range, in the survey when run with abundances from the chemical model.

Figures 4.17 and 4.18 show the plots of the integrated intensities from the line survey using the abundances from the parametric model over the SKA frequency range. In

the parametric models, the reservoir of the COMs is constrained within 20-50 K at a fixed fractional abundance of 3.3×10^{-10}.
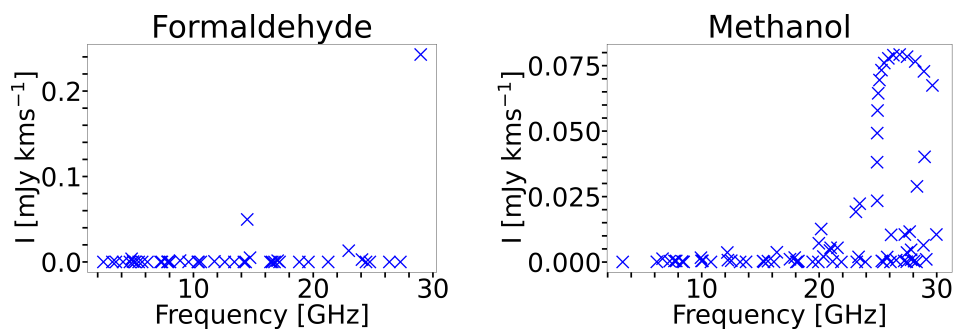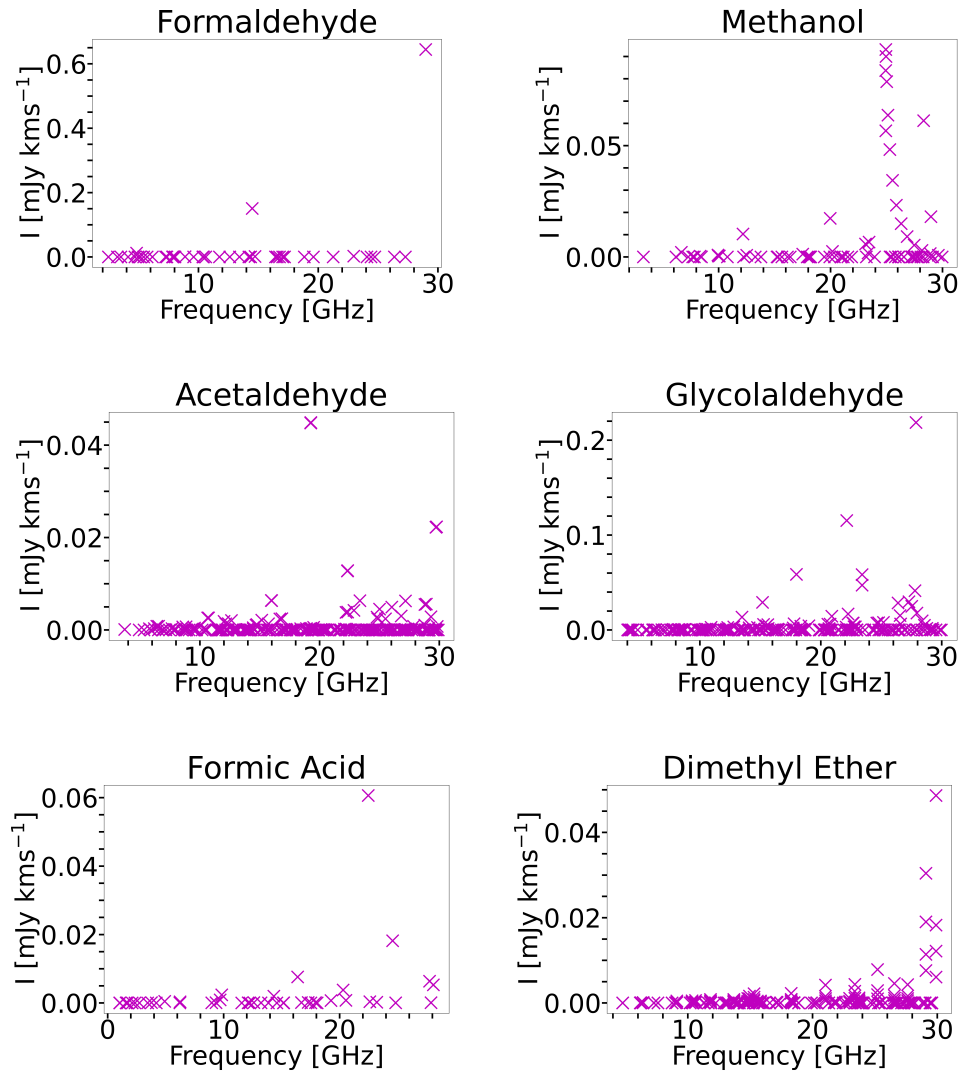

Figure 4.17: Integrated intensities of the molecular emission of COMs simulated with abundances from the parametric model at SKA wavelengths
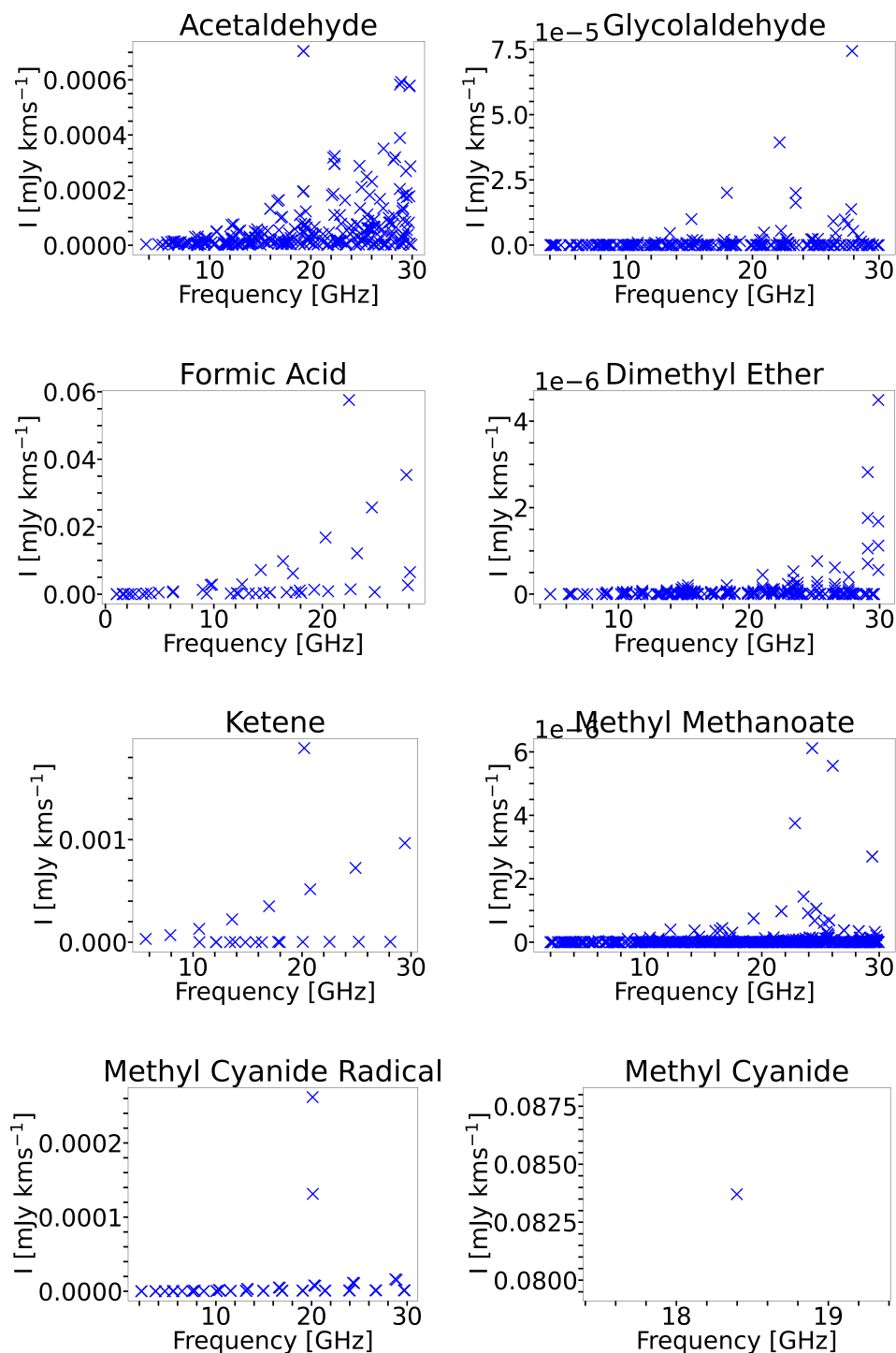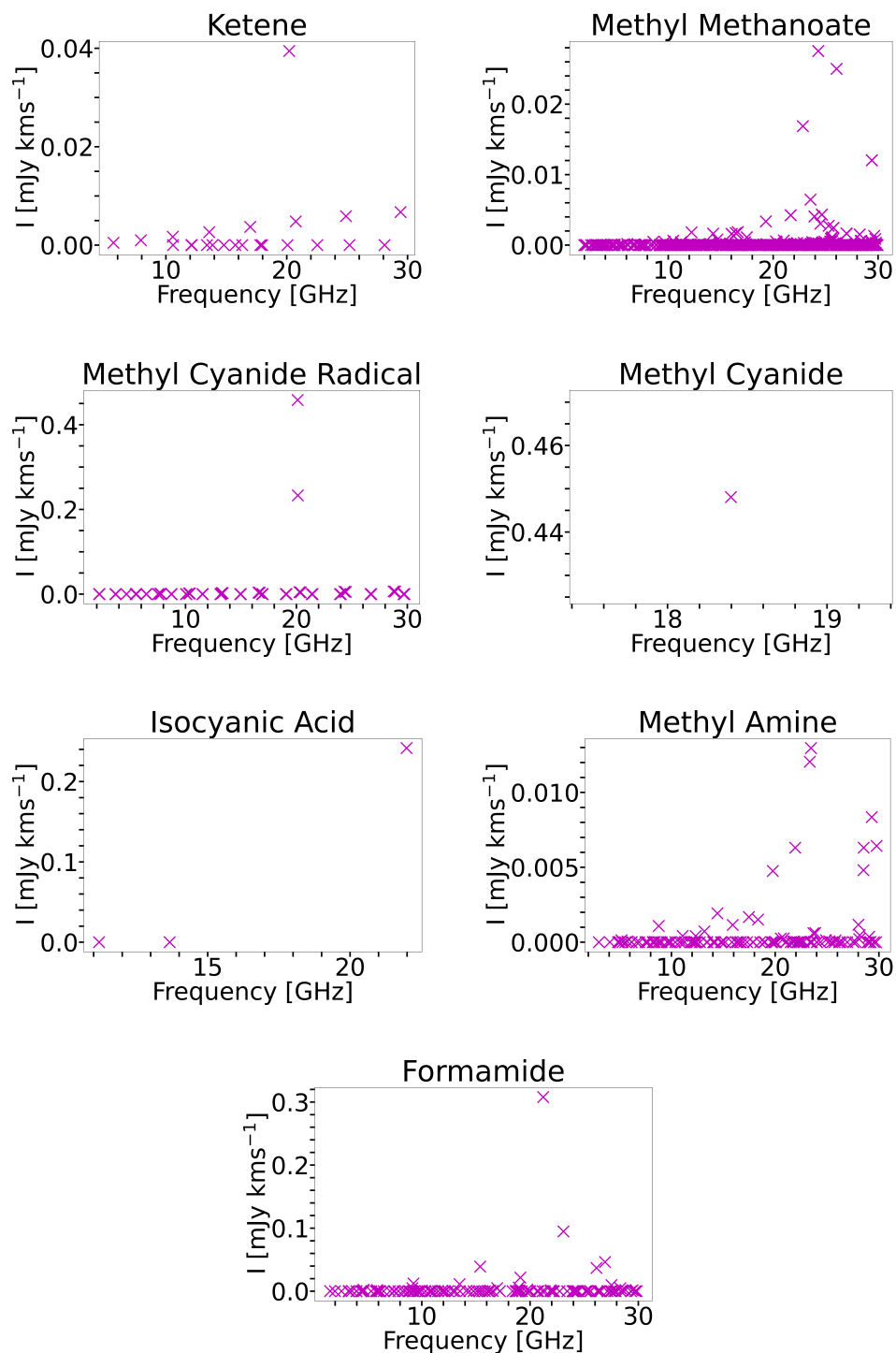
Figure 4.18: Integrated intensities of the molecular emission of COMs simulated with abundances from the parametric model at SKA wavelengths - *continued*
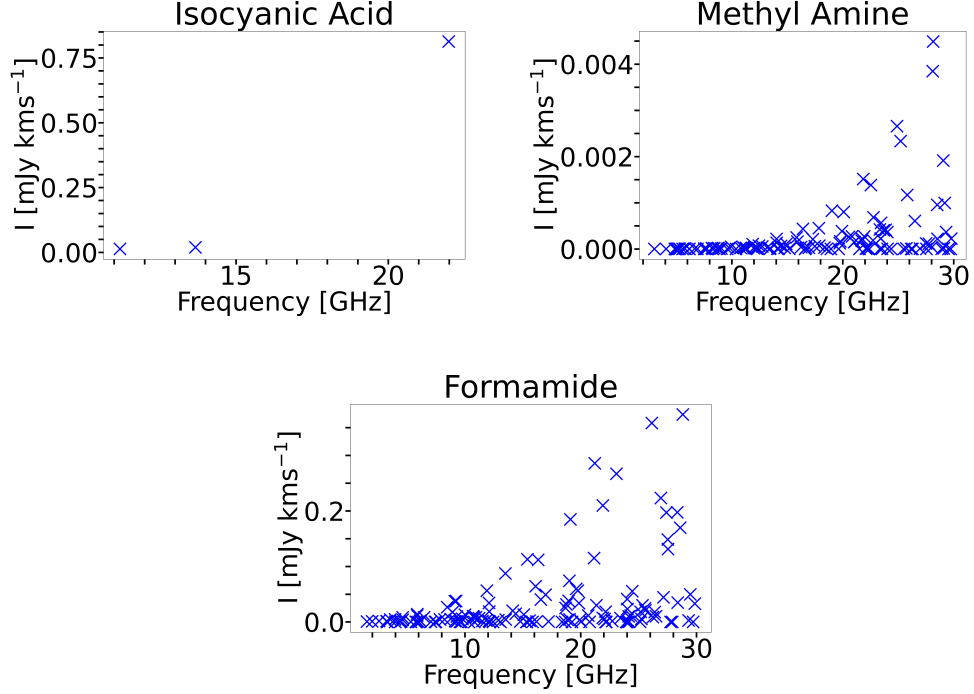
When the disk line survey is run with abundances from the parametric model, the maximum integrated intensities are seen to be much larger but within the same frequency range as when the survey was run with abundances from the chemical model. The maximum peak integrated intensity predicted is now that of formaldehyde at 644 μJy kms^{-1} at a frequency of 29GHz, followed by methyl cyanide radical at 458 μJy kms^{-1} at a frequency of 20 GHz. The maximum integrated intensities range all the way down to 28 μJy kms^{-1} for methyl methanoate and 13 μJy kms^{-1} for methyl amine, making the latter the molecule with the minimum peak integrated intensity at a frequency of 23 GHz in the survey when run abundances from the parametric model.

Table 4.3 shows the frequencies at which the integrated intensity is maximum from the chemical model and the parametric model in the SKA frequency range.

Molecule	Chemical Model		Parametric Model	
	Frequency/GHz	Integrated Intensity/μJy km s^{-1}	Frequency/GHz	Integrated Intensity/μJy km s^{-1}
Formaldehyde	28.975	243	28.975	644
Methanol	26.847	79	24.933	93
Acetaldehyde	19.265	0.7	19.265	45
Glycolaldehyde	27.871	0.07	27.871	219
Formic acid	22.471	58	22.471	61
Methanoic acid	*No molecular data available*			
Dimethyl ether	29.901	0.004	29.901	47
Ketene	20.209	2	20.209	39
Methyl methanoate	24.299	0.006	24.299	28
Methyl cyanide radical	20.116	0.3	20.116	458
Methyl cyanide	18.398 *(single freq)*	84	18.398 *(single freq)*	448
Isocyanic acid	21.982	813	21.982	242
Methyl amine	28.143	4	23.450	13
Formamide	28.816	374	21.207	308
Hydroxyl amine	*No prediction made*			

Table 4.3: Comparison of the lines with the maximum integrated intensity predicted by the line survey using abundances from the chemical model and the parametric model in the SKA regime

As seen from table 4.3, when the disk line survey is run with abundances from the parametric model, the integrated intensities peak at about the same frequencies but having values generally higher for all the molecules with the parametric model, with ratios of the predicted maximum integrated intensity with the parametric model to that with the chemical model being the highest for dimethyl ether, for which the parametric model predicts a four-order-of-magnitude higher integrated intensity, and lowest for formic acid, for which both models predict about the same values for integrated intensity

at about 60 μJy km s^{-1}. When the reservoir of the COMs is constrained within 20-50K at a fixed fractional abundance of 3.3×10^{-10}, relatively stronger integrated intensities at about the same frequencies are therefore predicted than when the abundances are taken from the chemical model.

Disk-Integrated Line Spectra of Complex Organic Molecules in the HD 100546 Disk from the Chemical Model and the Parametric Model in the SKA Frequency Range

Figures 4.19, 4.20 and 4.21 provide the disk-integrated line spectra of the chosen COMs (with the exception of methanoic acid whose molecular data file was unavailable, and hydroxyl amine, for which no prediction was returned) from the line survey using the abundances from the chemical model over the whole frequency range with SKA.

Figure 4.19: Disk-Integrated Line Spectra of COMs simulated with abundances from the chemical model at 1Myr at SKA wavelengths

Figure 4.20: Disk-Integrated Line Spectra of COMs simulated with abundances from the chemical model at 1Myr at SKA wavelengths - *continued*
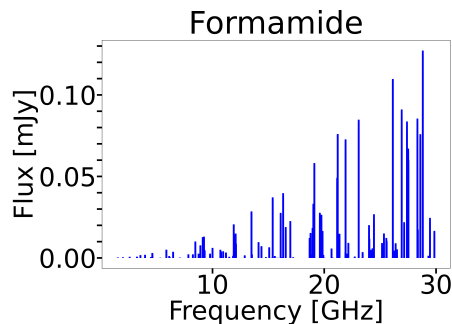
Figure 4.21: Disk-Integrated Line Spectra of COMs simulated with abundances from the chemical model at 1Myr at SKA wavelengths - *continued*

When the disk line survey is run with abundances from the chemical model, it is seen that significant ranges of fluxes of the lines are predicted for the different species, from relatively strong lines at 422 μJy for the 22 GHz-isocyanic acid line to very weak lines at 0.006 μJy for the 24 GHz-methyl methanoate line. Stronger lines are predicted within that frequency range for the smaller (four-to-five-atom-bearing) molecules. The maximum integrated intensity predicted is that of isocyanic acid at 6.7 Jy kms^{-1} at a frequency of 905 GHz, followed by formaldehyde at 4.2 Jy kms^{-1} at a frequency of 897 GHz. The line fluxes are seen to peak at the phase 3-end (14 GHz - 30 GHz) of the SKA frequency range for all molecules.

Figures 4.22 and 4.23 provide the disk-integrated line spectra of the chosen COMs (with the exception of methanoic acid whose molecular data file was unavailable, and hydroxyl amine) from the line survey using the abundances from the parametric model over the whole frequency range with SKA. In the parametric models, the reservoir of the COMs is constrained within 20-50 K at a fixed fractional abundance of 3.3×10^{-10}. When the disk line survey is run with abundances from the parametric model, it is seen that with the exception of isocyanic acid, larger fluxes are predicted for all the molecules which peak at roughly the same frequencies. The maximum line flux is now that of formaldehyde at 670 μJy, predicted again at the upper limit of 29 GHz of the SKA frequency range. It is followed by the 18 GHz-methyl cyanide line which has a flux of 467 μJy and the 20 GHz-line of its radical with a peak flux of 479 μJy. The maximum fluxes range all the way down to 14 μJy for methyl amine, making the latter the molecule with the minimum peak flux in the survey when run abundances from the
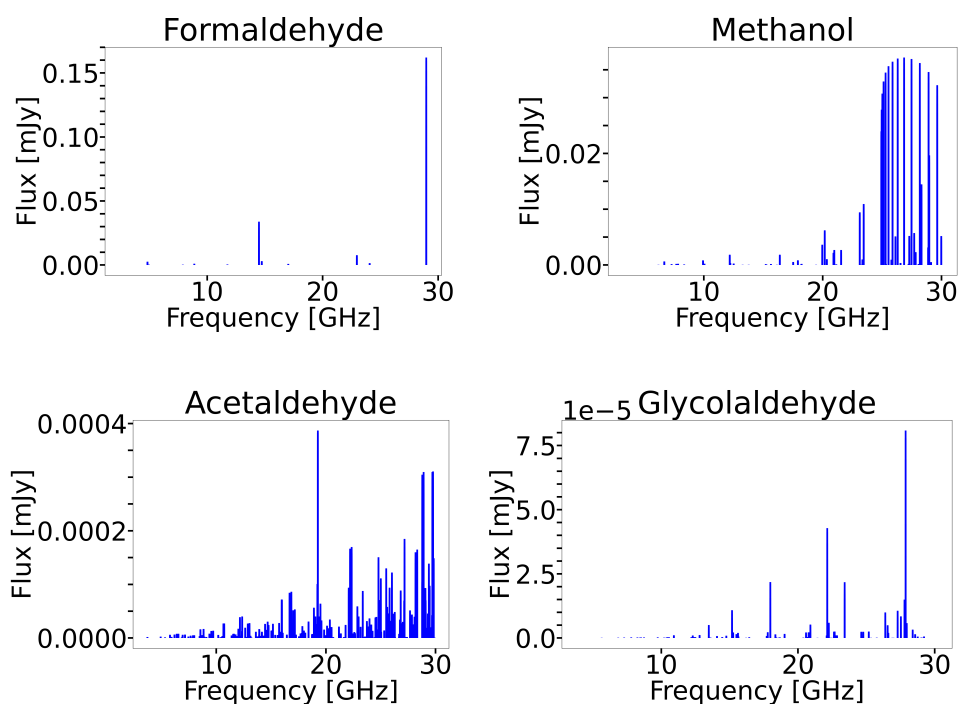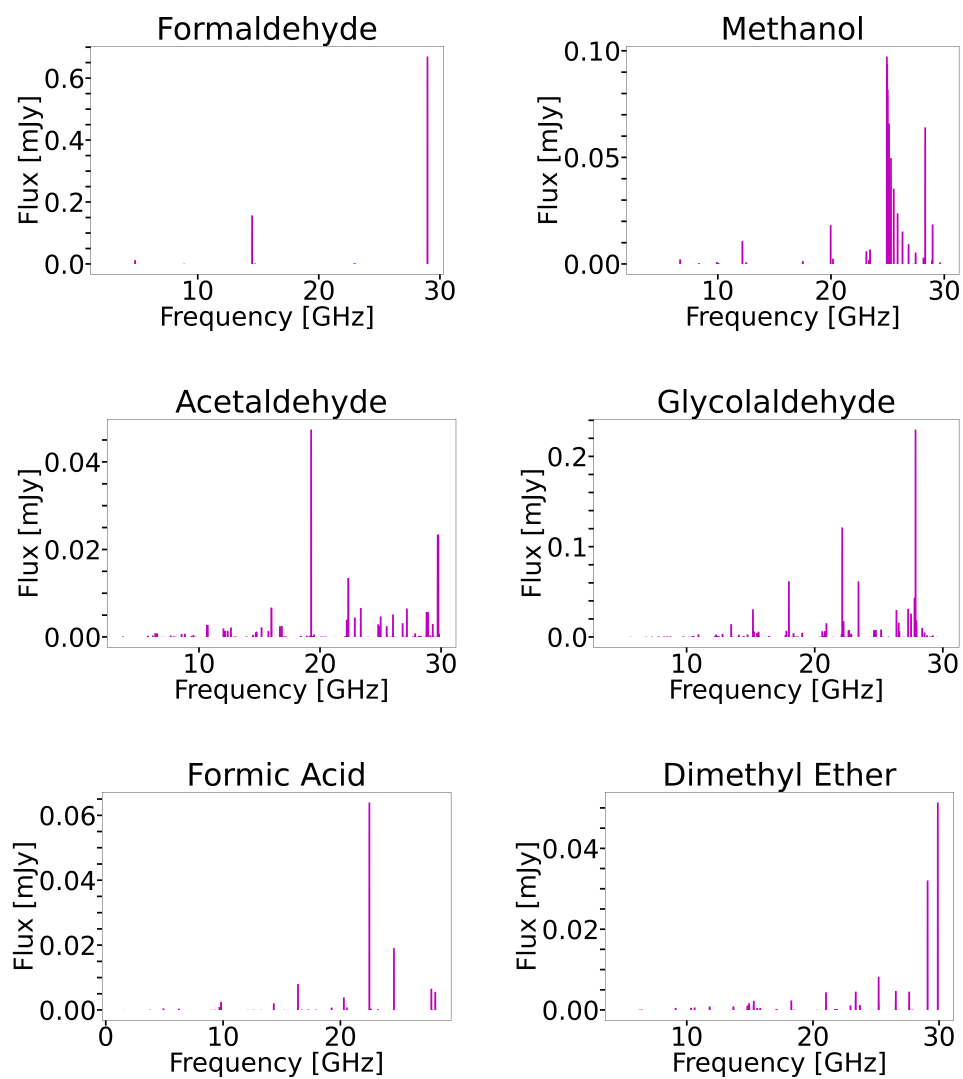
parametric model.

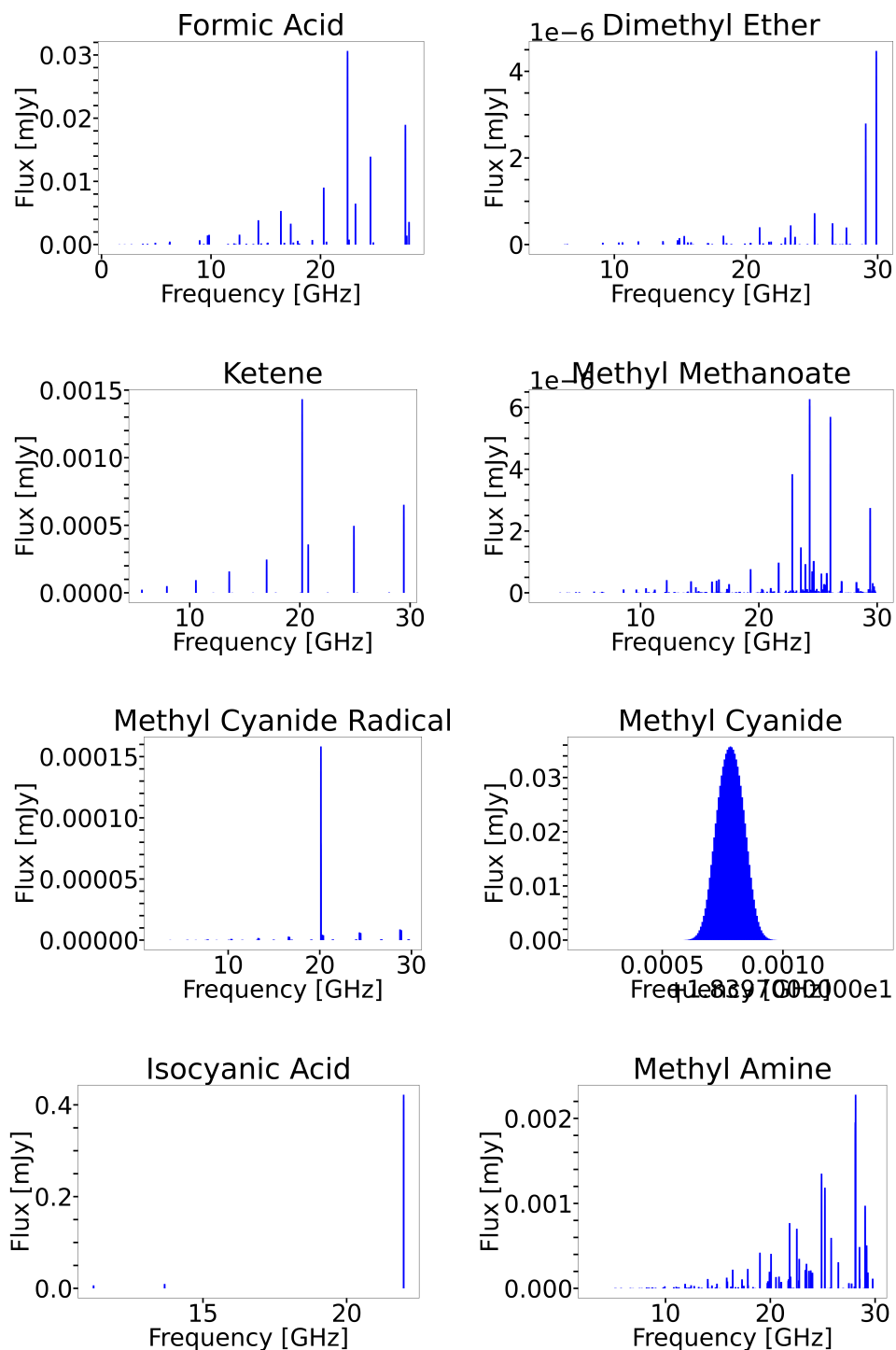Figure 4.22: Disk-Integrated Line Spectra of COMs simulated with abundances from the parametric model at SKA wavelengths
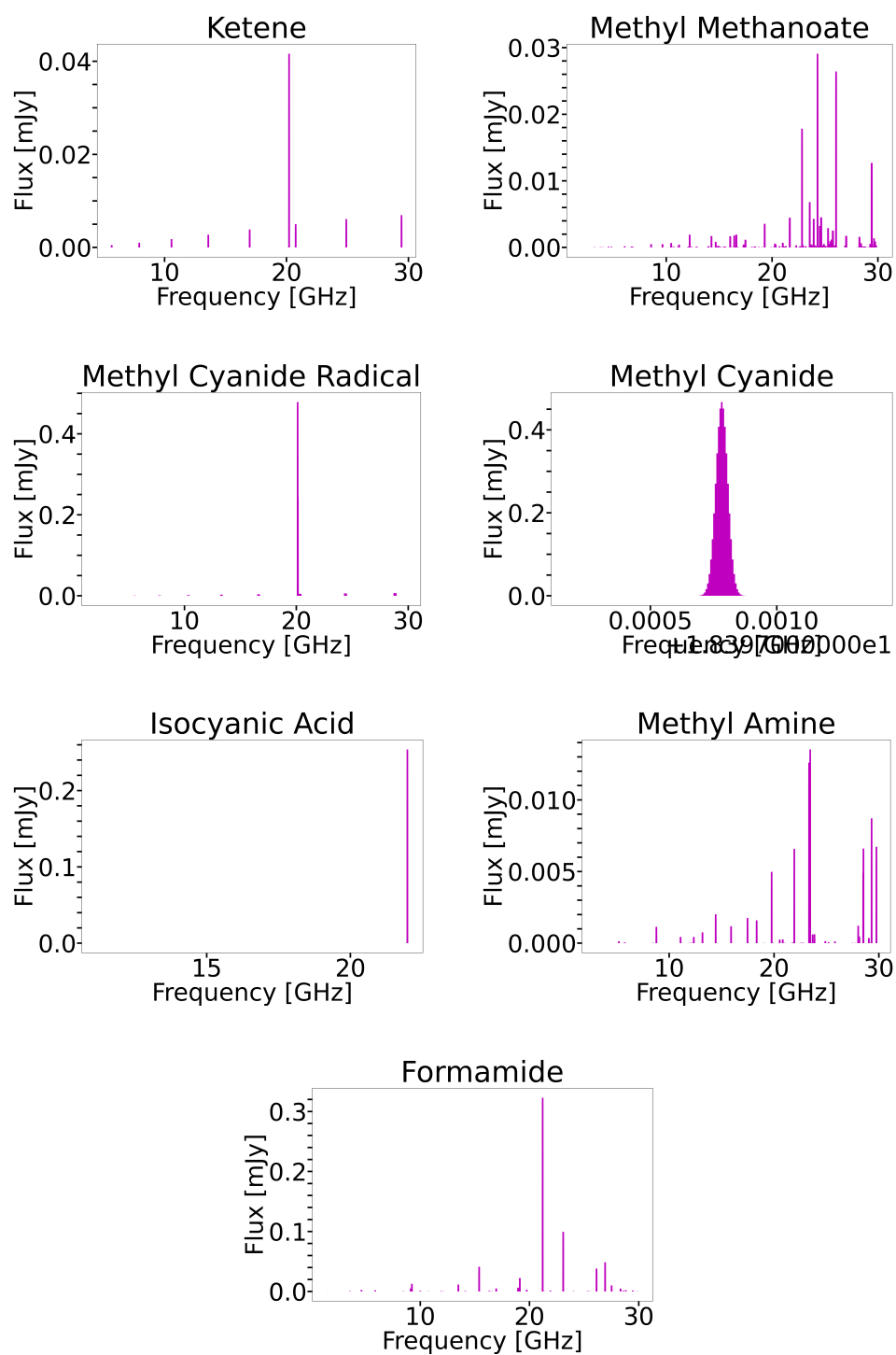
Figure 4.23: Disk-Integrated Line Spectra of COMs simulated with abundances from the parametric model at SKA wavelengths - *continued*

Table 4.4 shows how the strongest lines observable with SKA from the chemical model compare with those from the parametric model.

Molecule	Chemical Model		Parametric Model	
	Frequency/GHz	**Flux/μJy**	**Frequency/GHz**	**Flux/μJy**
Formaldehyde	28.975	162	28.975	670
Methanol	26.847	37	24.933	97
Acetaldehyde	19.265	0.4	19.265	47
Glycolaldehyde	27.871	0.08	27.871	230
Formic acid	22.471	31	22.471	64
Methanoic acid	*No molecular data available*			
Dimethyl ether	29.901	0.004	29.901	51
Ketene	20.209	1	20.209	42
Methyl methanoate	24.299	0.006	24.299	29
Methyl cyanide radical	20.116	0.2	20.116	479
Methyl cyanide	18.398	36	18.398	467
Isocyanic acid	21.982	422	21.982	254
Methyl amine	28.143	2	23.450	14
Formamide	28.816	127	21.207	323
Hydroxyl amine	*No line predicted*			

Table 4.4: Comparison of the strongest lines predicted by the line survey using abundances from the chemical model and the parametric model in the SKA regime

As seen from table 4.4, when the disk line survey is run with abundances from the parametric model, the disk-integrated line fluxes peak at the same frequencies but have greater values, except for isocyanic acid, for which the parametric model predicts a peak flux which is smaller by a factor of 2. The ratio of the predicted maximum line flux with the parametric model to that with the chemical model is seen to be the highest for dimethyl ether, and lowest for formic acid, for which the peak line flux predicted by the parametric model is only twice that predicted by the chemical model. When the reservoir of the COMs is constrained within 20-50K at a fixed fractional abundance of 3.3×10^{-10}, relatively stronger lines at generally the same frequencies are therefore predicted than when the abundances are taken from the chemical model.

4.4 Discussion

Table 4.5 pulls out the strongest lines observable in the different bands with ALMA from the parametric model and their properties. Apart from formaldehyde, dimethyl ether and methyl amine, for which the fourth, fifth and third strongest line respectively are chosen for observation with ALMA due to their strongest lines being outside the observable ranges of ALMA bands, the strongest lines are chosen for observation for all the species.

ALMA band	Molecule	Transition	E_{UP}/K	E_A/s^{-1}	Frequency/GHz	Integrated Intensity/mJy km s^{-1}	Peak Flux/mJy
Band 5	Methyl methanoate	$16_{3,13,0} - 15_{3,12,0}$	89.2	1.28×10^{-4}	206.619	15	16
Band 6	Acetaldehyde	$13_{1,12,0} - 12_{1,11,0}$	88.4	5.86×10^{-4}	255.385	146	147
	Formic acid	$12_{0,12} - 11_{0,11}$	82.8	1.95×10^{-4}	262.104	144	145
	Ketene	$13_{1,12} - 12_{1,11}$	102.1	2.10×10^{-4}	265.095	254	248
Band 7	Glycolaldehyde	$10_{10,1} - 9_{9,0}$	91.3	1.29×10^{-3}	356.137	165	168
	Methyl cyanide radical	$14_{0,14,15} - 13_{0,13,14}$	101.4	1.54×10^{-3}	281.500	791	705
	Methyl cyanide	$15_0 - 14_0$	105.9	1.82×10^{-3}	275.916	1008	860
	Formamide	$13_{1,12} - 12_{1,11}$	98.4	1.64×10^{-3}	282.569	634	583
Band 8	Formaldehyde	$7_{1,7} - 6_{1,6}$	106.3	3.44×10^{-3}	491.968	3057	2515
	Hydroxyl amine	$8_{0,8} - 7_{0,7}$	87.0	1.24×10^{-4}	402.847	202	205
Band 9	Dimethyl ether	$9_{8,2,1} - 8_{7,2,1}$	109.8	1.77×10^{-3}	609.712	148	152
Band 10	Methanol	$3_{3,1,0} - 2_{2,1,0}$	76.6	5.85×10^{-3}	912.109	2168	2119
	Isocyanic acid	$6_{1,5} - 6_{0,6}$	65.5	7.87×10^{-3}	903.369	8633	7262
	Methyl amine	$5_{4,5} - 4_{3,5}$	94.5	3.06×10^{-3}	797.219	657	665

Table 4.5: Properties - values of the line frequencies, Einstein A coefficients, upper energy levels (E_{UP}/K) (obtained from the LAMDA database) and fluxes - of the strongest lines predicted by the line survey observable in each ALMA band using abundances from the parametric model

The chosen lines are observable within the ALMA bands 5-10. The strongest line is the $6_{1,5} - 6_{0,6}$ isocyanic acid line with a peak flux of 7.3 Jy. The next strongest lines are the those of the already detected molecules, methanol and formaldehyde. Potential lines for observations with ALMA will then be those of nitrogen-bearing methyl cyanide ($15_0 - 14_0$) and methyl amine ($5_{4,5} - 4_{3,5}$) in bands 7 and 10 respectively. All the lines are seen to require temperatures of 65 K - 110K for the transitions to occur, with the lowest E_{UP} being that of isocyanic acid at 65.5 K for the $6_{1,5} - 6_{0,6}$ transition and the $9_{8,2,1} - 8_{7,2,1}$ transition of dimethyl ether having the highest E_{UP} of 109.8 K. It is to note that one of the caveats of the calculations done in this chapter is that dust is not considered. The detection of molecular line emission due to transitions at high frequencies is affected as the dust is optically thick at these frequencies. This can be taken into account in future calculations. The respective required integration times for

observation, for a signal-to-noise ratio (SNR) of 5, with a 1 km s^{-1} channel spacing and a 0.2" spatial resolution can be computed in the future using the onine ALMA Sensitivity Calculator (https://almascience.eso.org/proposing/sensitivity-calculator) to assess how long and feasible the observation of each line is.

Table 4.6 pulls out the properties of the strongest lines observable with SKA from the parametric model.

Molecule	Transition	E_{Up}/K	E_A/s^{-1}	Frequency/GHz	Integrated Intensity/μJy km s^{-1}	Peak Flux/μJy
Formaldehyde	$3_{1,2} - 3_{1,3}$	33.5	1.28×10^{-7}	28.975	644	670
Methanol	$4_{2,2,0} - 4_{1,3,0}$	45.5	7.87×10^{-8}	24.933	93	97
Acetaldehyde	$1_{0,1,0} - 0_{0,0,0}$	0.92	1.75×10^{-7}	19.265	45	47
Glycolaldehyde	$5_{1,4} - 5_{0,5}$	9.39	4.21×10^{-7}	27.871	219	230
Formic acid	$1_{0,1} - 0_{0,0}$	1.08	8.58×10^{-8}	22.471	61	64
Dimethyl ether	$1_{1,0,1} - 1_{0,1,1}$	2.34	2.64×10^{-7}	29.901	49	51
Ketene	$1_{0,1} - 0_{0,0}$	0.97	6.48×10^{-8}	20.209	39	42
Methyl methanoate	$2_{0,2,0} - 1_{0,1,0}$	1.75	1.77×10^{-7}	24.299	28	29
Methyl cyanide radical	$1_{0,1,2} - 0_{0,0,1}$	0.97	3.87×10^{-7}	20.116	458	479
Methyl cyanide	$1_0 - 0_0$	0.88	3.71×10^{-7}	18.398	448	467
Isocyanic acid	$1_{0,1} - 0_{0,0}$	1.05	1.03×10^{-7}	21.982	242	254
Methyl amine	$6_{1,2} - 5_{2,3}$	49.23	1.62×10^{-8}	23.450	13	14
Formamide	$1_{0,1} - 0_{0,0}$	1.02	4.84×10^{-7}	21.207	308	323

Table 4.6: Properties - values of the line frequencies, Einstein A coefficients, upper energy levels (E_{UP}/K) (obtained from the LAMDA database) and fluxes - of the strongest lines predicted by the line survey using abundances from the parametric model in the SKA regime

All the chosen lines are observable within the SKA frequency range of 14-30 GHz. The strongest line is the $3_{1,2} - 3_{1,3}$ formaldehyde line with a peak flux of 670 μJy. Following the already detected molecule are methyl cyanide, its radical, isocyanic acid and glycolaldehyde, whose $1_0 - 0_0$, $1_{0,1,2} - 0_{0,0,1}$, $1_{0,1} - 0_{0,0}$ and $5_{1,4} - 5_{0,5}$ lines respectively have fluxes of 448 μJy, 458 μJy, 242 μJy and 219 μJy at frequencies ranging from 18-28 GHz. Compared to the lines predicted in the ALMA frequency range, the lines predicted in the SKA regime are due to transitions between relatively lower energy levels with values ranging from 0.9 K - 50 K (with methyl amine at 49 K), with the E_{UP} of most molecules lying in the lower end of this range. The Einstein A coefficients of the lines predicted in the SKA frequency range are 3 to 4 orders of magnitudes lower than those predicted in the ALMA regime, implying the lower probability of emission at these lower frequencies. In general, it is also seen that the strengths of lines and the integrated intensities in the latter range are much smaller (by about three

orders of magnitude). The advantage of observing the emission of COMs at centimeter wavelengths with respect to observing it at sub-millimeter wavelengths is that we get over dust opacity issues in planet-forming regions. To assess how observable the lines are, they can be plotted against the sensitivity curve for SKA.

To date, the most complex molecule detected in a protoplanetary disk is dimethyl ether in the IRS 48 disk by Brunken et al. [2022] who also reported tentative identification of methyl formate. When compared to the observed intensities of COMs in other protoplanetary disks, the modelled integrated intensities from this work are comparable. The strongest line predicted is the isocyanic acid $5_{4,5}$-$4_{3,5}$ transition whose integrated intensity is 28 times stronger than the strongest detected $4_{2,2}$-$4_{2,1}$ line of formaldehyde. It is also two orders of magnitudes greater than that of the observed lines of methyl cyanide in MC 480 [Öberg et al., 2015] and that of the simplest organic acid, formic acid in TW Hya [Favre et al., 2018] which have been detected at 30 mJy kms^{-1} and 89 mJy kms^{-1} respectively with ALMA. The weakest line predicted among the chosen COMs is the $16_{3,13,0}$-$15_{3,12,0}$ line of methyl methanoate whose modelled integrated intensity is half of the observed line of methyl cyanide in MC 480 [Öberg et al., 2015]. The sensitivity of SKA at centimeter wavelengths will enable the detection of the lower energy level transitions of COMs [Jiménez-Serra et al., 2022], hinting towards possible observations of the tabulated lines for SKA. The modelled integrated intensities therefore make the chosen lines potential lines to be targeted in future observations. As shown in Chapter 2, the appreciable modelled column densities of the COMs also strengthen the case for the detection of the chosen lines of the COMs in this Chapter. Their detection will not only contribute in expanding the known reservoir of COMs in the HD 100546 disk but will provide further evidence that the chemistry of species are related.

4.5 Summary and Conclusions

Some important findings in this chapter are:

- The parametric model done in the disk line survey predicts abundances of methanol and formaldehyde in the thermally constrained region to be three orders of magnitude smaller than the maximum fractional abundance of gas-phase formaldehyde at 1 Myr from the chemical model.

- When the disk line survey is run with abundances from both the chemical model in both the ALMA and SKA frequency ranges, it is seen that the maximum integrated intensity predicted is that of isocyanic acid.

- When run in SKA regime, the integrated intensity plots are relatively sparsely-populated and lower values of integrated intensities and fluxes are predicted in the SKA frequency range.

- In the ALMA regime, the magnitudes of the peak fluxes are also larger for all the molecules with the parametric model, with ratios of the predicted maximum line strength with the parametric model to that with the chemical model being as high as 8250 for dimethyl ether and reaching values of 1.2 for formaldehyde, for which the difference is relatively smaller.

- The ratio of the predicted maximum line flux in the SKA frequency range with the parametric model to that with the chemical model is seen to be the highest for dimethyl ether, and lowest for formic acid, for which the peak line flux predicted by the parametric model is only twice that predicted by the chemical model.

- When the disk line survey is run with abundances from the parametric model in the ALMA regime, the integrated intensities peak at generally lower frequencies.

- In the ALMA frequency range, the strongest line is the $6_{1,5} - 6_{0,6}$ isocyanic acid line with a peak flux of 7.3 Jy.

- The strongest lines predicted in the SKA regime after formaldehyde are those of methyl cyanide, its radical, isocyanic acid and glycolaldehyde, whose $1_0 - 0_0$, $1_{0,1,2} - 0_{0,0,1}$, $1_{0,1} - 0_{0,0}$ and $5_{1,4} - 5_{0,5}$ lines respectively have fluxes of 448 μJy, 458 μJy, 242 μJy and 219 μJy at frequencies ranging from 18-28 GHz.

Exploring the chemical complexity of the HD 100546 disk through the prediction of the line fluxes of COMs is vital in providing insights in the habitability of planets formed from its material. Being one of the only three disks in which methanol is detected, our predictions further enhance the interest in this disk as most of the lines predicted in this work are reasonably strong. Future sensitivity calculations will allow us to assess assess how long and feasible the observations of the lines are. When the abundances of formaldehyde and methanol from the chemical model are scaled down by

three orders of magnitude and constrained within the 20-50 K temperature range, and the line survey is run assuming a face-on disk where LTE prevails, there is agreement between the observed and predicted line fluxes. With the upcoming progress of the further phases of SKA, a number of lines for each COM can be targeted to detect transitions which are not observable with ALMA. If identified, these lines will enrich our knowledge of the known reservoir of COMs of this planet-containing Herbig disk, proving to be interesting findings in assessing the habitability of planets formed from such disks.

CHAPTER 5

Summary and Conclusions

Protoplanetary disks are important astrophysical objects which contain all the material, gas and dust, from which planets form. The composition of a the latter is therefore set by the chemistry in its parent protoplanetary disk. Small, simple molecules have traditionally been detected in protoplanetary disks but owing to the high sensitivity of the Atacama Large Millimetre/submillimetre Array (ALMA), the inventory of the more complex ones is increasing with molecules as complex as dimethyl ether being recently detected in the disk around IRS 48 by Brunken et al. [2022]. Quantifying the complex organic molecular content of these planet-forming disks is crucial in determining the potential habitability of exoplanetary systems as the complex organic molecules (COMs) detected in star-forming regions are the precursors of the prebiotic molecules that can lead to the emergence of life. By studying COMs in more evolved protoplanetary disks, we can gain a better understanding of how they are incorporated into planets. In protoplanetary disks older than 1 Myr, even the most abundant COM, methanol, which is also vital in the chemistry leading to larger COMs [Öberg et al., 2009], is difficult to detect. The recent detection of methanol by Booth et al. [2021b] in the HD 100546 protoplanetary disk makes the latter an apt candidate for the exploration of further molecular complexity in warm Herbig disks. This project which has been carried out in three parts, namely:

1. to analyse the output of the chemical model by Walsh et al. [2012] previously run on the physical structure by Kama et al. [2016] of the disk, by quantifying the abundances of 15 chosen COMs which are the simplest members of organic functional groups, hence representing the next step in building molecular complexity

2. predict the spectra of the molecular emission in the ALMA and SKA regimes by running a line survey on the disk using the radiative transfer code by Walsh et al. [2014b]

3. reproduce the observed radial profiles obtained in a recent private communication by running the non-LTE radiative transfer code *LIME*, for lines of formaldehyde and methanol.

Some of the important findings in this work are:

- Substantial reservoirs (reaching as high as 10^{19} cm^{-2} in the gas state and 10^{20} cm^{-2} in the ice state) of COMs in both the gas and ice states are seen in disk with little depletion in most of them over the years.

- Larger organics, such as methanoic acid (CH_3COOH), dimethyl ether (CH_3OCH_3), glycolaldehyde (CH_2OHCHO) are among the least abundant in the gas state over the years, with the lowest maximum column density being that of glycolaldehyde at 3.8×10^{10} cm^{-2} at 117 au at 8 Myr.

- Ice-state COMs are seen in significant reservoirs in the outer disk, with the exception of the methyl cyanide radical (CH_2CN).

- The co-existence of the gas and ice states of the COMs is also seen, with the radial ice-to-gas ratio of the COMs reaching as high as 0.5 for formaldehyde (H_2CO), ketene (CH_2CO) and isocyanic acid (HNCO).

- As we progress over the years from 1 Myr to 8 Myr, a general decrease in the maximum column densities of all the gas-phase species is noted.

- Contrary to oxygen-bearing COMs, the peak column density of ice-state nitrogen-bearing COMs suffer significant decreases by three orders of magnitude, the maximum decrease being of methyl cyanide.

- For all the species, the maximum fractional abundance of their gas state generally decrease as we progress from 1 Myr to 5 Myr as opposed to little to no variation in that of the ice state.

- The most abundant molecule in the gas state at all three timestamps is the N- and O-bearing organic molecule formamide which peaks at 4.7×10^{-7} cm^{-3} at 1 Myr to 2.3×10^{-7} cm^{-3} at 5 Myr, at the constant location of (185, 6.42) in (r,z) coordinates.

- The most abundant molecule in the ice-state at all three timestamps is the inorganic molecule hydroxyl amine which peaks at $\sim 10^{-5}$ cm^{-3} at (185, 6.42) in (r,z) coordinates.

- The modelled gas-phase abundances of almost all the other COMs being comparable to that of the observed methanol indicate a possible similar inheritance or earlier in-situ formation, followed by thermal processing.

- The parametric model done in the disk line survey predicts abundances of methanol and formaldehyde in the thermally constrained region to be three orders of

magnitude smaller than the maximum fractional abundance of gas-phase formaldehyde at 1 Myr from the chemical model.

- When the disk line survey is run with abundances from both the chemical model in both the ALMA and SKA frequency ranges, it is seen that the maximum integrated intensity predicted is that of isocyanic acid.

- When run in SKA regime, the integrated intensity plots are relatively sparsely-populated and lower values of integrated intensities and fluxes are predicted in the SKA frequency range.

- In the ALMA regime, the magnitudes of the peak fluxes are also larger for all the molecules with the parametric model, with ratios of the predicted maximum line strength with the parametric model to that with the chemical model being as high as 8250 for dimethyl ether and reaching values of 1.2 for formaldehyde, for which the difference is relatively smaller.

- The ratio of the predicted maximum line flux in the SKA frequency range with the parametric model to that with the chemical model is seen to be the highest for dimethyl ether, and lowest for formic acid, for which the peak line flux predicted by the parametric model is only twice that predicted by the chemical model.

- When the disk line survey is run with abundances from the parametric model in the ALMA regime, the integrated intensities peak at generally lower frequencies.

- In the ALMA frequency range, the strongest line is the $6_{1,5} - 6_{0,6}$ isocyanic acid line with a peak flux of 7.3 Jy.

- The strongest lines predicted in the SKA regime after formaldehyde are those of methyl cyanide, its radical, isocyanic acid and glycolaldehyde, whose $1_0 - 0_0$, $1_{0,1,2} - 0_{0,0,1}$, $1_{0,1} - 0_{0,0}$ and $5_{1,4} - 5_{0,5}$ lines respectively have fluxes of 448 μJy, 458 μJy, 242 μJy and 219 μJy at frequencies ranging from 18-28 GHz.

- From the radiative transfer calculations with *LIME*, significant reservoirs of gas-phase methanol and formaldehyde, with abundances reaching 10^{-10} cm^{-3} are predicted to be located in an inner range of radii and an outer shoulder, possibly in line with the suggested double ring in Walsh et al. [2014a].

- The peak fractional abundances obtained from the chemical model in Chapter 2 are found to be 5 to 7 orders of magnitude greater than those reported at the same radii from the parametric modelling done with *LIME*, suggesting that the chemical model calculates overestimates of the fractional abundances. On the other hand, the abundances in this parametric are more comparable to those predicted in the parametric modelling in Chapter 3.

These findings will help inform further observations with ALMA and SKA. If detected, these molecules will expand the complex organic molecular inventory of warm Herbig disks, revealing the presence of the precursors to biologically important molecules in the material from which planets form.

References

C. P. Dullemond and J. D. Monnier. The Inner Regions of Protoplanetary Disks. , 48: 205–239, September 2010. doi: 10.1146/annurev-astro-081309-130932.

Thomas Henning and Dmitry Semenov. Chemistry in Protoplanetary Disks. *Chemical Reviews*, 113(12):9016–9042, December 2013. doi: 10.1021/cr400128p.

D. Fedele, C. Toci, L. Maud, and G. Lodato. ALMA 870 μm continuum observations of HD 100546. Evidence of a giant planet on a wide orbit. , 651:A90, July 2021. doi: 10.1051/0004-6361/202141278.

Alice S. Booth, Nienke van der Marel, Margot Leemker, Ewine F. van Dishoeck, and Satoshi Ohashi. A major asymmetric ice trap in a planet-forming disk. II. Prominent SO and SO_2 pointing to C/O ¡ 1. , 651:L6, July 2021a. doi: 10.1051/0004-6361/202141057.

Valentine Wakelam, Herma M. Cuppen, and Eric Herbst. Astrochemistry: Synthesis and Modelling. *arXiv e-prints*, art. arXiv:1309.7792, September 2013.

Robin T. Garrod, Susanna L. Widicus Weaver, and Eric Herbst. Complex Chemistry in Star-forming Regions: An Expanded Gas-Grain Warm-up Chemical Model. , 682 (1):283–302, July 2008. doi: 10.1086/588035.

M. Kama, S. Bruderer, E. F. van Dishoeck, M. Hogerheijde, C. P. Folsom, A. Miotello, D. Fedele, A. Belloche, R. Güsten, and F. Wyrowski. Volatile-carbon locking and release in protoplanetary disks. A study of TW Hya and HD 100546. , 592:A83, August 2016. doi: 10.1051/0004-6361/201526991.

Alice S. Booth, Catherine Walsh, Jeroen Terwisscha van Scheltinga, Ewine F. van Dishoeck, John D. Ilee, Michiel R. Hogerheijde, Mihkel Kama, and Hideko Nomura.

An inherited complex organic molecule reservoir in a warm planet-hosting disk. *Nature Astronomy*, 5:684–690, January 2021b. doi: 10.1038/s41550-021-01352-w.

Jonathan P. Williams and Lucas A. Cieza. Protoplanetary Disks and Their Evolution. , 49(1):67–117, September 2011. doi: 10.1146/annurev-astro-081710-102548.

D. McElroy, C. Walsh, A. J. Markwick, M. A. Cordiner, K. Smith, and T. J. Millar. The UMIST database for astrochemistry 2012. , 550:A36, February 2013. doi: 10.1051/0004-6361/201220465.

Karen M. Strom, Stephen E. Strom, Suzan Edwards, Sylvie Cabrit, and Michael F. Skrutskie. Circumstellar Material Associated with Solar-Type Pre-Main-Sequence Stars: A Possible Constraint on the Timescale for Planet Building. , 97:1451, May 1989. doi: 10.1086/115085.

David A. Weintraub, G. Sandell, and W. D. Duncan. Submillimeter Measurements of T Tauri and FU Orionis Stars. , 340:L69, May 1989. doi: 10.1086/185441.

C. R. O'dell and Zheng Wen. Postrefurbishment Mission Hubble Space Telescope Images of the Core of the Orion Nebula: Proplyds, Herbig-Haro Objects, and Measurements of a Circumstellar Disk. , 436:194, November 1994. doi: 10.1086/174892.

J. A. Eisner, L. A. Hillenbrand, John M. Carpenter, and S. Wolf. Constraining the Evolutionary Stage of Class I Protostars: Multiwavelength Observations and Modeling. , 635(1):396–421, December 2005. doi: 10.1086/497161.

Kamber R. Schwarz, Edwin A. Bergin, L. Ilsedore Cleeves, Ke Zhang, Karin I. Öberg, Geoffrey A. Blake, and Dana Anderson. Unlocking CO Depletion in Protoplanetary Disks. I. The Warm Molecular Layer. , 856(1):85, March 2018. doi: 10.3847/1538-4357/aaae08.

Michel Guélin and Jose Cernicharo. Organic Molecules in Interstellar Space: Latest Advances. *Frontiers in Astronomy and Space Sciences*, 9:787567, March 2022. doi: 10.3389/fspas.2022.787567.

Jes K. Jørgensen, Arnaud Belloche, and Robin T. Garrod. Astrochemistry During the Formation of Stars. , 58:727–778, August 2020. doi: 10.1146/annurev-astro-032620-021927.

Karin I. Öberg, Viviana V. Guzmán, Kenji Furuya, Chunhua Qi, Yuri Aikawa, Sean M. Andrews, Ryan Loomis, and David J. Wilner. The comet-like composition of a protoplanetary disk as revealed by complex cyanides. , 520(7546):198–201, April 2015. doi: 10.1038/nature14276.

Catherine Walsh, Ryan A. Loomis, Karin I. Öberg, Mihkel Kama, Merel L. R. van 't Hoff, Tom J. Millar, Yuri Aikawa, Eric Herbst, Susanna L. Widicus Weaver, and Hideko Nomura. First Detection of Gas-phase Methanol in a Protoplanetary Disk. , 823(1):L10, May 2016. doi: 10.3847/2041-8205/823/1/L10.

Cécile Favre, Davide Fedele, Dmitry Semenov, Sergey Parfenov, Claudio Codella, Cecilia Ceccarelli, Edwin A. Bergin, Edwige Chapillon, Leonardo Testi, Franck Hersant, Bertrand Lefloch, Francesco Fontani, Geoffrey A. Blake, L. Ilsedore Cleeves, Chunhua Qi, Kamber R. Schwarz, and Vianney Taquet. First Detection of the Simplest Organic Acid in a Protoplanetary Disk. , 862(1):L2, July 2018. doi: 10.3847/2041-8213/aad046.

P. Swings and L. Rosenfeld. Considerations Regarding Interstellar Molecules. , 86: 483–486, November 1937. doi: 10.1086/143880.

Eric Herbst and Ewine F. van Dishoeck. Complex Organic Interstellar Molecules. , 47 (1):427–480, September 2009. doi: 10.1146/annurev-astro-082708-101654.

Karin I. Öberg, Ruth Murray-Clay, and Edwin A. Bergin. The Effects of Snowlines on C/O in Planetary Atmospheres. , 743(1):L16, December 2011. doi: 10.1088/ 2041-8205/743/1/L16.

Ewine F. van Dishoeck and Geoffrey A. Blake. Chemical Evolution of Star-Forming Regions. , 36:317–368, January 1998. doi: 10.1146/annurev.astro.36.1.317.

Nienke van der Marel, Alice S. Booth, Margot Leemker, Ewine F. van Dishoeck, and Satoshi Ohashi. A major asymmetric ice trap in a planet-forming disk. I. Formaldehyde and methanol. , 651:L5, July 2021. doi: 10.1051/0004-6361/202141051.

M. Vioque, R. D. Oudmaijer, D. Baines, I. Mendigutía, and R. Pérez-Martínez. Gaia DR2 study of Herbig Ae/Be stars. , 620:A128, December 2018. doi: 10.1051/0004-6361/201832870.

Gaia Collaboration, A. G. A. Brown, A. Vallenari, T. Prusti, J. H. J. de Bruijne, C. Babusiaux, C. A. L. Bailer-Jones, M. Biermann, D. W. Evans, L. Eyer, F. Jansen, C. Jordi, S. A. Klioner, U. Lammers, L. Lindegren, X. Luri, F. Mignard, C. Panem, D. Pourbaix, S. Randich, P. Sartoretti, H. I. Siddiqui, C. Soubiran, F. van Leeuwen, N. A. Walton, F. Arenou, U. Bastian, M. Cropper, R. Drimmel, D. Katz, M. G. Lattanzi, J. Bakker, C. Cacciari, J. Castañeda, L. Chaoul, N. Cheek, F. De Angeli, C. Fabricius, R. Guerra, B. Holl, E. Masana, R. Messineo, N. Mowlavi, K. Nienartowicz, P. Panuzzo, J. Portell, M. Riello, G. M. Seabroke, P. Tanga, F. Thévenin, G. Gracia-Abril, G. Comoretto, M. Garcia-Reinaldos, D. Teyssier, M. Altmann, R. Andrae, M. Audard, I. Bellas-Velidis, K. Benson, J. Berthier, R. Blomme, P. Burgess, G. Busso, B. Carry, A. Cellino, G. Clementini, M. Clotet, O. Creevey, M. Davidson, J. De Ridder, L. Delchambre, A. Dell'Oro, C. Ducourant, J. Fernández-Hernández, M. Fouesneau, Y. Frémat, L. Galluccio, M. García-Torres, J. González-Núñez, J. J. González-Vidal, E. Gosset, L. P. Guy, J. L. Halbwachs, N. C. Hambly, D. L. Harrison, J. Hernández, D. Hestroffer, S. T. Hodgkin, A. Hutton, G. Jasniewicz, A. Jean-Antoine-Piccolo, S. Jordan, A. J. Korn, A. Krone-Martins, A. C. Lanzafame, T. Lebzelter, W. Löffler, M. Manteiga, P. M. Marrese, J. M. Martín-Fleitas, A. Moitinho, A. Mora, K. Muinonen, J. Osinde, E. Pancino, T. Pauwels, J. M. Petit, A. Recio-Blanco, P. J. Richards, L. Rimoldini, A. C. Robin, L. M. Sarro, C. Siopis, M. Smith, A. Sozzetti, M. Süveges, J. Torra, W. van Reeven, U. Abbas, A. Abreu Aramburu, S. Accart, C. Aerts, G. Altavilla, M. A. Álvarez, R. Alvarez, J. Alves, R. I. Anderson, A. H. Andrei, E. Anglada Varela, E. Antiche, T. Antoja, B. Arcay, T. L. Astraatmadja, N. Bach, S. G. Baker, L. Balaguer-Núñez, P. Balm, C. Barache, C. Barata, D. Barbato, F. Barblan, P. S. Barklem, D. Barrado, M. Barros, M. A. Barstow, S. Bartholomé Muñoz, J. L. Bassilana, U. Becciani, M. Bellazzini, A. Berihuete, S. Bertone, L. Bianchi, O. Bienaymé, S. Blanco-Cuaresma, T. Boch, C. Boeche, A. Bombrun, R. Borrachero, D. Bossini, S. Bouquillon, G. Bourda, A. Bragaglia, L. Bramante, M. A. Breddels, A. Bressan, N. Brouillet, T. Brüsemeister, E. Brugaletta, B. Bucciarelli, A. Burlacu, D. Busonero, A. G. Butkevich, R. Buzzi, E. Caffau, R. Cancelliere, G. Cannizzaro, T. Cantat-Gaudin, R. Carballo, T. Carlucci, J. M. Carrasco, L. Casamiquela, M. Castellani, A. Castro-Ginard, P. Charlot, L. Chemin, A. Chiavassa, G. Cocozza, G. Costigan, S. Cowell, F. Crifo, M. Crosta, C. Crowley, J. Cuypers, C. Dafonte, Y. Damer-

dji, A. Dapergolas, P. David, M. David, P. de Laverny, F. De Luise, R. De March, D. de Martino, R. de Souza, A. de Torres, J. Debosscher, E. del Pozo, M. Delbo, A. Delgado, H. E. Delgado, P. Di Matteo, S. Diakite, C. Diener, E. Distefano, C. Dolding, P. Drazinos, J. Durán, B. Edvardsson, H. Enke, K. Eriksson, P. Esquej, G. Eynard Bontemps, C. Fabre, M. Fabrizio, S. Faigler, A. J. Falcão, M. Farràs Casas, L. Federici, G. Fedorets, P. Fernique, F. Figueras, F. Filippi, K. Findeisen, A. Fonti, E. Fraile, M. Fraser, B. Frézouls, M. Gai, S. Galleti, D. Garabato, F. García-Sedano, A. Garofalo, N. Garralda, A. Gavel, P. Gavras, J. Gerssen, R. Geyer, P. Giacobbe, G. Gilmore, S. Girona, G. Giuffrida, F. Glass, M. Gomes, M. Granvik, A. Gueguen, A. Guerrier, J. Guiraud, R. Gutiérrez-Sánchez, R. Haigron, D. Hatzidimitriou, M. Hauser, M. Haywood, U. Heiter, A. Helmi, J. Heu, T. Hilger, D. Hobbs, W. Hofmann, G. Holland, H. E. Huckle, A. Hypki, V. Icardi, K. Janßen, G. Jevardat de Fombelle, P. G. Jonker, Á. L. Juhász, F. Julbe, A. Karampelas, A. Kewley, J. Klar, A. Kochoska, R. Kohley, K. Kolenberg, M. Kontizas, E. Kontizas, S. E. Koposov, G. Kordopatis, Z. Kostrzewa-Rutkowska, P. Koubsky, S. Lambert, A. F. Lanza, Y. Lasne, J. B. Lavigne, Y. Le Fustec, C. Le Poncin-Lafitte, Y. Lebreton, S. Leccia, N. Leclerc, I. Lecoeur-Taibi, H. Lenhardt, F. Leroux, S. Liao, E. Licata, H. E. P. Lindstrøm, T. A. Lister, E. Livanou, A. Lobel, M. López, S. Managau, R. G. Mann, G. Mantelet, O. Marchal, J. M. Marchant, M. Marconi, S. Marinoni, G. Marschalkó, D. J. Marshall, M. Martino, G. Marton, N. Mary, D. Massari, G. Matijevič, T. Mazeh, P. J. McMillan, S. Messina, D. Michalik, N. R. Millar, D. Molina, R. Molinaro, L. Molnár, P. Montegriffo, R. Mor, R. Morbidelli, T. Morel, D. Morris, A. F. Mulone, T. Muraveva, I. Musella, G. Nelemans, L. Nicastro, L. Noval, W. O'Mullane, C. Ordénovic, D. Ordóñez-Blanco, P. Osborne, C. Pagani, I. Pagano, F. Pailler, H. Palacin, L. Palaversa, A. Panahi, M. Pawlak, A. M. Piersimoni, F. X. Pineau, E. Plachy, G. Plum, E. Poggio, E. Poujoulet, A. Prša, L. Pulone, E. Racero, S. Ragaini, N. Rambaux, M. Ramos-Lerate, S. Regibo, C. Reylé, F. Riclet, V. Ripepi, A. Riva, A. Rivard, G. Rixon, T. Roegiers, M. Roelens, M. Romero-Gómez, N. Rowell, F. Royer, L. Ruiz-Dern, G. Sadowski, T. Sagristà Sellés, J. Sahlmann, J. Salgado, E. Salguero, N. Sanna, T. Santana-Ros, M. Sarasso, H. Savietto, M. Schultheis, E. Sciacca, M. Segol, J. C. Segovia, D. Ségransan, I. C. Shih, L. Siltala, A. F. Silva, R. L. Smart, K. W. Smith, E. Solano, F. Solitro, R. Sordo, S. Soria Nieto, J. Souchay, A. Spagna, F. Spoto, U. Stampa, I. A. Steele, H. Steidelmüller, C. A.

Stephenson, H. Stoev, F. F. Suess, J. Surdej, L. Szabados, E. Szegedi-Elek, D. Tapiador, F. Taris, G. Tauran, M. B. Taylor, R. Teixeira, D. Terrett, P. Teyssandier, W. Thuillot, A. Titarenko, F. Torra Clotet, C. Turon, A. Ulla, E. Utrilla, S. Uzzi, M. Vaillant, G. Valentini, V. Valette, A. van Elteren, E. Van Hemelryck, M. van Leeuwen, M. Vaschetto, A. Vecchiato, J. Veljanoski, Y. Viala, D. Vicente, S. Vogt, C. von Essen, H. Voss, V. Votruba, S. Voutsinas, G. Walmsley, M. Weiler, O. Wertz, T. Wevers, Ł. Wyrzykowski, A. Yoldas, M. Žerjal, H. Ziaeepour, J. Zorec, S. Zschocke, S. Zucker, C. Zurbach, and T. Zwitter. Gaia Data Release 2. Summary of the contents and survey properties. , 616:A1, August 2018. doi: 10.1051/0004-6361/201833051.

D. Fedele, S. Bruderer, M. E. van den Ancker, and I. Pascucci. On the Asymmetry of the OH Ro-vibrational Lines in HD 100546. , 800(1):23, February 2015. doi: 10.1088/0004-637X/800/1/23.

Sascha P. Quanz, Adam Amara, Michael R. Meyer, Julien H. Girard, Matthew A. Kenworthy, and Markus Kasper. Confirmation and Characterization of the Protoplanet HD 100546 b—Direct Evidence for Gas Giant Planet Formation at 50 AU. , 807(1): 64, July 2015a. doi: 10.1088/0004-637X/807/1/64.

D. R. Ardila, D. A. Golimowski, J. E. Krist, M. Clampin, H. C. Ford, and G. D. Illingworth. Hubble Space Telescope Advanced Camera for Surveys Coronagraphic Observations of the Dust Surrounding HD 100546. , 665(1):512–534, August 2007. doi: 10.1086/519296.

A. Boccaletti, E. Pantin, A. M. Lagrange, J. C. Augereau, H. Meheut, and S. P. Quanz. Multiple spiral patterns in the transitional disk of HD 100546. , 560:A20, December 2013. doi: 10.1051/0004-6361/201322365.

Jaime E. Pineda, Judit Szulágyi, Sascha P. Quanz, Ewine F. van Dishoeck, Antonio Garufi, Farzana Meru, Gijs D. Mulders, Leonardo Testi, Michael R. Meyer, and Maddalena Reggiani. High-resolution ALMA Observations of HD 100546: Asymmetric Circumstellar Ring and Circumplanetary Disk Upper Limits. , 871(1):48, January 2019. doi: 10.3847/1538-4357/aaf389.

Catherine Walsh, Attila Juhász, Paola Pinilla, Daniel Harsono, Geoffrey S. Mathews, William R. F. Dent, Michiel R. Hogerheijde, T. Birnstiel, Gwendolyn Meeus, Hideko Nomura, Yuri Aikawa, T. J. Millar, and Göran Sandell. ALMA Hints at the Presence

of two Companions in the Disk around HD 100546. , 791(1):L6, August 2014a. doi: 10.1088/2041-8205/791/1/L6.

Sascha P. Quanz, Adam Amara, Michael R. Meyer, Julien H. Girard, Matthew A. Kenworthy, and Markus Kasper. Confirmation and Characterization of the Protoplanet HD 100546 b—Direct Evidence for Gas Giant Planet Formation at 50 AU. , 807(1): 64, July 2015b. doi: 10.1088/0004-637X/807/1/64.

C. Brinch and M. R. Hogerheijde. LIME - a flexible, non-LTE line excitation and radiation transfer method for millimeter and far-infrared wavelengths. , 523:A25, November 2010. doi: 10.1051/0004-6361/201015333.

Catherine Walsh, Tom. J. Millar, Hideko Nomura, Eric Herbst, Susanna Widicus Weaver, Yuri Aikawa, Jacob C. Laas, and Anton I. Vasyunin. Complex organic molecules in protoplanetary disks. , 563:A33, March 2014b. doi: 10.1051/0004-6361/201322446.

Richard Teague. GoFish: Fishing for Line Observations in Protoplanetary Disks. *The Journal of Open Source Software*, 4(41):1632, September 2019. doi: 10.21105/joss.01632.

Michiel Hogerheijde and Floris van der Tak. RATRAN: Radiative Transfer and Molecular Excitation in One and Two Dimensions. Astrophysics Source Code Library, record ascl:0008.002, August 2000.

Brett A. McGuire. 2021 Census of Interstellar, Circumstellar, Extragalactic, Protoplanetary Disk, and Exoplanetary Molecules. , 259(2):30, April 2022. doi: 10.3847/1538-4365/ac2a48.

A. Dutrey, S. Guilloteau, and P. Ho. Interferometric Spectroimaging of Molecular Gas in Protoplanetary Disks. In Bo Reipurth, David Jewitt, and Klaus Keil, editors, *Protostars and Planets V*, page 495, January 2007.

B. T. Draine. Interstellar Dust Grains. , 41:241–289, January 2003. doi: 10.1146/annurev.astro.41.011802.094840.

B. T. Draine. Interstellar Dust Models and Evolutionary Implications. In T. Henning, E. Grün, and J. Steinacker, editors, *Cosmic Dust - Near and Far*, volume 414 of *Astronomical Society of the Pacific Conference Series*, page 453, December 2009.

F. Hersant, V. Wakelam, A. Dutrey, S. Guilloteau, and E. Herbst. Cold CO in circumstellar disks. On the effects of photodesorption and vertical mixing. , 493(3): L49–L52, January 2009. doi: 10.1051/0004-6361:200811082.

D. Semenov, D. Wiebe, and Th. Henning. Gas-Phase CO in Protoplanetary Disks: A Challenge for Turbulent Mixing. , 647(1):L57–L60, August 2006. doi: 10.1086/507096.

Yuri Aikawa, Valentine Wakelam, Robin T. Garrod, and Eric Herbst. Molecular Evolution and Star Formation: From Prestellar Cores to Protostellar Cores. , 674(2): 984–996, February 2008. doi: 10.1086/524096.

Catherine Walsh, T. J. Millar, and Hideko Nomura. Chemical Processes in Protoplanetary Disks. , 722(2):1607–1623, October 2010. doi: 10.1088/0004-637X/722/2/1607.

Catherine Walsh, Hideko Nomura, T. J. Millar, and Yuri Aikawa. Chemical Processes in Protoplanetary Disks. II. On the Importance of Photochemistry and X-Ray Ionization. , 747(2):114, March 2012. doi: 10.1088/0004-637X/747/2/114.

J. Woodall, M. Agúndez, A. J. Markwick-Kemper, and T. J. Millar. The UMIST database for astrochemistry 2006. , 466(3):1197–1204, May 2007. doi: 10.1051/0004-6361:20064981.

Catherine Walsh, Hideko Nomura, and Ewine van Dishoeck. The molecular composition of the planet-forming regions of protoplanetary disks across the luminosity regime. , 582:A88, October 2015. doi: 10.1051/0004-6361/201526751.

Tatsuhiko I. Hasegawa, Eric Herbst, and Chun M. Leung. Models of Gas-Grain Chemistry in Dense Interstellar Clouds with Complex Organic Molecules. , 82:167, September 1992. doi: 10.1086/191713.

K. I. Öberg, R. T. Garrod, E. F. van Dishoeck, and H. Linnartz. Formation rates of complex organics in UV irradiated CH$_3$OH-rich ices. I. Experiments. , 504(3): 891–913, September 2009. doi: 10.1051/0004-6361/200912559.

K. J. Chuang, G. Fedoseev, S. Ioppolo, E. F. van Dishoeck, and H. Linnartz. H-atom addition and abstraction reactions in mixed CO, H$_2$CO and CH$_3$OH ices - an extended view on complex organic molecule formation. , 455(2):1702–1712, January 2016. doi: 10.1093/mnras/stv2288.

Arthur D. Bosman, Catherine Walsh, and Ewine F. van Dishoeck. CO destruction in protoplanetary disk midplanes: Inside versus outside the CO snow surface. , 618: A182, October 2018. doi: 10.1051/0004-6361/201833497.

Jamila Pegues, Karin I. Öberg, Jennifer B. Bergner, Ryan A. Loomis, Chunhua Qi, Romane Le Gal, L. Ilsedore Cleeves, Viviana V. Guzmán, Jane Huang, Jes K. Jørgensen, Sean M. Andrews, Geoffrey A. Blake, John M. Carpenter, Kamber R. Schwarz, Jonathan P. Williams, and David J. Wilner. An ALMA Survey of H_2CO in Protoplanetary Disks. , 890(2):142, February 2020. doi: 10.3847/1538-4357/ab64d9.

C. A. Grady, B. Woodgate, S. R. Heap, C. Bowers, III Nuth, J. A., G. J. Herczeg, and H. G. M. Hill. Resolving the Inner Cavity of the HD 100546 Disk: A Candidate Young Planetary System? , 620(1):470–480, February 2005. doi: 10.1086/426887.

G. D. Mulders, L. B. F. M. Waters, C. Dominik, B. Sturm, J. Bouwman, M. Min, A. P. Verhoeff, B. Acke, J. C. Augereau, N. J. Evans, Th. Henning, G. Meeus, and J. Olofsson. Low abundance, strong features: window-dressing crystalline forsterite in the disk wall of HD 100546. , 531:A93, July 2011. doi: 10.1051/0004-6361/201116770.

Nashanty G. C. Brunken, Alice S. Booth, Margot Leemker, Pooneh Nazari, Nienke van der Marel, and Ewine F. van Dishoeck. A major asymmetric ice trap in a planet-forming disk. III. First detection of dimethyl ether. , 659:A29, March 2022. doi: 10.1051/0004-6361/202142981.

A. E. Douglas and G. Herzberg. Note on $CH\hat{\{+\}}$ in Interstellar Space and in the Laboratory. , 94:381, September 1941. doi: 10.1086/144342.

S. Weinreb, A. H. Barrett, M. L. Meeks, and J. C. Henry. Radio Observations of OH in the Interstellar Medium. , 200(4909):829–831, November 1963. doi: 10.1038/200829a0.

Robert Braun, Anna Bonaldi, Tyler Bourke, Evan Keane, and Jeff Wagg. Anticipated Performance of the Square Kilometre Array – Phase 1 (SKA1). *arXiv e-prints*, art. arXiv:1912.12699, December 2019.

C. H. Townes and A. L. Schawlow. *Microwave Spectroscopy.* 1955.

A. Belloche, K. M. Menten, C. Comito, H. S. P. Müller, P. Schilke, J. Ott, S. Thorwirth, and C. Hieret. Detection of amino acetonitrile in Sgr B2(N). , 482(1):179–196, April 2008. doi: 10.1051/0004-6361:20079203.

Lucy M. Ziurys and Aldo J. Apponi. What Constitutes Spectroscopic Proof for the Detection of Large "Hot Core" Molecules? In Dariusz C. Lis, Geoffrey A. Blake, and Eric Herbst, editors, *Astrochemistry: Recent Successes and Current Challenges*, volume 231, pages 207–216, August 2005. doi: 10.1017/S1743921306007204.

H. M. Pickett, R. L. Poynter, E. A. Cohen, M. L. Delitsky, J. C. Pearson, and H. S. P. Müller. Submillimeter, millimeter and microwave spectral line catalog. , 60(5):883–890, November 1998. doi: 10.1016/S0022-4073(98)00091-0.

Holger S. P. Müller, Frank Schlöder, Jürgen Stutzki, and Gisbert Winnewisser. The Cologne Database for Molecular Spectroscopy, CDMS: a useful tool for astronomers and spectroscopists. *Journal of Molecular Structure*, 742(1-3):215–227, May 2005. doi: 10.1016/j.molstruc.2005.01.027.

F. L. Schöier, F. F. S. van der Tak, E. F. van Dishoeck, and J. H. Black. An atomic and molecular database for analysis of submillimetre line observations. , 432(1):369–379, March 2005. doi: 10.1051/0004-6361:20041729.

Richard Teague and Ryan Loomis. The Excitation Conditions of CN in TW Hya. , 899(2):157, August 2020. doi: 10.3847/1538-4357/aba956.

Floris van der Tak. Radiative Transfer and Molecular Data for Astrochemistry. In José Cernicharo and Rafael Bachiller, editors, *The Molecular Universe*, volume 280, pages 449–460, December 2011. doi: 10.1017/S1743921311025191.

C. Bernes. A MOnte Carlo approach to non-LTE radiative transfer problems. , 73: 67–73, March 1979.

M. Juvela. Non-LTE radiative transfer in clumpy molecular clouds. , 322:943–961, June 1997.

Ya. N. Pavlyuchenkov and B. M. Shustov. A Method for Molecular-Line Radiative-Transfer Computations and Its Application to a Two-Dimensional Model for the Starless Core L1544. *Astronomy Reports*, 48(4):315–326, April 2004. doi: 10.1134/1.1704676.

Ya. Pavlyuchenkov, D. Semenov, Th. Henning, St. Guilloteau, V. Piétu, R. Launhardt, and A. Dutrey. Molecular Line Radiative Transfer in Protoplanetary Disks: Monte Carlo Simulations versus Approximate Methods. , 669(2):1262–1278, November 2007. doi: 10.1086/521872.

Izaskun Jiménez-Serra, Jesús Martín-Pintado, Aran Insausti, Elena R. Alonso, Emilio J. Cocinero, and Tyler L. Bourke. The SKA as a Prebiotic Molecule Detector. *Frontiers in Astronomy and Space Sciences*, 9:843766, March 2022. doi: 10.3389/fspas.2022.843766.